Stabilization mechanism of pores in aluminum alloy foam during semi-solid route

セミソリッド発泡法で作製する際の発泡アルミニウム合金における
気孔安定化メカニズム

February, 2024

Satomi TAKAMATSU
髙松　聖美

Stabilization mechanism of pores in aluminum alloy foam during semi-solid route

セミソリッド発泡法で作製する際の発泡アルミニウム合金における
気孔安定化メカニズム

February, 2024

Waseda University Graduate School of Fundamental Science and Engineering

Department of Materials Science, Research on Materials Process Engineering

Satomi TAKAMATSU
髙松　聖美

Contents

List of Figures

List of Tables

Nomenclature

A_f	m²	cross-sectional area of the film
A_{cw}	mm²	area of cell wall
A_{cw}''	mm²	cross-sectional area of cell wall viewed in the flow direction
A_m	mm²	area of metallic part
A_p	mm²	area of pore
A_{pr}	μm²	area of primary crystal
A_{pr}'	μm²	original area of primary crystal
A_{pr}''	μm²	area of the primary crystal in the flow direction
A_w	mm²	area of measurement window
d_p	mm	equivalent pore diameter
C	%	concentration of oxygen
d_{pr}	μm	equivalent diameter of primary crystal
d_{pr}'	μm	original equivalent circle diameter of primary crystal
$\overline{d_{pr}'}$	μm	average original equivalent circle diameter of primary crystal
$\overline{d_p}$	mm	average equivalent circle diameter of pore
$\bar{e}$		average pore circularity
f_{s_cr}		critical volume fraction of solid
f_s	%	volume fraction of solid
g	m/s²	acceleration due to gravity
h_0	m	height of the film
h	mm	position in height
H	mm	maximum height
L_{cw}	mm	length of cell wall
L_p	mm	pore perimeter
M_{air}	kg	mass of the foam
M_{water}	kg	mass of the foam in the water
n_{cc}		number of clogged cell walls
N_{cw}		number of all cell walls
N_p		total number of pores in the measurement window
n_f		number of foams
n_s		number of sizes coming from vertex of lattice
n_i		number of inflows
n_o		number of outflows

N_{path}		number of all paths
n_{path}		number of paths that is pass through
N_δ		number of all cell wall structure
n_δ		number of clogged cell wall structures
P_{p}	Pa	pressure inside the pore
ΔP	Pa	capillary pressure
p	%	porosity
$\bar{p}$	%	average porosity
p_{cw}		area ratio of primary crystals to area of cell wall: percolation probability of cell wall
p_{cw}'		percolation threshold for cell wall
p_{f}		percolation probability for the lattice
p_{f}'		percolation threshold for planar lattice
P_{O2}	MPa	partial pressure of oxygen
P_{t}	MPa	total pressure
p_δ		percolation probability for cell wall structure
p_δ'		percolation threshold for cell wall structure
R	mm	curvature radius
Δr	μm	grown radius
$\overline{\Delta r}$	μm	average grown radius
R^2		determination coefficient
r_c		ratio of clogged cell wall to all cell wall
dr	mm	thickness of sphere
r	mm	distance from target cell wall structure to spherical surface
S_{pr}	μm	spherical diameter of primary crystal
t	s	time
T_1	°C	temperature of the melt
T_1'	°C	calibrated temperature
T_2	°C	temperature of bottom of crucible
W_0	m	maximum width of the film
W_t	m	time-varying minimum film thickness

Greek symbols

δ		cell wall structure
γ	mN/m	surface tension

μ	Pa·S	viscosity of the melt
ρ	kg/m3	density
ρ_{H2O}	kg/m^3	the density of H2O at room temperature
ρ_{np}	kg/m^3	density of Al-6.4mass%Si alloy
ρ_p	kg/m^3	density of aluminum alloy foam
ρ_δ		number density of distributed cell wall structure
σ		relative standard deviation
τ	N·m	torque

Abbreviations

$g(r)$	pair distribution function
$n(r)$	radial distribution function

Subscripts

i		serial number
x	mm	coordinate
y	mm	coordinate
z	mm	coordinate

Chapter 1

Introduction

1. Introduction

1.1. Overview

Many porous materials exist in the natural world, e.g., bone, honeycomb, and bamboo. These materials exhibit high strength and rigidity because of their internal cell structure, even when their density is considerably low compared to that of dense materials [1]. Since the 20th century, artificial porous materials have been engineered to realize materials with unique properties, such as shock absorbance, sound absorbance, heat insulation, sorting capability as a filter, and other similar properties [2]. Examples of such artificial porous materials include cardboards, styrofoam, and sponges. Porous metals have recently attracted increasing research attention in response to the demands for reducing environmental load. Further, porous metals are expected to be used as materials for a wide range of industrial products, including a crash box in a car, a heat exchanger, an acoustic material, a biomaterial, and a battery box. [3-11]

Porous metals can be classified into two groups: open-cell and closed-cell (Figure 1-1). Open-cell porous metals possesses many different types of structures, including lattices, fibers, and sponges; further, they have open cell-to-cell boundary surfaces, and the metal parts are concentrated at the ridges of the cells. Open-cell porous metals have permeable structures, and therefore, they are used in biomaterials, heat exchangers, and filtration systems[5,9-13]. Based on the fabrication method, open-cell porous metals can be fabricated with a controlled structure and used as a shock-absorbing material [14,15]. Closed-cell porous metals have a closed cell-to-cell boundary surface. Each cell is independent and referred to as a pore. The dispersion of a gaseous phase in a liquid or a solid is called a foam. Therefore, a closed-cell porous metal is referred to as a metal foam. Currently, many companies commercially develop and manufacture metal foam products [6-8]. Especially, aluminum alloy foams are fabricated as commercial products because although aluminum is very light, its strength can be increased by adding elements. However, the structure of the aluminum alloy foam is random because of the fabrication method employed. Thus, pore structures may vary within the product, thereby resulting in different properties in different areas. In addition, the pore structure differs from lot to lot. The low uniformity and reproducibility significantly decrease product reliability.

The uniformity (pore morphologies, such as pore size and circularity, are uniform in one metal foam) and reproducibility (pore morphologies of the foams among multiple fabrications are the same) of aluminum alloy foams are essential factors for future industrial use (Figure 1-2). The desired mechanical properties cannot be realized if the aluminum alloy foam has low uniformity; in addition, aluminum alloy foams with poor reproducibility deplete customer confidence. The drainage phenomenon is the primary factor responsible for these issues. Drainage is a type of liquid flow that occurs in a cell wall, which is a narrow path between two pores. The liquid inside the cell wall runs

out if the drainage advances excessively; however, because the cell wall cannot hold its shape without any liquid, the cell wall ruptures. Subsequently, the pores connect to each other and become coarse.
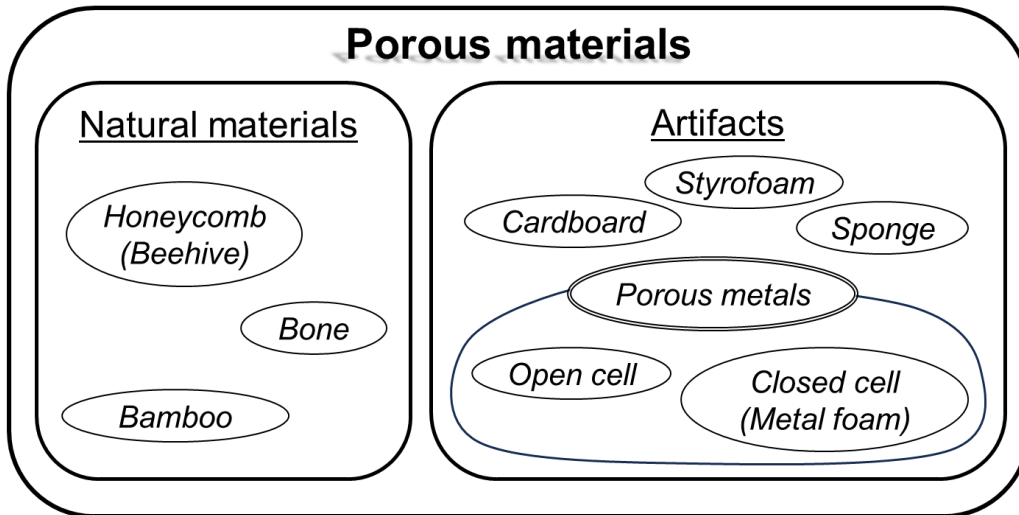
Figure 1-1 Schematic grouping of porous materials including both of natural and artificial materials.
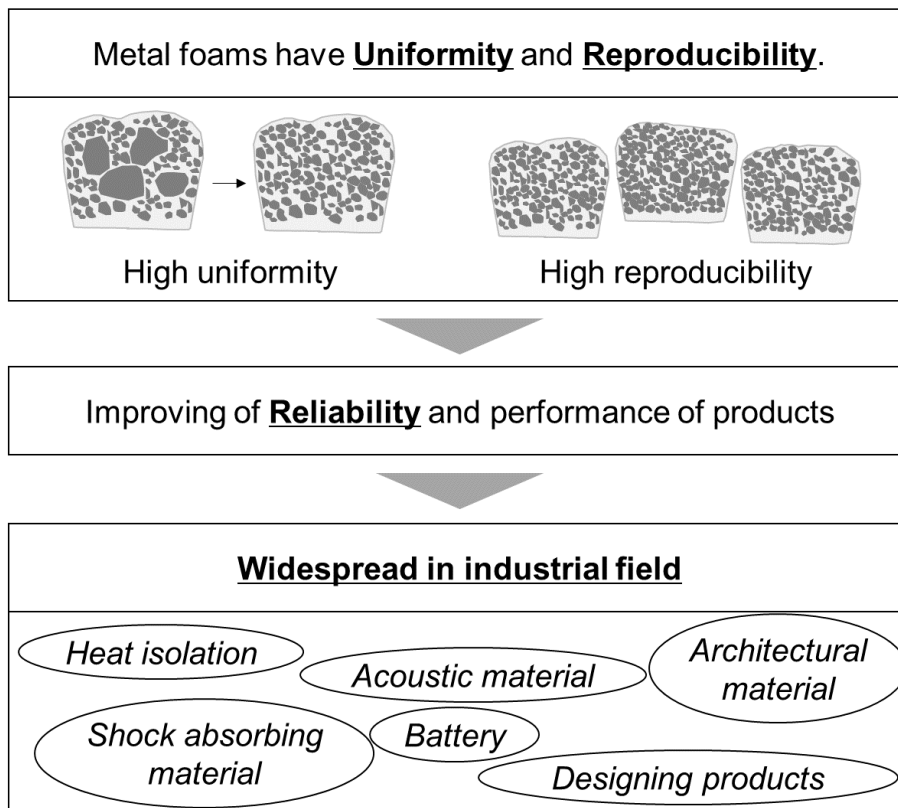
Figure 1-2 Schematic of the strategy for increasing the industrial use of metal foams.

Further, the drainage can cause each pore to be unequal in one aluminum alloy foam, causing the pore morphologies in aluminum alloy foams among multiple fabrications to be different. Therefore, every fabrication method focuses on approaches to prevent drainage during fabrication.

The melt route is one of the easiest fabrication methods for aluminum alloy foams [16,17]. In the melt route, a blowing agent (e.g., titanium hydrate, TiH_2) is added to the molten metal, which is then allowed to solidify after the foaming process. During the foaming process, gas is generated because of the thermal decomposition of the blowing agent. Without any treatment for the melt, the drainage easily advances in the cell wall. Thus, the melt route increases the apparent viscosity of the melt by adding a thickening agent (e.g., Al_2O_3, MgO, and SiC) into the molten metal before the foaming process [16], which can effectively realize uniform foaming. However, thickening agents are impurities in the base alloy and can lower the mechanical properties of the metal foam.

Hanafusa *et al.* developed another fabrication method called the semi-solid route, which does not use any additional thickening agent to increase the apparent viscosity of the molten metal and instead uses primary crystals as the thickening agent [18]. Primary crystals are inherently included in the alloy, which makes adding impurity elements unnecessary. Further, the semi-solid route is an environmentally friendly method because the aluminum alloy foam fabricated via this method can easily be recycled because of the small amount of impurities.

Both fabrication methods have been investigated to identify how the pores and cell walls become uniform and stable (stabilization mechanism) for realizing the industrial use of aluminum alloy foams. Previous research on the melt route revealed that small thickening particles are fixed on the surface of the cell wall and connected to each other [19]. Further, the preferred range of the thickening agent particle in size and volume fraction was obtained experimentally. According to the United States Patent 4973358, the preferred range where the foaming process advances properly is 1–20 μm in size and 5–15% in volume fraction (Figure 1-3) [20]. Further, the surface of the cell wall becomes oxidized because of the oxygen in the furnace [21]. The boundary of the oxide surface and base alloy can easily catch the thickening particles on its plane, and therefore, not only the thickening agent but also the oxide layer on the surface of the cell wall are required to prevent drainage and ensure cell wall stability.

15
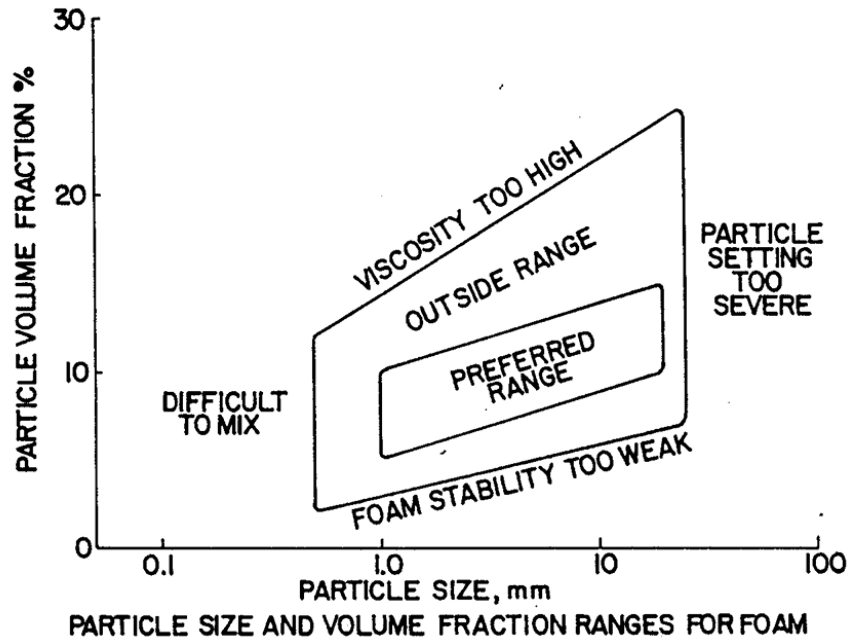
Figure 1-3 Particle size and volume fraction ranges for aluminum alloy foam fabricated in the melt route [20].

The primary crystals are not affixed on the surface of the cell wall, and instead, they aggregate in the alloy film, simulating the one cell wall in the metal foam [22]. This prevents the drainage because the cell wall is clogged by the aggregated primary crystals. A different stabilization mechanism can be employed in the semi-solid route because the average size of the primary crystals which is around 150 μm is ten times larger than the preferred size of the thickening agent. In previous research, this different stabilization mechanism was referred to as clogging effect. Stability is attributed to not only the increasing apparent viscosity of the semi-solid slurry but also the aggregated primary crystals. However, the minimum amount of primary crystals required to prevent the drainage remains unclear (Figure 1-4). In addition, the clogging effect is only confirmed in the alloy film, which is not a real cell wall. Moreover, it is not clear if the clogging effect can work in actual aluminum alloy foams. Therefore, the clogging effect must be extended to the entire aluminum alloy foam to reveal the stabilization mechanism of the semi-solid route.
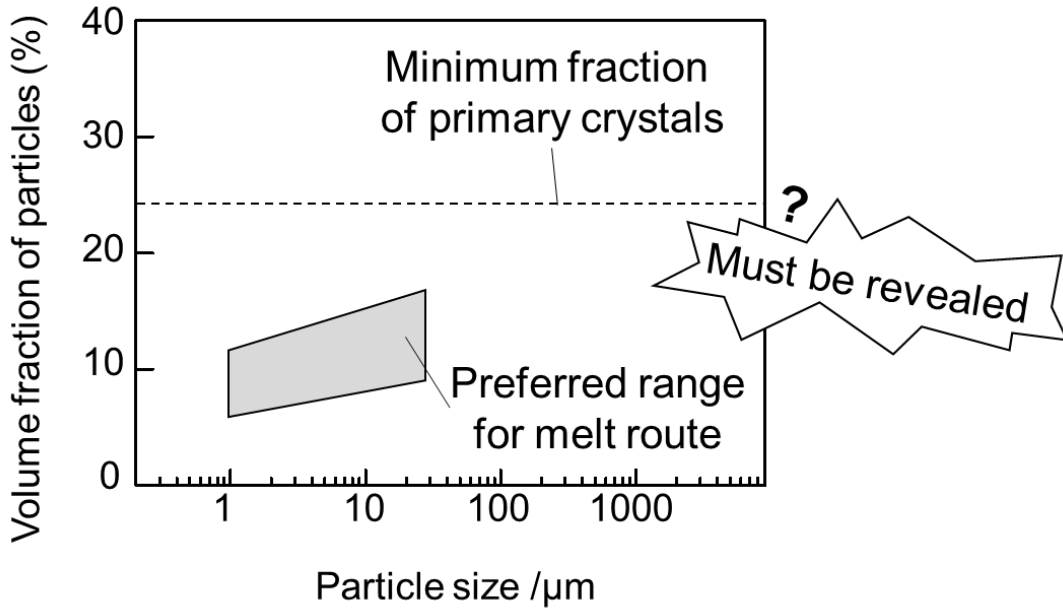
Figure 1-4 Schematic assignment that must be revealed.

Percolation theory describes the behavior of connected obstacles in a system with any type of structure. The ratio of obstacles that prevent liquid flow in a system is called percolation probability. Liquid flow stops because of the obstacles when the value of percolation probability exceeds the percolation threshold. The percolation threshold changes depending on the structure of the system, such as tube-type flow and lattice-structural flow, as indicated in Figure 1-5. The minimum amount of primary crystals required to prevent drainage in the cell wall and the entire metal foam can be determined by adopting this theory on the clogging effect. Further, the effect of increasing primary crystals on the stability should be discussed.

(a) Tube-type flow   (b) Lattice-structural flow
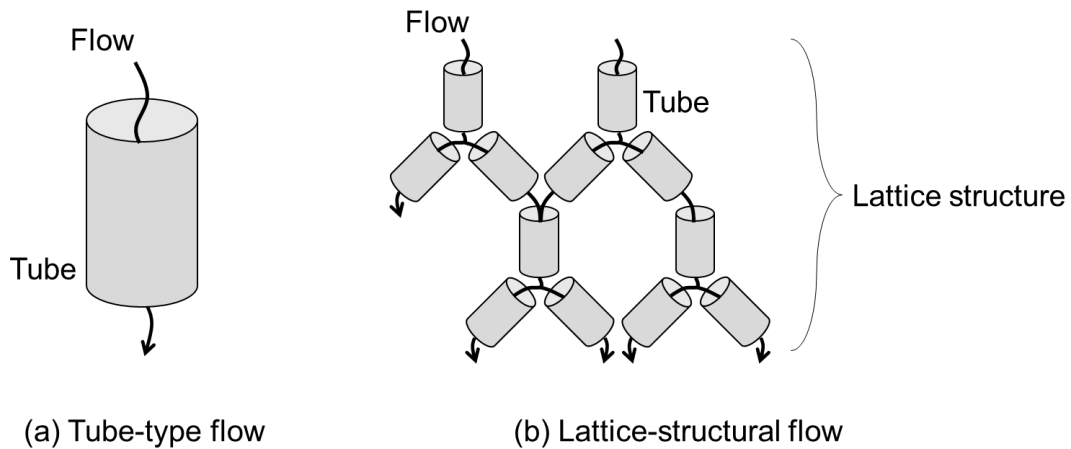
Figure 1-5 Schematic illustration of flows used in percolation theory: (a) tube-type flow and (b) lattice-structural flow.

The values of the percolation threshold for some structures have already been identified experimentally [23-27]. The percolation threshold values for the tube, lattice, and two dimensional plane structures can be easily estimated as they are very simple structures. However, a cell wall structure is too complex to calculate the percolation threshold. Therefore, a new parameter that can describe the structure of the cell wall needs to be identified to determine the percolation threshold and define the structure of stable metal foam.

Further, the influence of oxygen on the stability is not clear in the semi-solid route. To this end, metal foams must be fabricated in an atmosphere with different concentrations of oxygen. The oxygen in the atmosphere oxidizes the surface of the cell wall and raises the stability of the cell wall; however, to the best of our knowledge, there is no existing research on the effect of oxygen on the stability of the semi-solid route.

Comparative experiments are required to consider the effect of increasing the number of primary crystals and the oxygen in the atmosphere on the stability of the metal foam. However, a better technique is required to fabricate the metal foams with high reproducibility, especially under temperature control. The semi-solid route is sensitive to the temperature of the melt because the volume fraction of the solid can change easily with small variations in the temperature of the melt. Thus, the allowance fluctuations of the temperature during fabrication must be identified. In previous research, the temperature of the melt during the foaming process was not measured because the thermo-couple was pulled out before the foaming process. The temperature of the atmosphere in the furnace was used as the feedback value for controlling the temperature. For accurate temperature control, the calibrated temperature of the melt must be determined before conducting the comparative experiments.

There are two approaches to performing semi-solid processing: rheoforming and thixoforming [28]. The cast alloy of rheoforming is completely melted once and cooled slowly until the temperature of the slurry reaches the semi-solid state. After slow cooling, the primary crystals are grained using different methods. The slurry is cast into the mold while maintaining the temperature during the graining. The semi-solid route can be considered as one of the rheoforming processes. Chapter 1 introduces rheoforming and thixoforming, including the methods to grain the primary crystals. Thus, the most important parameter of semi-solid processing is the fraction of the solid. Since the fraction of the solid is considerably higher above around 50%, it is revealed through experiments that it decreases fluidity [29,30]. A semi-solid slurry that can be tensioned is not suitable for casting. Low fluidity generates casting defects such as misrun, and therefore, it is necessary to avoid an excessively high fraction of solid for casting using typical semi-solid processing methods. However, there has been no discussion on the low fraction of solid. The semi-solid route requires clarification of the minimum fraction of solid required to prevent drainage. This is very different from typical semi-solid processing and is a completely different approach.

This study aims to expand the clogging effect to the entire foam by adopting the percolation theory and reveal the effect of increasing the number of primary crystals and oxygen on the stability of metal foams. Further, the allowance fluctuation of the temperature of the melt is identified to conduct comparative experiments. The approaches used to achieve these objectives are summarized in Figure 1-6.
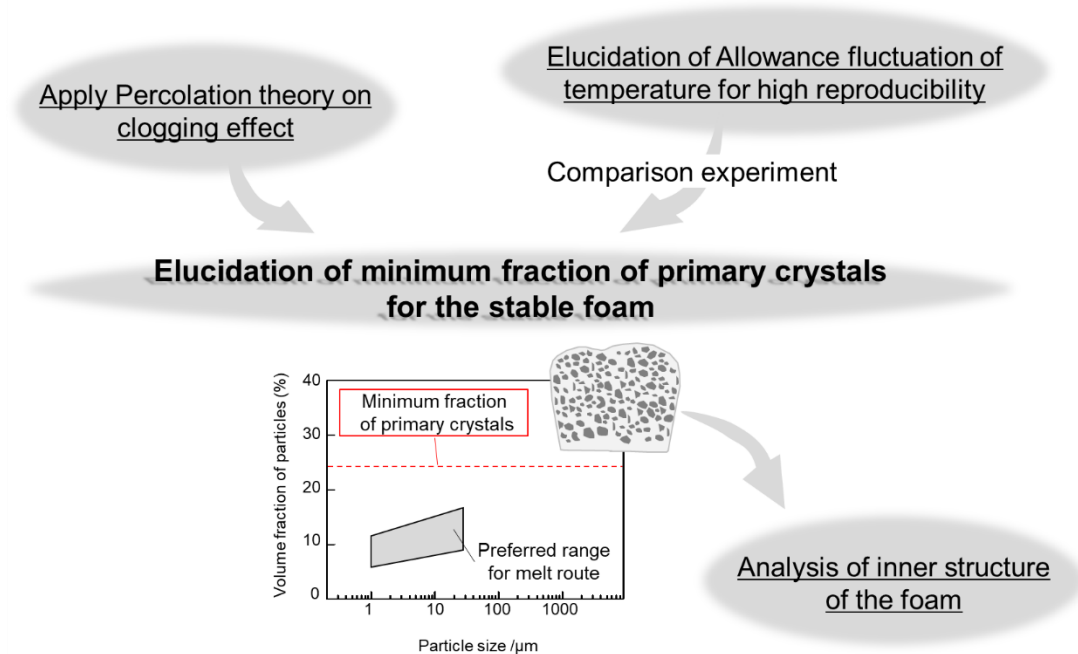
Figure 1-6 Schematic of the objectives of this study.

This study presents the stabilization mechanism of the semi-solid route based on the percolation theory. The allowance fluctuation of the temperature of the melt is identified to conduct comparative experiments, which reveal that oxygen in the atmosphere raises the stability of the metal foam. Further, the preferred ratio of primary crystals is identified using the stabilization mechanism and comparative experiments. The preferred ratio for the fabrication is expected to help accelerate the industrial use of the metal foam with high uniformity.

1.2. Fabrication methods for metal foams

1.2.1. Melt route

Melt route, which is one of the fabrication methods developed at an early date, can fabricate a metal foam with an anisotropic pore structure. Mechanical properties do not indicate isotropy, and therefore, future industrial usage is expected. Figure 1-7 illustrates the schematic of the fabrication processes involved in the melt route [16].

In the melt route, the basis alloy is completely melted at first, and then, a thickening agent is added to increase the apparent viscosity of the melt. TiH_2 is added as a blowing agent to the thickened melt, which is then stirred. The melt with the blowing agent is held for the foaming process while maintaining the temperature. During the foaming process, TiH_2 generates hydrogen gas because of thermal decomposition, thereby forming hydrogen bubbles within the melt. The metal foams are obtained by solidifying the foamed melt while retaining the internal pore structure.
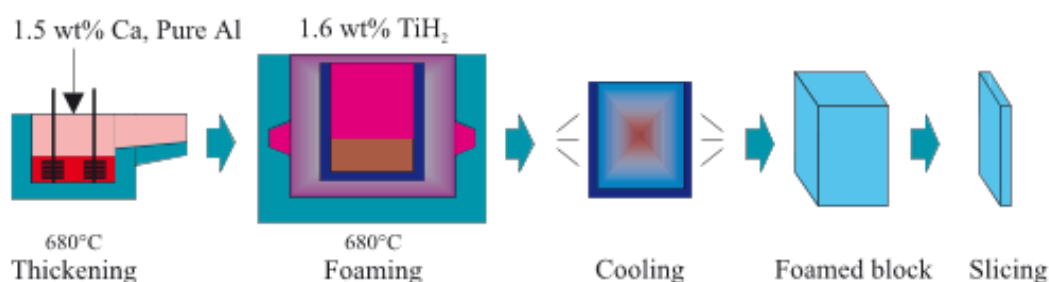
Figure 1-7 Manufacturing process of Alporas through the melt route [16]

1.2.2. Precursor method

method follows the same foaming process as the melt route. While the melt route adds the blowing agent directly into the molten metal and allow them to generate the gas, the precursor method adds the blowing agent into the ingot. The ingot including the blowing agent inside are then heated until the proper temperature. Gas is generated from the blowing agent while the ingot starts to melt to molten metal. Finally, the bubbles are formed inside the molten metal which was the ingot before. The metal foam is then obtained by solidifying the molten metal. The ingot, including the blowing agent, is referred to as the precursor.

There are two methods for fabricating precursors. In the first method, precursors are fabricated by blending the blowing agent and powdered base alloy and consolidating or sintering the mixture of the blowing agent and powdered metal into a block [31], which is called the precursor. In the second method, the blowing agent is blended into a metal ingot using friction stirring welding (FSW) [32]. In this case, the sintering process can be skipped. The precursor contains the blowing agent, and therefore, the ingot foams when heated with a halogen lump or heating plate. The foamed precursor does not retain its shape if the temperature becomes higher than the liquidus temperature.
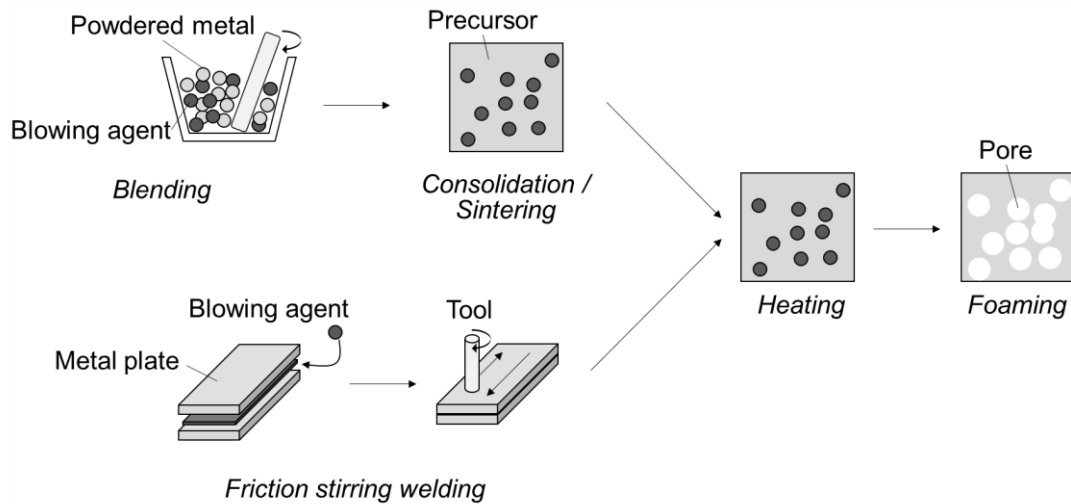
Figure 1-8 Schematic of the precursor method.

1.2.3. Gas injection method

Gas injection is one of the oldest fabrication methods. In this method, molten aluminum is pooled in a tundish. Subsequently, a nozzle is inserted into the molten aluminum, and the gas (O_2) is injected. The impeller attached to the edge of the nozzle stirs the gas, causing the gas to form small bubbles and flow upward. The foam structure is generated at the top of the molten metal. The belt conveyor scoops and transports the foam structure continuously.

This method is effective and convenient for fabricating large and plate-like aluminum foam. Many companies have utilized this method for fabricating aluminum foam for commercial use.
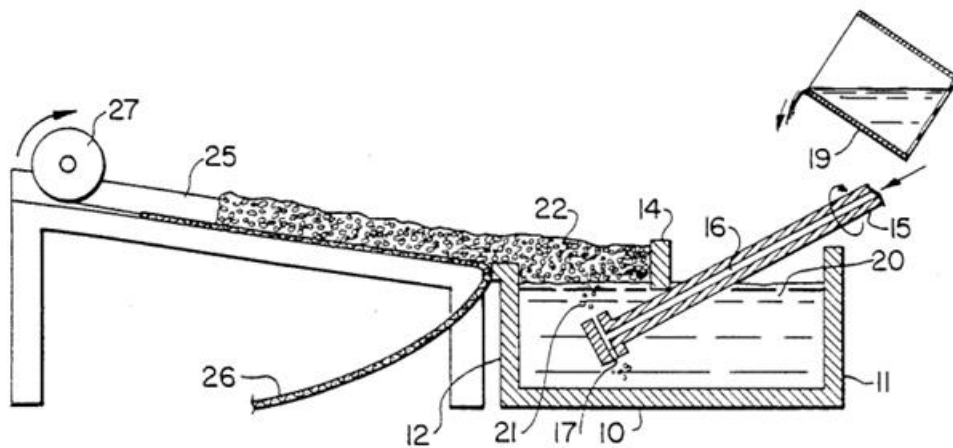
Figure 1-9 Schematic of the gas injection method [20].

1.3. Stabilization and prevention of drainage

1.3.1. Drainage

In the area between two pores, which is referred to as the cell wall, liquid flow exists along the direction of gravity. This liquid flow is referred to as drainage, which can cause the cell wall to rupture and pores to connect. The connected and coarse pores lower the mechanical property and pore morphology. Therefore, every fabrication method employs a process to prevent drainage. The most common process involves increasing the apparent viscosity of the liquid metal.

When the aluminum alloy foam is fabricated, the pore size increases proportionally with the foaming time, and the pore shapes become irregular, as shown in Figure 1-10[33]. To achieve stability in the pore structure, it is important to focus on the thinning of the cell walls along with the drainage.
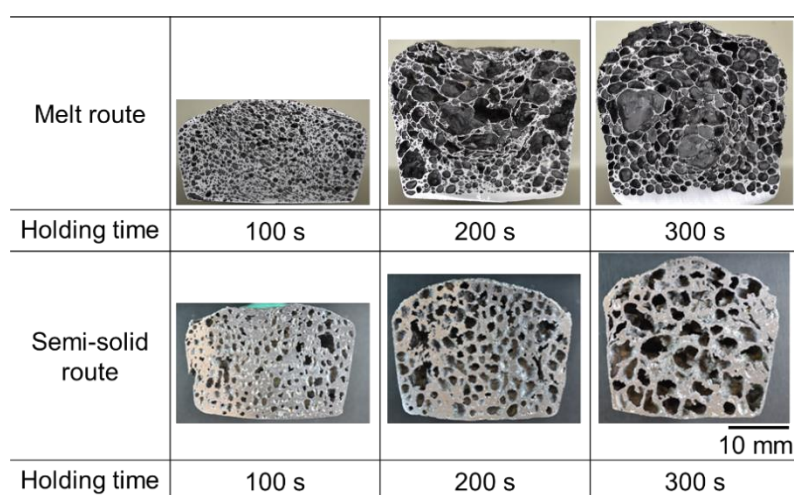
Figure 1-10 Porosity expanding with time in each fabrication process [33].

Figure 1-11(a) illustrates the cell structure within the metal foam. The cell structure comprises the cell walls and their nodes (plateau border). The basis alloy remains in a liquid or semi-solid state during the foaming and holding processes of each fabrication method. Hydrogen gas is generated because of the thermal decomposition of the foaming agent, thereby leading to the formation of pores. Over time, the pores grow larger, resulting in the drainage phenomenon (liquid flow due to the gravity force) at the cell wall. As the cell wall becomes thinner due to drainage, the curvature radius R of the pore and surface tension γ generate a capillary pressure ΔP described by Equation 1-1. Consequently, the molten metal influenced by the pressure inside the pore P_p is further drawn toward the plateau border, resulting in a thinner cell wall. Eventually, the excessive thinning of the cell wall ruptures the cell wall, resulting in the coalescence and enlargement of the neighboring pores (Figure 1-11(b)) [34].

$$\Delta P = \frac{\gamma}{R} \qquad\qquad (1-1)$$

(a)

(b)
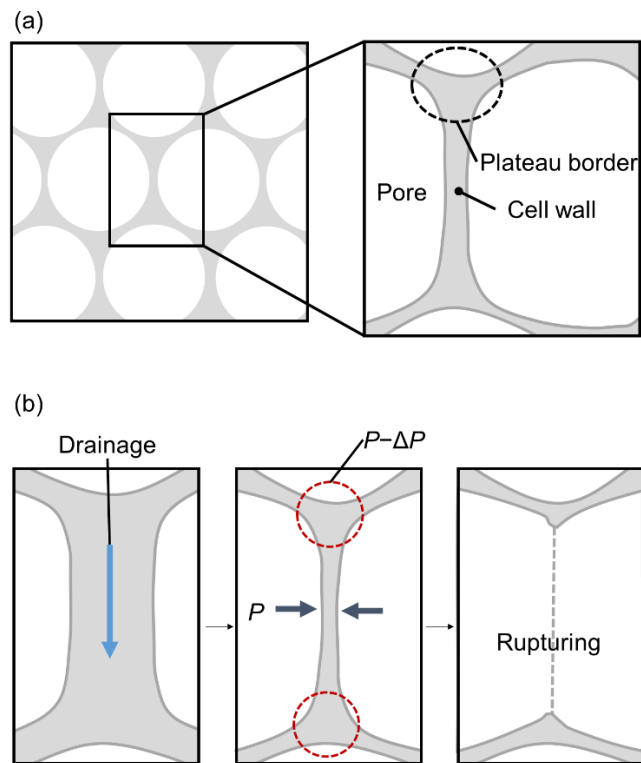
Figure 1-11 Schematic of the cell wall structure. (a) Cell wall and name of each part. (b) Stages of the cell wall until rupturing.

Although the thinning of the cell walls is inevitable, it can be delayed by increasing the viscosity of the melt. The impact of the viscosity-increasing agent on the thinning of the cell walls will be discussed in the next section.

1.3.2. Effect of the thickening agent on the cell wall

Figure 1-12 presents the schematic diagram reported by Heim *et al*., which shows the effect of thickening agents such as Mg and Ca (approximately 5 μm in size) used in the melt route on cell wall stabilization [21].
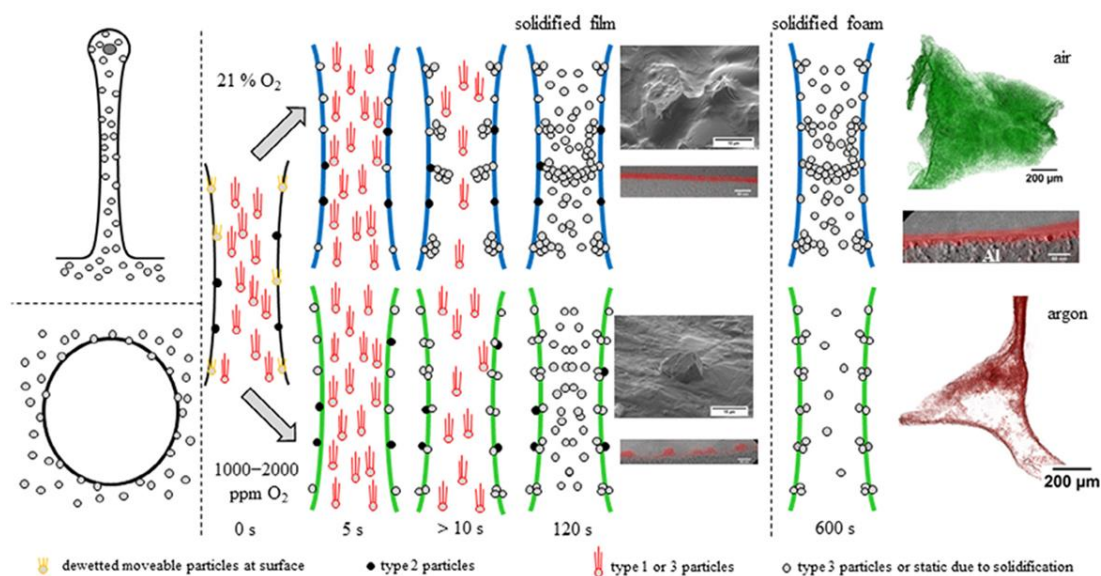
Figure 1-12 Schematic of the stabilization mechanism of the melt route [21].

Heim *et al*. simulated the cell walls using alloy films, as shown in Figure 1-13[21,22]. The alloy films were created by immersing them in molten metal and pulling them out to form a liquid film that mimics the cell walls between rings. They clarified their actions by observing the movement and behavior of the internal viscosity-increasing agent particles using X-ray tomography.
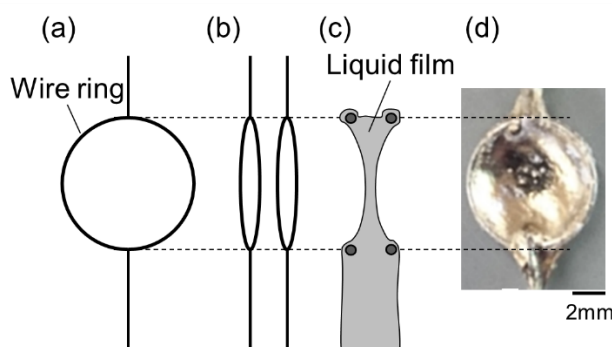
Figure 1-13 Schematic and image of the alloy film used for simulating the drainage of the cell wall.

The thickening agent within the cell walls flows predominantly under the influence of gravity during the initial stages of alloy film fabrication, as described in the upper scheme in Figure 1-12. However, smaller particles are more attracted to the liquid interface, resulting in the thickening

agent becoming fixed on the film surface. Gradually, other thickening agents become fixed in response to the influence of these agents, which leads to all thickening agents becoming fixed, as shown in the right scheme in Figure 1-12. This increases the apparent viscosity of the liquid film, thereby preventing drainage.

In the melt route, this stabilization mechanism is believed to occur in all cell walls within the foam. If all cell walls become stable, the foam inherently becomes stable, thereby maintaining its stability.

1.3.3. Effect of primary crystals on the cell wall

The effect of primary crystals on cell wall stability in the semi-solid route is yet to be elucidated. Kaya and Kuwahara revealed the effect of primary crystals on the stability of alloy films, as shown in Figure 1-14 [22]. To this end, they created alloy films similar to those created by Heim *et al.*, that is, within the semi-solid state of the melt, and they evaluated the primary crystals by observing the cross-section of the film. The observation revealed the presence of primary crystals with diameters of 50–70 μm on the upper part of the film, whereas coarse primary crystals with diameters exceeding 100 μm were unevenly distributed in the lower part of the film. This can be attributed to the gravitational effect, causing only the coarse primary crystals to flow down through the film. Further, the accumulation of the coarse primary crystals in the lower part obstructs the drainage pathway of the liquid film, thereby delaying the drainage phenomenon (Figure 1-14).
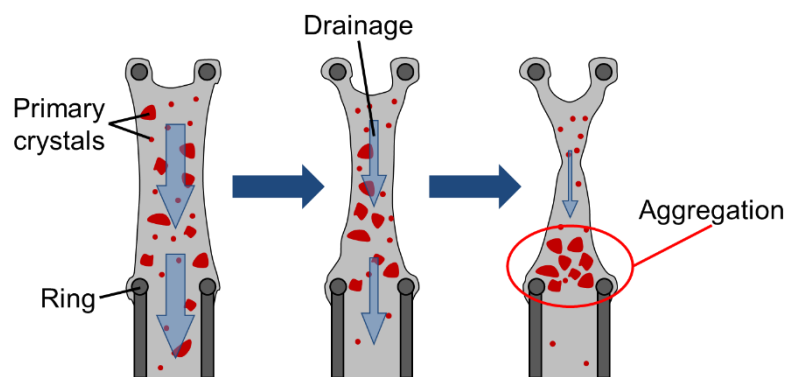
Figure 1-14 Schematic of the stabilization mechanism of the semi-solid route [22].

Kuwahara focused on the thinning of the film caused by the drainage of the liquid film and revealed that the cross-sectional area of the film decreases as the drainage progresses. In addition, the drainage phenomenon within the film can be considered as a Poiseuille flow with zero velocity at both ends because the film surface is oxidized and becomes a fixed end. This flow can be formulated using the Navier–Stokes equation. Figure 1-15 shows a model diagram of the flow. Assuming that the model diagram in Figure 1-15 has the boundary conditions of Poiseuille flow and the film surface forms a smooth curvature, the flow equation can be expressed as follows:

$$A_f = h_0 W_0 - \frac{1}{4\Delta W} \left\{ \frac{\pi}{2\Delta W} \left(h_0{}^2 - \Delta W^2 \right)^2 \frac{\theta}{360°} - \left(h_0{}^2 - \Delta W^2 \right) h_0 \right\} \tag{1-2}$$
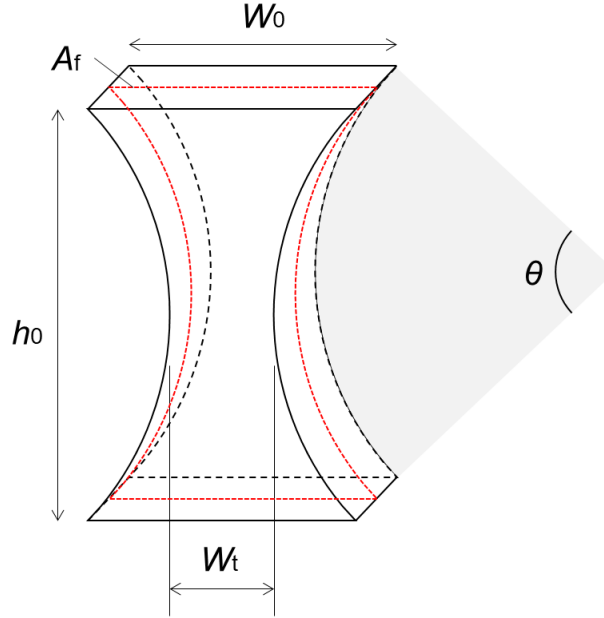
Figure 1-15 Schematic of the model diagram of flow.

In Equation 1-2, A_f, h_0, and W_0 represent the cross-sectional area of the film [m^2], height of the film [m], and maximum width of the film [m], respectively. In addition, ΔW is calculated using

$$\Delta W = W_0 - W_t \tag{1-3}$$

In Equation 1-3, W_t represents the time-varying minimum film thickness [m], which is calculated using

$$W_t = W_0 \sqrt{\frac{6\mu h_0}{\rho g t W_0^2 + 6\mu h_0}} \tag{1-4}$$

In Equation 1-4, μ, ρ, g, and t represent the viscosity of the melt [Pa·s], density [kg/m^3], acceleration due to gravity [m/s^2], and time [s], respectively.

The mechanisms mentioned in this section are related to the stability of the alloy film in the semi-solid state; however, it remains unclear if similar mechanisms occur within the cell walls inside the foam and whether they have an impact on the entire foam structure.

1.3.4. Stability of Foam Based on Particle Size and Volume Fraction of the Thickening Agent

Saito *et al*. conducted experiments to compare the stability of foams produced through in-situ observation using X-rays in the melt route and the semi-solid route [35]. The results showed that

the cell walls of foams fabricated through the semi-solid route lasted longer before rupturing compared to those fabricated through the melt route, thereby indicating that foams produced through the semi-solid route were more stable.

Jin *et al*. investigated the range of the particle size and volume fraction of the thickening agents that contribute to the stability of foams [20]. They revealed that the particle size and volume fraction of the thickening agent are important parameters influencing the stability of foams in the melt route. Figure 1-16 illustrates a graph of the particle size and volume fraction of the thickening agent for foam production.
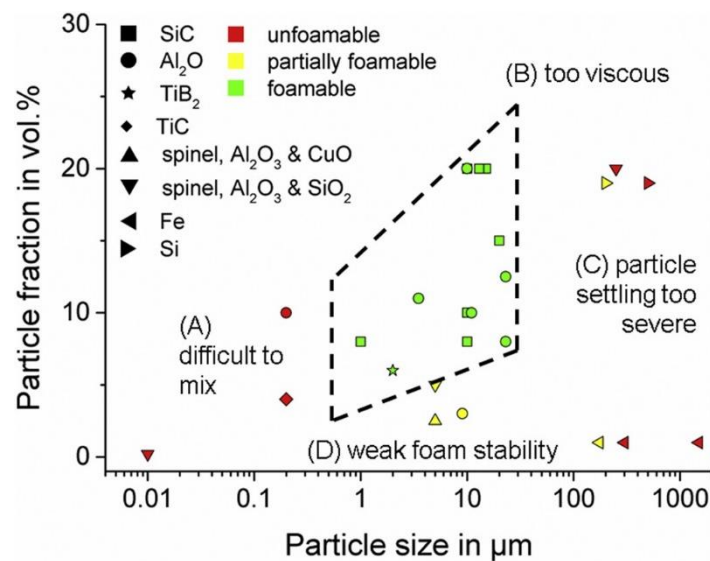
Figure 1-16 Graph of the particle size and volume fraction of the thickening agent for the fabrication [36].

Foams can be stably produced within the preferred range indicated by the black dashed line in the middle of the graph (particle size of approximately 0.5–20 μm) . However, in the study conducted by Saito *et al*., a thickening agent used in the semi-solid route, which is considered more stable, consists of primary crystals (indicated by black triangle ▶ in the figure), typically with particle sizes of around 200 μm. This size falls outside the range where particle arrangement is challenging, (Particle setting too severe) as shown in Figure 1-16. Therefore, this result indicates a different stabilization mechanism in the semi-solid route compared to that in the melt route.

The concept of percolation phenomena described by the theory of infiltration was introduced by Broadbent *et al*. in 1957 to represent the random infiltration of liquid within porous materials [37] Since then, percolation phenomena have been studied as percolation theory in various fields, with numerous applications reported.

1.4. Previous research on internal structure of porous metals

Open-cell porous metals are used as orthopedic materials and shock-absorbing materials in spacecraft [9,15,38]. Orthopedic applications such as bone implants and dental implants require sufficient transmittance for close contact with the base biomaterial part. In addition, a stiffness similar to that of the bone or the tooth is essential [10]. Shock-absorbing materials need to avoid a drop in the compressive stress, which can decrease the energy absorption efficiency. This phenomenon occurs when the plastic deformation of the cell walls localizes to one row of cells vertical to the compressive direction. This row of cells at which the deformation occurs is called the deformation band. As indicated in Figure 1-17, the strain at which the deformation occurs coincides with the strain at which the compressive stress drops [39]. The deformation band can also be observed in the compression test of closed-cell porous metals (Figure 1-18) [40]. Therefore, it is necessary to avoid generating the deformation band by optimizing the inner structure.
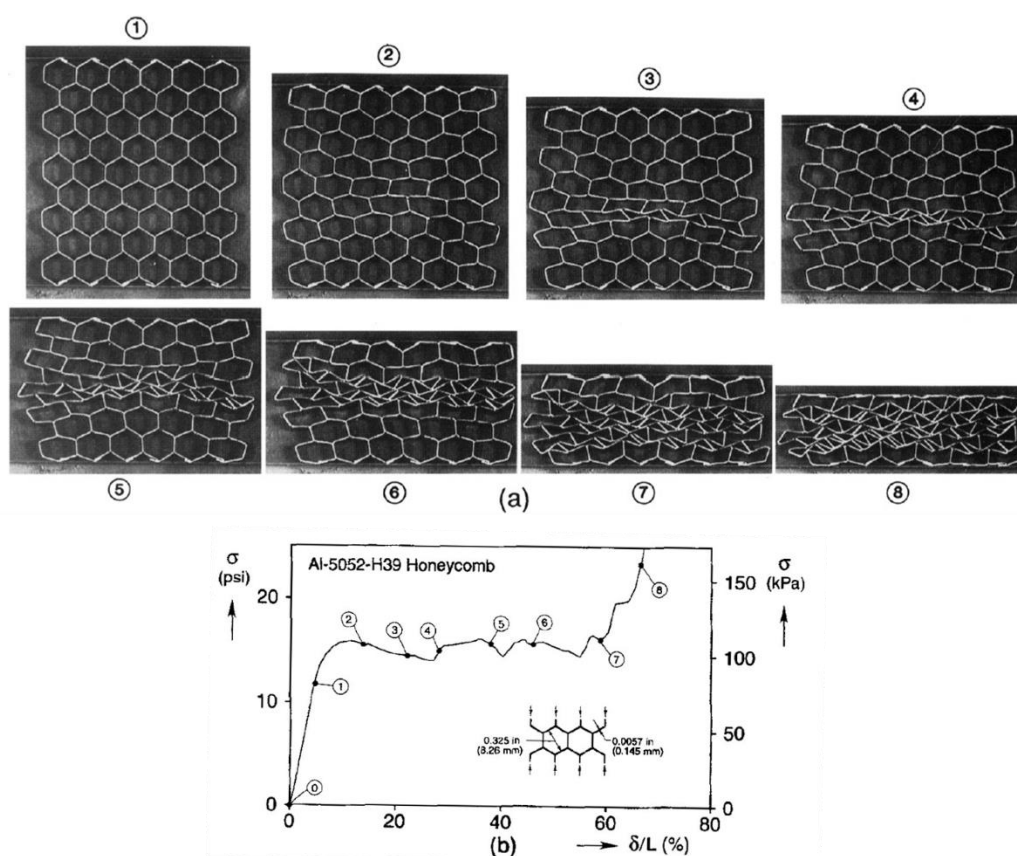
Figure 1-17 Crushing of the aluminum honeycomb specimen. (a) Sequence of deformed configurations. (b) Recorded load–displacement response [39].

Open-cell porous metals can be designed digitally and fabricated using advanced manufacturing technology. A typical design strategy involves using computer aided design (CAD),

including platonic and Archimedean polyhedral solids to determine the structure [9,15,38,41-44]. For a regularly arranged structure, the structure can be quantitatively expressed as FCC or BCC. Further, Voronoi tessellations are also used for designing the structure [15,45]. A Voronoi tessellation is a tessellation pattern in which a number of points scattered in a space is subdivided in some cells enclosing a plane closest to each point. The Voronoi tessellation allows faster modeling because the arbitrary structure can be generated by controlling the distance between the points. However, in the case of a random structure, there are few examples of uniform and quantitative definitions of the structure, which can only be expressed in terms of porosity and other properties.
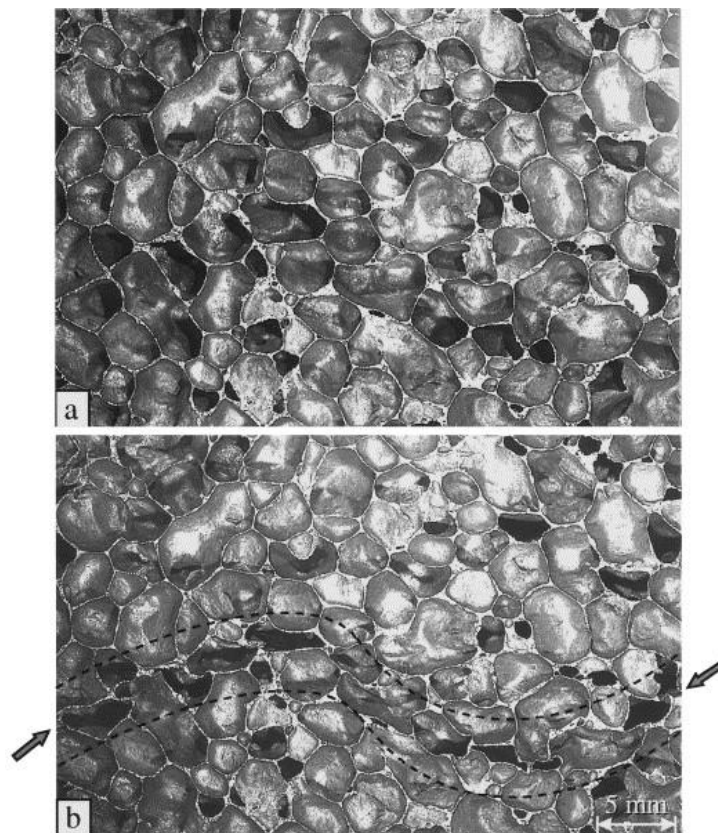
Figure 1-18 Optical images of the surface cells of the Alporas Al foam. (a) As received. (b) After strain $\epsilon A \approx 4.4\%$, which shows the collapse band indicated by the black dashed line and black arrows [40].

1.5. Previous research of semi-solid alloy and semi-solid die-casting

1.5.1. Weck's reagent

In this study, Weck's reagent was used to observe the growth of primary crystals during the fabrication process. Weck's reagent is prepared by dissolving potassium permanganate ($KMnO_4$) and sodium hydroxide (NaOH) in a 4:1 ratio. This reagent was developed by Weck *et al*. in 1986 and enables the etching of metal surfaces to reveal minor segregations in the crystals of Al-based alloys [46-

[49]

Figure 1-19 shows the microstructural image of an Al-7.0 mass% Si specimen before and after etching with Weck's reagent [48]. The specimen was remelted until it reached the semi-solid state, after which it was rapidly quenched by water cooling. The region indicated by the red arrows in the figure (located outside the black striped region within the microstructure) is colored by Weck's reagent, and it indicates the grown primary crystals (segregated regions).

(a)   (b)
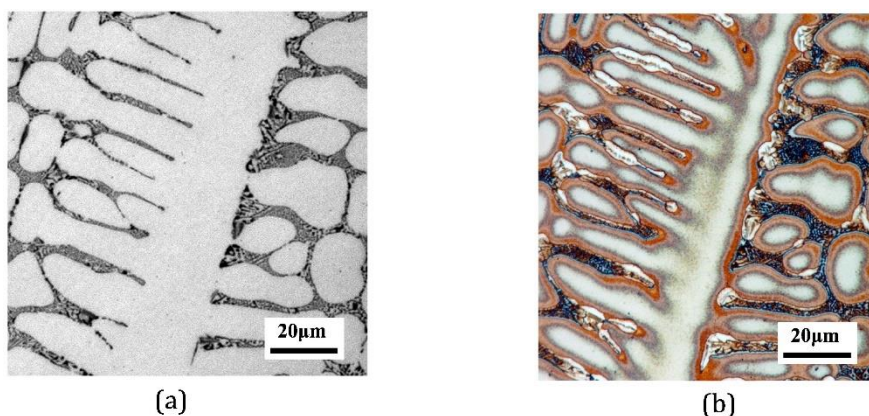
Figure 1-19 Microscopic images before and after etching with Weck's reagent [48].

1.5.2. Basis of Semi-Solid Processes

Since the 1990s, semi-solid processing has been developed for practical applications to utilize mechanical properties that emerge when metals undergo partial melting or solidification [50-52]. For example, metals in semi-solid slurry behave like fluids under shear forces while maintaining their self-supporting nature, thereby indicating that semi-solid slurry have properties of both solids and liquids.

Semi-solid processing can be broadly classified into two categories: rheoforming and [53] thixoforming. Rheoforming involves completely melting the metal and then cooling the molten metal to achieve a desired solid fraction, thereby resulting in a semi-solid slurry. Thixoforming involves heating an alloy with appropriate grained or equiaxed crystal structures to obtain a semi-solid slurry, with a high solid fraction. However, in both methods, it is necessary to crush and refine the solid phase (in most cases, the primary crystals) to prevent macro-segregation, which occurs due to the dendritic growth of the primary crystals and can lead to defects in the final product.

Therefore, various techniques have been investigated and industrialized for crushing and refining the primary crystals. For rheoforming, which is closely related to this study, the following methods have been explored.

1.5.3. Rheoforming

Rheoforming is a well-established semi-solid processing technique in the field of industrial

applications. Thus far, various rheoforming methods have been studied, which can be categorized as mechanical stirring, mechanical shearing, electromagnetic stirring, induced turbulence stirring, and other methods. These methods enable easier crushing of primary crystals.

i. Mechanical stirring with rotating items

The oldest and most straightforward method for crushing primary crystals, which relies on a well-understood physical phenomenon, is stirring the slurry using an agitator, as devised by Flemings *et al.* [28]. As shown in Figure 1-20(a), the molten alloy is transferred from the reservoir located at the upper part of the continuous rheocaster to the stirring unit with a cooling mechanism at the bottom. As a portion of the molten alloy solidifies, it is stirred by the impeller, thereby resulting in a highly flowable slurry that can be cast directly, as indicated in Figure 1-20(b). However, the challenges in stirring and discharging the high solid fraction mass zone, along with the severe wear of the impeller in the high-temperature molten metal, have hindered its practical implementation.
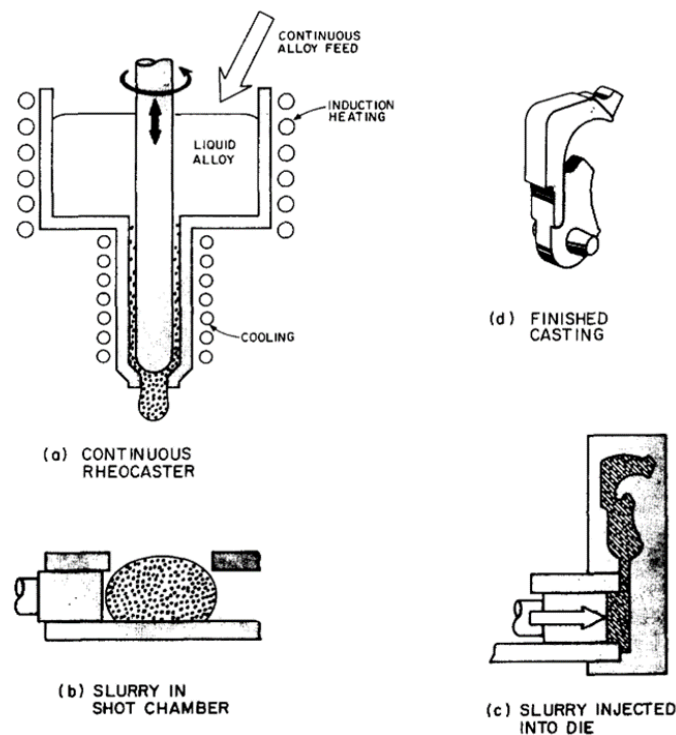
Figure 1-20 Schematic of the Rheocast process [28].

ii. Electromagnetic stirring (EMS)

An effective method for addressing issues such as agitator wear is electromagnetic stirring (EMS), which is widely employed in the continuous casting of steel. EMS is highly productive because it is not limited to specific molten metals [54-56]. In EMS, the solid phase is rotated by the shear forces generated by the electromagnetic field, which effectively plays the role of an agitator. Simultaneously,

the shear forces concentrate at the tips of dendrites, thereby causing their fragmentation and resulting in a highly flowable slurry with granular primary crystals. The image shown in Figure 1-21 illustrates the microstructures before (left) and after (right) stirring [57]. However, the dendritic structure is maintained in the unseen regions although the protrusions of the dendrites visible in Figure 1-22 undergo deformation.

Furthermore, studies involving the EMS of eutectic Al-Si alloys report that the centrifugal forces generated by electromagnetic stirring can lead to the coalescence of primary Si grains although the diameter of primary Si grains becomes finer [58].
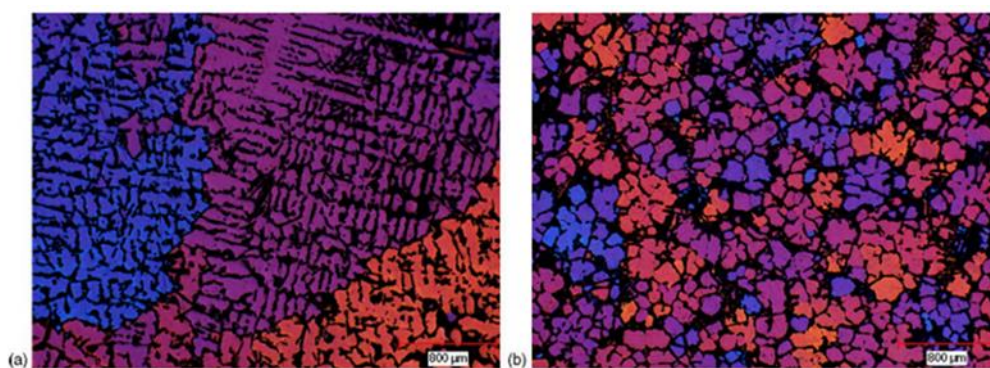
Figure 1-21 Microstructures before (left) and after (right) stirring with an impeller [57].
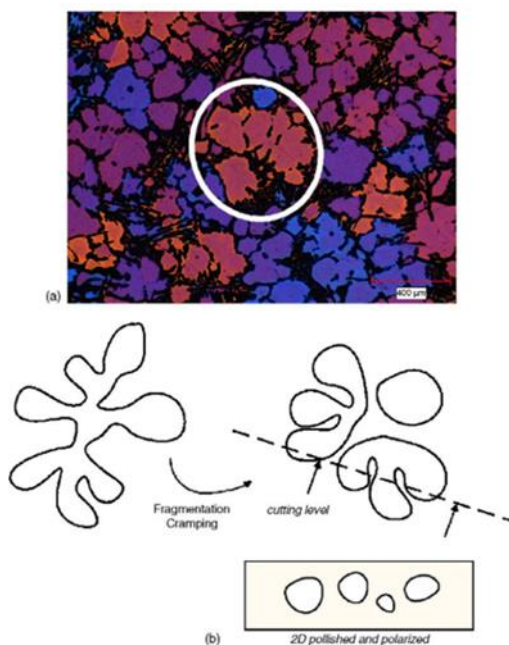
Figure 1-22 Schematic of the visible microstructure depending on the polished surface [57].

iii. Other methods

There are various other techniques for crushing primary crystals, which generally involve

approaches besides stirring. One such method involves using inclined cooling plates [59-61]. It is a simple technique where the molten metal flows along inclined plates cooled by a gas or a liquid, following gravity. The setup, as shown in Figure 1-23, is relatively simple. Turbulence is induced in the molten metal flowing over the cooling plates, which results in the fragmentation of primary crystals. The advantage of this method is the ease of adjusting the molten metal flow rate and cooling rate, which allows for easy control of the slurry characteristics by varying the length and angle of the cooling plates.
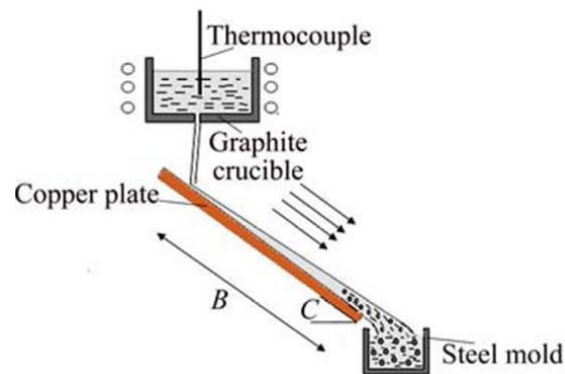
Figure 1-23 Schematic of the casting process using the inclined cooling plate [59].

Another innovative method among non-agitation approaches is the utilization of ultrasound (Figure 1-23) [62]. This method achieves both the crushing effect on primary crystals and the uniform dispersion of particles based on the application of ultrasound to the molten metal during the cooling process and subsequently agitating them.

1.6. Flow of liquid phase in solid phase

1.6.1. Fraction transmitted

In the field of semi-solid processing, a semi-solid slurry has conventionally been regarded as a porous medium through which fluid flows according to Darcy's law [63,64]. Darcy's law is used to model the behavior of semi-solid slurries. In this context, the generation of crystal structures and simulation of their behavior are considered.

The effect of dendritic crystals on preventing the movement of the liquid phase can be understood based on permeability, which is a measure of the ability of fluid to flow through a porous medium. During solidification in the semi-solid slurry state, permeability indicates the pressure drop associated with the flow of molten metal filling the voids formed by solidification shrinkage. Permeability is significant in processes such as semi-solid die casting because it influences the formation of casting defects, such as hot cracking, which determine the quality of the product [65]. Calculating the permeability can help simulate the behavior of dendritic crystals that hinder the

movement of the liquid phase, thereby contributing to the formation of casting defects.

In Japan, Takahashi *et al*. calculated the permeability of steel in the semi-solid slurry state using a circular cavity impregnation method [66]. They revealed that permeability decreases and fluidity significantly deteriorates as the solid fraction increases from 0.30 to 0.45 (Figure 1-24). This finding generally agrees with the observations by Ito *et al*. that dendritic crystals interconnect and form a complex lattice structure with an internal liquid phase, thereby reducing fluidity at a solid fraction of around 0.30.
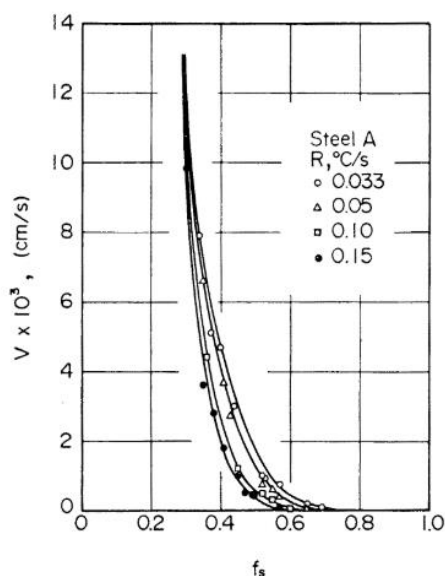
Figure 1-24 Relationship between permeability and fraction of solid [66].

Kareh *et al*. calculated the permeability of semi-solid slurries by observing their compressive behavior using X-ray tomography [67]. As shown in Figure 1-25(a), internal voids are formed when a semi-solid slurry is compressed because the overall volume increases owing to the compressive strain exerted when no liquid phase is supplied. Figure 1-25(c) shows a three dimensional rendering of the portion where the generated gas is involved in the liquid phase. This enables the calculation of permeability, which reveals the fluidity of semi-solid slurries at any desired solid fraction when cast. Since the 2000s, research has shifted towards simulating structures formed by dendritic crystals during the occurrence of decreased permeability to understand the dynamics of the actual process rather than solely determining permeability [52]. Sun *et al*. and Dijkstra *et al*. created models using Voronoi tessellation, as illustrated in Figure 1-26 [68,69]. They successfully introduced a curvature at grain boundaries by incorporating the Gibbs–Thomson effect into the simulations, yielding calculated permeability values that closely match experimentally obtained values, making the model more representative of actual semi-solid slurries.

Natsume *et al*. further developed simulations by modeling the three dimensional flow of the

liquid phase between dendritic trees [70]. They found that the permeability of the liquid flowing between dendritic trees significantly decreases at a solid fraction of around 0.3, which is consistent with previous research.
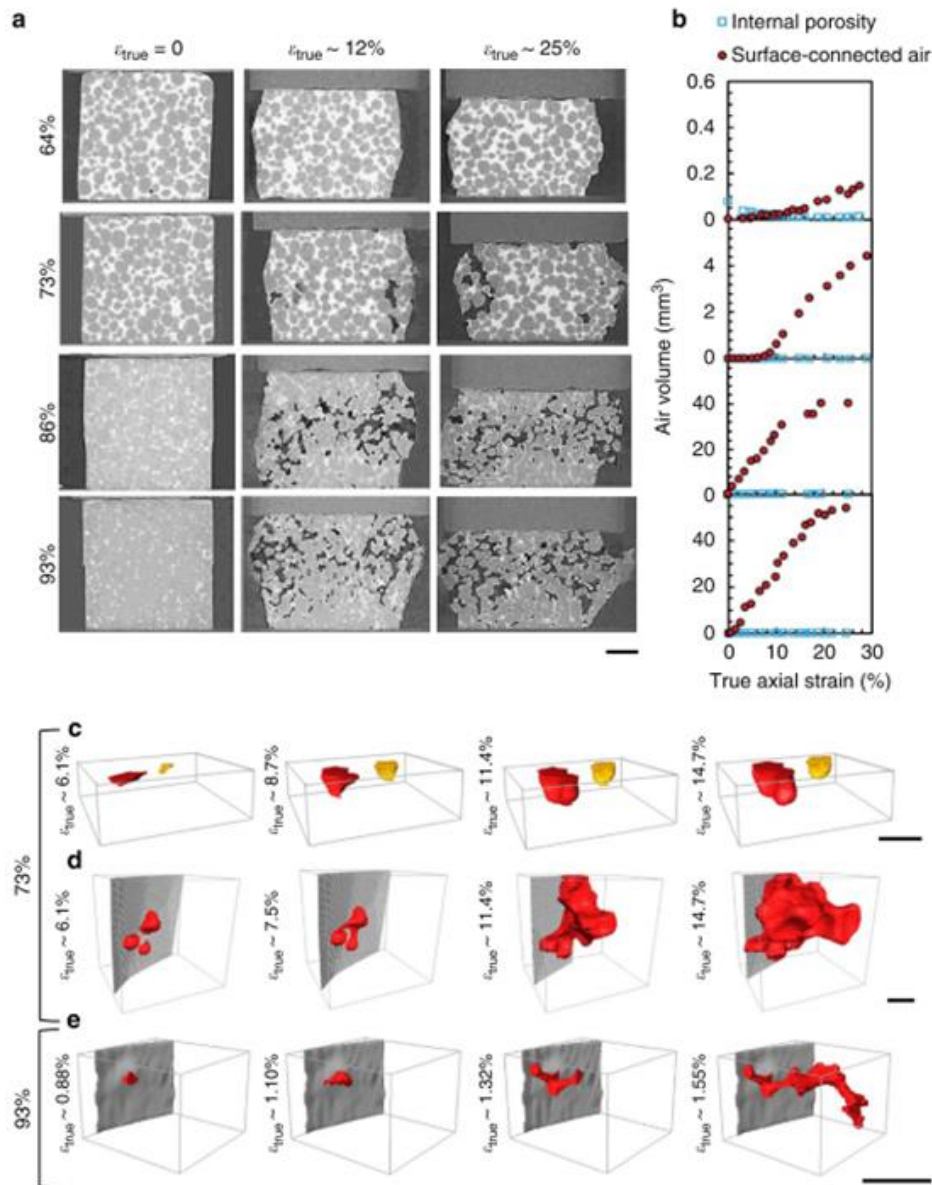
Figure 1-25 Compressive behavior of semi-solid slurry observed by X-ray. (a) Cross-sectional images of the semi-solid slurry under compression. (b) Change in porosity during compression. (c) 3D images of the generated gas involved in liquid phase [67].
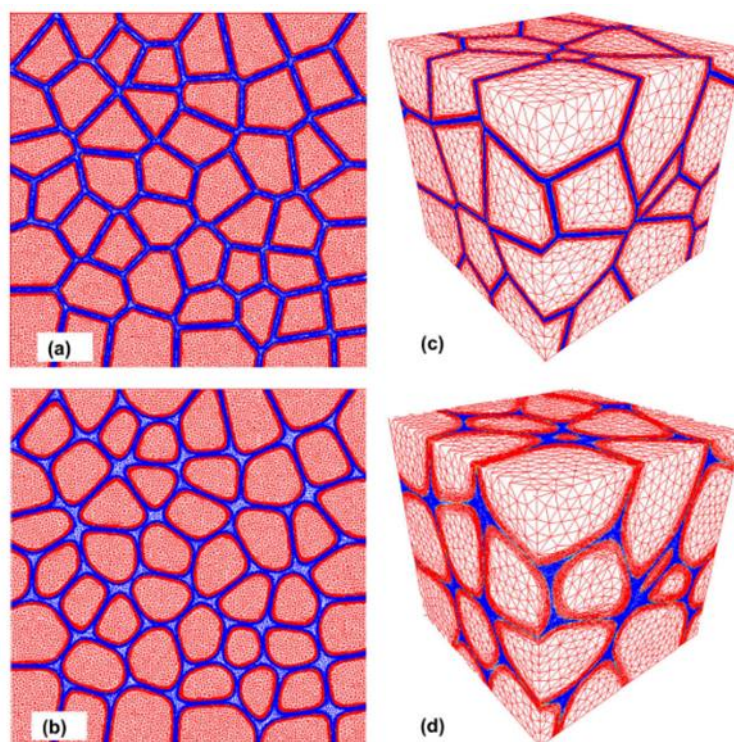
Figure 1-26 Calculation of permeability using Voronoi analysis [68].

1.6.2. Solidifying segregation caused by bridging effect

Previous studies focused on the flow of the liquid phase when examining the fluidity of slurries based on permeability. However, dendritic crystal bridging plays a significant role when considering the effect of the solid phase structure on fluidity. Bridging refers to the scenario wherein dendritic crystals growing from opposite mold surfaces extend toward each other and connect in the central region, assuming that the opposing mold surfaces are cooled. This phenomenon not only reduces the permeability of the liquid phase but also leads to centerline segregation, where a high concentration of solute remains in the central region.

Although bridging is closely related to permeability, dendritic crystals completely traverse and merge through the entire mold, completely blocking the flow of the liquid phase [71]. Therefore, simulations that consider bridging are necessary to understand the flow of the liquid phase between dendritic trees.

1.6.3. Percolation theory

Percolation theory is a theoretical framework that describes the number and properties of substances present in a system [72]. Substances within the system aggregate and form clusters, and when the proportion of clusters occupying the system, denoted as p, exceeds the percolation threshold p', the substances and clusters are interconnected within the system. Figure 1-27 illustrates the concept

of percolation and clusters in a system represented by a square lattice. As shown in the left scheme of Figure 1-27, the clusters and substances are not connected, thereby allowing other substances to move freely through the vacant lattice sites even when additional substances are introduced. However, as shown in the right scheme of Figure 1-27, clusters completely divide the system when clusters and substances are interconnected and permeate throughout the system from one end to the other. Consequently, other substances besides the clusters become immobile within the system.
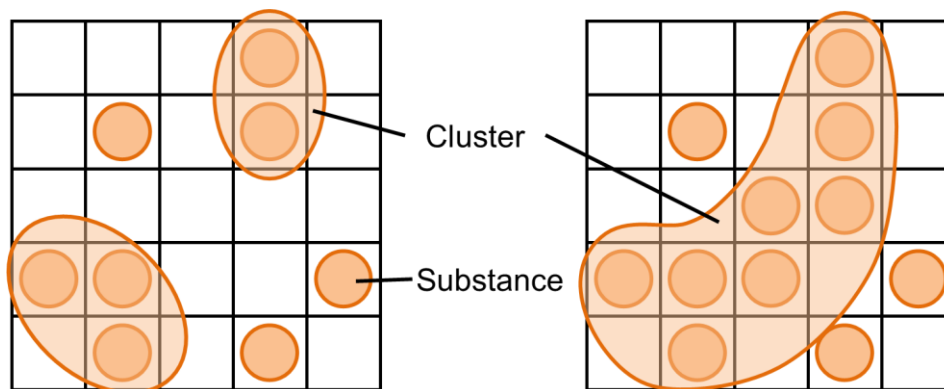
Figure 1-27 Schematic of clusters in a system based on percolation theory.

Percolation theory has been widely applied to analyze gas dynamics in porous magma during degassing processes, predict fire lifetimes in forest fires, and investigate the impact of high electrical resistance regions in conductive plates on overall conductivity. In the context of conductive plates, percolation theory suggests that the presence of high-resistance regions beyond a certain threshold renders the plate practically non-conductive even when some conducting paths remain. In other words, blocking a threshold number of pathways can be considered as the complete disconnection of pathways. Applying this concept to foams by considering cell walls as pathways and clusters as primary crystals, it is hypothesized that all cell walls are blocked if the primary crystals exceed the threshold, thereby resulting in a stable foam structure.

1.6.4. Monte Carlo method to calculate percolation threshold

Monte Carlo method is one of the calculation methods repeating algorithm generated randomly. Ulam and Neumann formulated the fundamental idea of this method, and it has been widely used until now [73].

There are two types of ways to calculate and obtain the percolation threshold; one is to conduct many experiments using a model, and the other is to perform numerical calculations (simulations). Particulary, the simulation is common way to treat a complex and massive amount of data.

The calcuation of the percolation threshold requires the calculation of the percolation

probability per every steps and the frequancy of the simulated phenomena. The percolation threshold is determined as the percolation probability when the simulated phenomena change rapidly. For example, in the simulation of the forest fire, the number of trees was deifnes as the percolation probability, and the fire lifetimes of the forest fire was defined as the phenomenon [74]. While there were limited clusters of the fire when the probability was 0.33 and 0.30, the fires spread widely when the percolation probability was 0.40 as indicated in Figure 1-28. In this case, clear difference between (a) and (b) estimates that the percolation threshold existed in the range of 0.33 to 0.4.
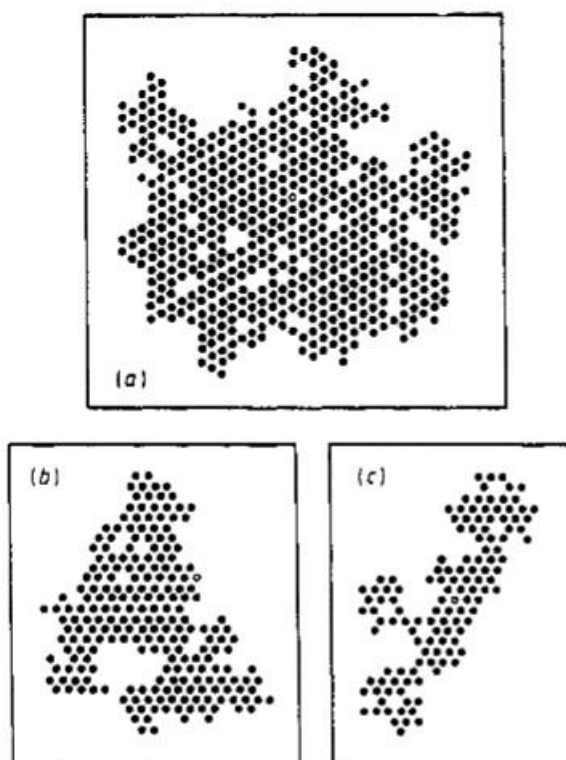
Figure 1-28 Simulation to calculate percolation threshold of forest fire by using Monte Carlo method. (a) Percolation probability is 0.40. (b) Percolation probability is 0.33. (c) Percolation probability is 0.30. The black circles represent the fire. The open circle represents the origin of the fire in each case.

Figure 1-29 shows the graph of the number of the burnt trees along with the time. As indicated in the graph, the number of the burnt trees increased when the probability was 0.40. On the other hand, the number of the burnt trees converged with 0.33 of the probability.
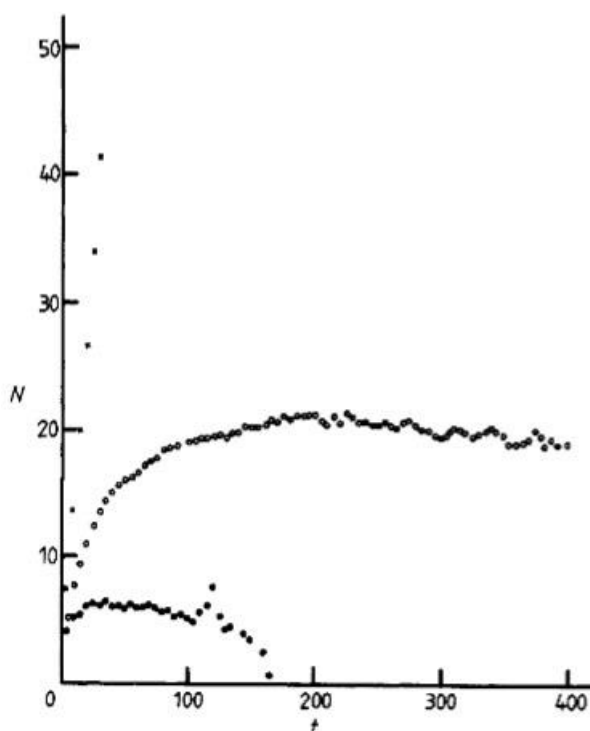
Figure 1-29 Number of burning trees with each percolation probability. The vertical axis *N* represents the number of burning trees and the horizontal axis *t* represents the time. Cross mark, open circle, and black circle indicate the cases shown in Figure 1(a-c), respectively.

In this study, the percolation probability for the foam is defined as the number of cell walls that can not go through. The phenomenon is defined as the number of paths from the top to the bottom of the foam. The percolation threshold is defined as the percolation probability when the number of the paths rapidly decreases.

1.7. Objectives and organization of this thesis

Developing and establishing a semi-solid route is imperative for fabricating stable foam. In this study, aluminum silicon alloy foams are fabricated, and their pore morphology, structure, and solid/gas boundary are observed to achieve the objectives below.

Chapter 1 presents an overview of the study and discussed certain associated issues including the mechanism of drainage prevention, analysis of the inner structure of the foam, and reproducibility of the fabrication method. The objectives of this study are three-fold.

1) Revealing the mechanism of drainage prevention based on the percolation theory.
2) Classifying the cell wall structure to define the stable structure.
3) Clarifying the effect of temperature and concentration of oxygen on the reproducibility of the semi-solid route.

Chapter 2 explains the mechanism used by the primary crystals to prevent drainage in the

entire foam. Both the cell wall and foam have their own referenced percolation thresholds for describing the required fraction of the obstacles to prevent drainage. The drainage is prevented when the presence of obstacles exceeds the percolation threshold. First, the cell walls, whose fraction of primary crystals exceeds the threshold of 0.58, are recognized as clogged cell walls. Subsequently, the ratio of the clogged cell walls to all cell walls is calculated. When this ratio exceeds the threshold of 0.33, drainage of the entire foam can be prevented.

Chapter 3 discusses the reproducibility of the semi-solid route among multiple experimental runs. Aluminum alloy foams are fabricated five times under the same setting fabrication conditions. The histories of the concentration of oxygen indicate high reproducibility. The history of the temperature of the melt shows the fluctuation in the temperature compared to the setting temperature. However, the pore morphologies, such as the pore diameter and circularity, do not change significantly when the change in the volume fraction of solid is less than 5%. Further, the preferred fraction range of the primary crystal is determined to be 15–35%. The preferred range is obtained from the results that indicate the relationship between the number of the clogged cell walls and volume fraction of solid. In addition, aluminum alloy foams are fabricated under different atmospheres by changing the concentration of oxygen and replacing the gas inside the furnace with Ar gas. The results indicate that aluminum alloy foams fabricated under 10 ppm oxygen have lower porosity compared with those fabricated under 18% oxygen. In addition, the foam fabricated under Ar gas has unstable pores with large diameters and low circularity. Therefore, oxygen is identified as a factor affecting the stabilization of the foam.

Chapter 4 clarifies the cell wall structure of the stable foam. Few extant studies have analyzed the structure of the stable foam using quantitative methods. In this study, the internal structure of the stable foam is observed using X-ray CT. The connection of inflows and outflows was focused on, which are always connected to one cell wall parallel to the direction of gravity. The number of inflows and outflows connected to the upside and downside of each cell wall parallel to gravity is counted, and the difference between the number of inflows and outflows is calculated. This number is defined as the new parameter δ, which is the cell wall structure. The results reveal that cell wall structures can be classified into 5 types, from $\delta = -2$ to $\delta = 2$. Monte Carlo method is conducted to calculate the percolation threshold of each cell wall structure, which reveals that the cell wall structure with a large value of $-\delta$ is more stable because the threshold is small. In addition, the pair distribution function of each cell wall structure is obtained, which indicates that the nearest neighbor structure is not the one that fills in the gap of the number δ. However, the total of the number δ of all cell walls is calculated as zero. Therefore, the structure of the stable foam is finally defined as the structure that compensates for the differences in each cell structure and brings the overall difference close to zero.
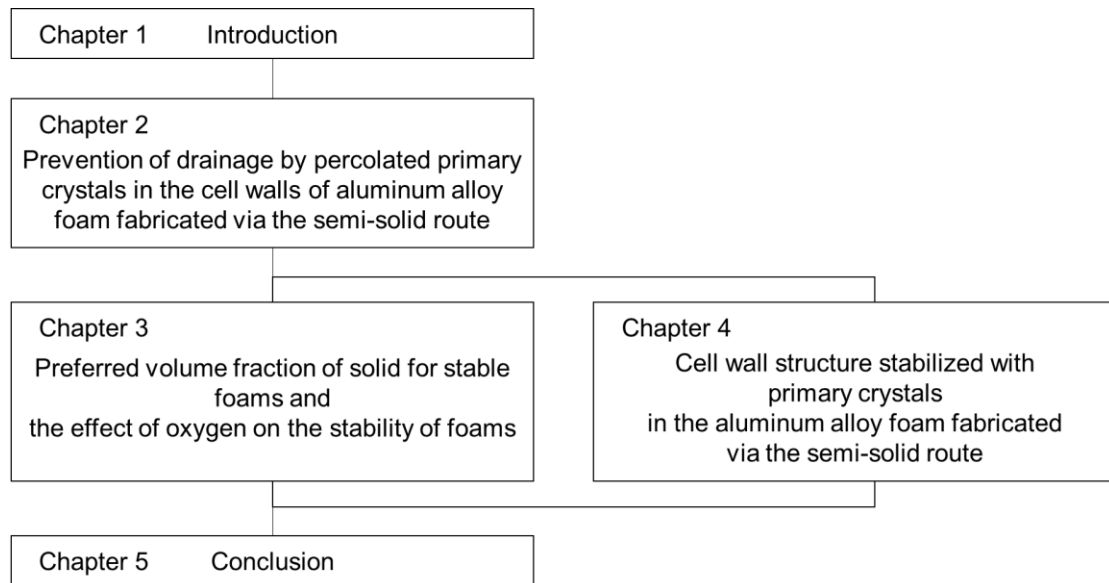
Figure 1-30 Structure of this thesis.

1.8. Summary

Thus far, I have described the previous research on the stabilization mechanisms in current foam aluminum alloys and introduced casting defects in the semi-solid process, their causes, as well as the latest simulation techniques and methods for resolving them. Kuwahara *et al*. proposed the phenomenon of the aggregation of primary crystals suppressing drainage and the damming effect, which bears a resemblance to the relationship between permeability and liquid flow. Although the permeability decreases as primary crystals grow in the semi-solid process, foam aluminum alloys exhibit a different behavior when granular primary crystals are initially gravitationally discharged to the lower region and accumulate there. Therefore, it is necessary to combine the knowledge of permeability used in the semi-solid process field with the insights from the field of physics, such as percolation theory, to investigate the drainage suppression or stabilization mechanisms of foam aluminum alloys comprehensively. In addition, the utilization of 3D simulation methods introduced in the previous section is essential for further validation. Therefore, this study aims to elucidate the stabilization mechanisms of foam aluminum alloys produced by the semi-solid foam method based on 3D percolation theory and conduct more efficient and generalized investigations through simulations.

References in Chapter 1

[1] J. Banhart: Manufacture, Characterisation and Application of Cellular Metals and Metal Foams. *Progress in Materials Science,* **46** (2001) *6*, 559-632, doi: 10.1016/S0079-6425(00)00002-5.

[2] J. Banhart and H. Seeliger: Recent Trends in Aluminum Foam Sandwich Technology. *Advanced Engineering Materials,* **14** (2012) *12*, 1082-1087, doi: 10.1002/adem.201100333.

[3] M.F. Ashby, Evans T, Fleck NA, Hutchinson JW, Wadley HNG, Gibson LJ. *Metal Foams: A Design Guide.* 1st ed. (Butterworth-Heinemann, MA, USA, 2000) .

[4] F. García-Moreno: Commercial Applications of Metal Foams: Their Properties and Production. *Materials,* **9** (2016) *2*, 85, doi: 10.3390/ma9020085.

[5] R. Watanabe, T. Kobayashi, Y. Otomo, A. Akisawa, Y. Ueda, and K. Enoki: Experimental Investigation into the Heat Transfer and Pressure Drop Performance of Sintered High Porosity Media. *Applied Thermal Engineering.,* **196** (2021), 117284, doi: 10.1016/j.applthermaleng.2021.117284.

[6] "Architectural". https://www.cymat.com/ (accessed 28th Nov., 2023).

[7] "Filtration". https://alupor.com/filtration (accessed 28th Nov., 2023).

[8] "General industry". http://www.foamtechglobal.co.kr/product#general (accessed 28th Nov., 2023).

[9] G. Ryan, A. Pandit, and D.P. Apatsidis: Fabrication Methods of Porous Metals for use in Orthopaedic Applications. *Biomaterials,* **27** (2006) *13*, 2651-2670, doi: 10.1016/j.biomaterials.2005.12.002.

[10] X. Tong, Z. Shi, L. Xu, J. Lin, D. Zhang, K. Wang, Y. Li, and C. Wen: Degradation Behavior, Cytotoxicity, Hemolysis, and Antibacterial Properties of Electro-Deposited Zn–Cu Metal Foams as Potential Biodegradable Bone Implants. *Acta Biomaterialia,* **102** (2020), 481-492, doi: 10.1016/j.actbio.2019.11.031.

[11] A. Ataee, Y. Li, D. Fraser, G. Song, and C. Wen: Anisotropic Ti-6Al-4V Gyroid Scaffolds Manufactured by Electron Beam Melting (EBM) for Bone Implant Applications. *Materials & Design,* **137** (2018), 345-354, doi: 10.1016/j.matdes.2017.10.040.

[12] V. Hejtmanek and P. Capek: 3D Microstructure Modeling of Porous Metal Filters. *Metals,* **2** (2012) *3*, 344-352, doi: 10.3390/met2030344.

[13] A.J. Otaru, H.P. Morvan, and A.R. Kennedy: Airflow Measurement Across Negatively Infiltration Processed Porous Aluminum Structures. *AIChE Journal,* **65** (2019) *4*, 1355-1364, doi: 10.1002/aic.16523.

[14] K. Kitazono: Design of impact energy absorbing system based on porous aluminum. *Journal of The Japan Institute of Light Metals,* **67** (2017) *11*, 559-563, doi: 10.2464/jilm.67.559. (written in Japanese).

[15] K. Kitazono, K. Matsuo, T. Hamaguchi, and Y. Fujimori: Design of Energy-Absorbing Materials for Space Crafts Based on Voronoi Diagrams. *Proceedings of the 11th International Conference on Porous Metals and Metallic Foams (MetFoam 2019):* 11th International Conference on Porous Metals and Metallic Foams (MetFoam 2019) 20-23 Aug, 2019); Anonymous Eds.: (Springer International Publishing, Switzerland, 2020), pp. 3-10.

[16] T. Miyoshi, M. Itoh, S. Akiyama, and A. Kitahara: ALPORAS Aluminum Foam: Production Process, Properties, and Applications. *Adv Eng Mater,* **2** (2000) *4*, , doi: 10.1002/(sici)1527-2648(200004)2:4<179::aid-adem179>3.0.co;2-g.

[17] T. Miyoshi: Production Process, Properties and Applications of Closed-Cell Aluminum Foam. **74** (2002) *12*, 835-839, (written in Japanese).

[18] T. Hanafusa and K. Ohishi: Making of Porous Metallic Material by the Semi-solid Aluminum Alloy. *BULLETIN OF HIROSHIMA PREFECTURAL TECHNOLOGY RESEARCH INSTITUTE EASTERN REGION INDUSTRIAL RESEARCH CENTER,* (2010) *23*, 28-29, (written in Japanese).

[19] K. Heim, G.S.V. Kumar, F. Garcia-Moreno, I. Manke, and J. Banhart: Drainage of Particle-Stabilised Aluminium Composites through Single Films and Plateau Borders. *Colloids and Surfaces. A, Physicochemical and Engineering Aspects,* **438** (2013), 85-92, doi: 10.1016/j.colsurfa.2013.02.019.

[20] I. Jin, Kenny LD, and Sang H: Method of producing lightweight foamed metal. United States Patent 4,973,358. (1990).

[21] K. Heim, G.S. Vinod-Kumar, F. García-Moreno, A. Rack, and J. Banhart: Stabilisation of Aluminium Foams and Films by the Joint Action of Dispersed Particles and Oxide Films. *Acta Materialia,* **99** (2015), 313-324, doi: 10.1016/j.actamat.2015.07.064.

[22] T. Kuwahara, A. Kaya, T. Osaka, S. Takamatsu, and S. Suzuki: Stabilization Mechanism of Semi-Solid Film Simulating the Cell Wall during Fabrication of Aluminum Foam. *Metals,* **10** (2020) *3*, 333, doi: 10.3390/met10030333.

[23] S.C. van der Marck: Percolation Thresholds and Universal Formulas. *Physical Review. E, Statistical Physics, Plasmas, Fluids, and Related Interdisciplinary Topics,* **55** (1997) *2*, 1514-1517, doi: 10.1103/PhysRevE.55.1514.

[24] X. Feng, Y. Deng, and H.W.J. Blöte: Percolation Transitions in Two Dimensions. *Physical Review. E, Statistical, Nonlinear, and Soft Matter Physics,* **78** (2008) *3 Pt 1*, 031136, doi: 10.1103/PhysRevE.78.031136.

[25] C.R. Scullard and R.M. Ziff: Predictions of Bond Percolation Thresholds for the Kagomé and Archimedean (3, 122) Lattices. *Physical Review. E, Statistical, Nonlinear, and Soft Matter Physics,* **73** (2006) *4 Pt 2*, 045102, doi: 10.1103/PhysRevE.73.045102.

[26] R.G. Arenhart, G.M.O. Barra, and C.P. Fernandes: Simulation of Percolation Threshold and Electrical Conductivity in Composites Filled with Conductive Particles: Effect of Polydisperse Particle Size Distribution. *Polymer Composites,* **37** (2016) *1*, 61-69, doi: 10.1002/pc.23155.

[27] P.N. Suding and R.M. Ziff: Site Percolation Thresholds for Archimedean Lattices. *Physical Review. E, Statistical Physics, Plasmas, Fluids, and Related Interdisciplinary Topics,* **60** (1999) *1*, 275-283, doi: 10.1103/physreve.60.275.

[28] M.C. Flemings, R.G. Riek, and K.P. Young: Rheocasting. *Materials Science and Engineering,* **25** (1976), doi: 10.1016/0025-5416(76)90057-4.

[29] C. Limmaneevichitr, S. Pongananpanya, and J. Kajornchaiyakul: Metallurgical Structure of A356 Aluminum Alloy Solidified Under Mechanical Vibration: An Investigation of Alternative Semi-Solid Casting Routes. *Materials in Engineering,* **30** (2009) *9*, 3925-3930, doi: 10.1016/j.matdes.2009.01.036.

[30] M. Paes and E.J. Zoqui: Semi-Solid Behavior of New Al–Si–Mg Alloys for Thixoforming. *Materials Science & Engineering A, Structural Materials :,* **406** (2005) *1-2,* 63-73, doi: 10.1016/j.msea.2005.07.018.

[31] F. Baumgärtner, I. Duarte, and J. Banhart: Industrialization of Powder Compact Toaming Process. *Advanced Engineering Materials,* **2** (2000) *4*, 168-174, doi: 10.1002/(SICI)1527-2648(200004)2:43.0.CO;2-O.

[32] Y. Hangai and T. Utsunomiya: Fabrication of Porous Aluminum by Friction Stir Processing. *Metall Mater Trans A,* **40** (2009) *2*, 275-277, doi: 10.1007/s11661-008-9733-9.

[33] T. Kuwahara, M. Saito, T. Osaka, and S. Suzuki: Effect of Primary Crystals on Pore Morphology during Semi-Solid Foaming of A2024 Alloys. *Metals,* **9** (2019) *1*, 88, doi: 10.3390/met9010088.

[34] J. Banhart, G.S. Vinod-Kumar, P.H. Kamm, T.R. Neu, and F. García-Moreno: Light-Metal Foams: Some Recent Developments. *Ciência & Tecnologia Dos Materiais,* **28** (2016) *1,* 1-4, doi: 10.1016/j.ctmat.2016.06.002.

[35] M. Saito and Shinsuke Suzuki: In-situ observation of foam evolution of liquid and sei-solid A2024 alloy through X-ray radioscopy. *Proceedings of the 9th International Conference on Porous Metals and Metallic Foams (MetFoam 2015),* (accepted).

[36] K. Heim, F. García-Moreno, and J. Banhart: Particle Size and Fraction Required to Stabilise Aluminium Alloy Foams Created by Gas Injection. *Scripta Materialia,* **153** (2018), 54-58, doi: 10.1016/j.scriptamat.2018.04.041.

[37] S.R. Broadbent and J.M. Hammersley: Percolation Processes. *Mathematical Proceedings of the Cambridge Philosophical Society,* **53** (1957) *3,* 629-641, doi: 10.1017/S0305004100032680.

[38] X. Wang, S. Xu, S. Zhou, W. Xu, M. Leary, P. Choong, M. Qian, M. Brandt, and Y.M. Xie: Topological Design and Additive Manufacturing of Porous Metals for Bone Scaffolds and Orthopaedic Implants: A Review. *Biomaterials,* **83** (2016), 127-141, doi: 10.1016/j.biomaterials.2016.01.012.

[39] S.D. Papka and S. Kyriakides: In-Plane Compressive Response and Crushing of Honeycomb. *Journal of the Mechanics and Physics of Solids,* **42** (1994) *10,* 1499-1532, doi: 10.1016/0022-5096(94)90085-X.

[40] A. Bastawros, H. Bart-Smith, and A.G. Evans: Experimental Analysis of Deformation Mechanisms in a Closed-Cell Aluminum Alloy Foam. *Journal of the Mechanics and Physics of Solids,* **48** (2000), 301-322, doi: 10.1016/s0022-5096(99)00035-6.

[41] A. Takezawa, Y. Koizumi, and M. Kobashi: High-Stiffness and Strength Porous Maraging Steel Via Topology Optimization and Selective Laser Melting. *Additive Manufacturing,* **18** (2017), 194-202, doi: 10.1016/j.addma.2017.10.004.

[42] C. Lin, T. Wirtz, F. LaMarca, and S.J. Hollister: Structural and Mechanical Evaluations of a Topology Optimized Titanium Interbody Fusion Cage Fabricated by Selective Laser Melting Process. *Journal of Biomedical Materials Research. Part A,* **83A** (2007) *2,* 272-279, doi: 10.1002/jbm.a.31231.

[43] J. Parthasarathy, B. Starly, and S. Raman: A Design for the Additive Manufacture of Functionally Graded Porous Structures with Tailored Mechanical Properties for Biomedical Applications. *Journal of Manufacturing Processes,* **13** (2011) *2,* 160-170, doi: 10.1016/j.jmapro.2011.01.004.

[44] N. Taniguchi, S. Fujibayashi, M. Takemoto, K. Sasaki, B. Otsuki, T. Nakamura, T. Matsushita, T. Kokubo, and S. Matsuda: Effect of Pore Size on Bone Ingrowth into Porous Titanium Implants Fabricated by Additive Manufacturing: An in Vivo Experiment. *Materials Science & Engineering C,* **59** (2016), 690-701, doi: 10.1016/j.msec.2015.10.069.

[45] O.E. Sotomayor and H.V. Tippur: Role of Cell Regularity and Relative Density on Elasto-Plastic Compression Response of Random Honeycombs Generated using Voronoi Diagrams. *International Journal of Solids and Structures.,* **51** (2014) *21-22*, 3776-3786, doi: 10.1016/j.ijsolstr.2014.07.009.

[46] E. Weck, Leistner E. *Metallographic Instructions for Colour Etching by Immersion. II. Beraha Colour Etchants and their Different Variants.* (DVS GmbH, Düsseldorf, 1983) .

[47] L. Gao, Y. Harada, and S. Kumai: Microstructural Characterization of Aluminum Alloys using Weck's Reagent, Part II: Coloring Mechanism. *Materials Characterization,* **107** (2015), 434-452, doi: 10.1016/j.matchar.2015.05.006.

[48] L. Gao, Y. Harada, and S. Kumai: Microstructural Characterization of Aluminum Alloys using Weck's Reagent, Part I: Applications. *Materials Characterization :,* **107** (2015), 426-433, doi: 10.1016/j.matchar.2015.01.005.

[49] L. Gao, Y. Harada, and S. Kumai: Analysis of Microstructure Evolution and Precise Solid Fraction Evaluation of A356 Aluminum Alloy during Partial Re-Melting by a Color Etching Method. *J Mater Sci,* **47** (2012) *18*, 6553-6564, doi: 10.1007/s10853-012-6585-x.

[50] B.G. Thomas and Bellet M: Modeling of Stress, Distortion, and Hot Tearing. *Casting* 1st ed. (ASM International, 2008).

[51] D.G. Eskin, Suyitno, and L. Katgerman: Mechanical Properties in the Semi-Solid State and Hot Tearing of Aluminium Alloys. *Progress in Materials Science,* **49** (2004) *5*, 629-711, doi: 10.1016/S0079-6425(03)00037-9.

[52] J.A. Spittle and S.G.R. Brown: Numerical Modelling of Permeability Variation with Composition in Aluminium Alloy Systems and its Relationship to Hot Tearing Susceptibility. *Materials Science and Technology,* **21** (2005) *9*, 1071-1077, doi: 10.1179/174328405X51839.

[53] H.V. Atkinson: Semisolid Processing of Metallic Materials. *Materials Science and Technology,* **26** (2010) *12*, 1401-1413, doi: 10.1179/026708310X12815992418012.

[54] W.R. Loué and M. Suéry: Microstructural Evolution during Partial Remelting of Al☐Si7Mg Alloys. *Materials Science & Engineering A, Structural Materials :,* **203** (1995) *1-2,* 1-13, doi: 10.1016/0921-5093(95)09861-5.

[55] E.J. Zoqui, M.T. Shehata, M. Paes, V. Kao, and E. Es-Sadiqi: Morphological Evolution of SSM A356 during Partial Remelting. *Materials Science & Engineering A, Structural Materials :,* **325** (2002) *1-2,* 38-53, doi: 10.1016/S0921-5093(01)01401-0.

[56] S. Chayong, H.V. Atkinson, and P. Kapranos: Thixoforming 7075 Aluminium Alloys. *Materials Science & Engineering. A, Structural Materials : Properties, Microstructure and Processing,* **390** (2005) *1*, 3-12, doi: 10.1016/j.msea.2004.05.004.

[57] S. Nafisi, D. Emadi, M.T. Shehata, and R. Ghomashchi: Effects of Electromagnetic Stirring and Superheat on the Microstructural Characteristics of Al–Si–Fe Alloy. *Materials Science & Engineering A, Structural Materials :,* **432** (2006) *1-2,* 71-83, doi: 10.1016/j.msea.2006.05.076.

[58] D. Lu, Y. Jiang, G. Guan, R. Zhou, Z. Li, and R. Zhou: Refinement of Primary Si in Hypereutectic Al–Si Alloy by Electromagnetic Stirring. *Journal of Materials Processing Technology,* **189** (2007) *1-3,* 13-18, doi: 10.1016/j.jmatprotec.2006.12.008.

[59] H. Khosravi, R. Eslami-Farsani, and M. Askari-paykani: Modeling and Optimization of Cooling Slope Process Parameters for Semi-Solid Casting of A356 Al Alloy. *Transactions of Nonferrous Metals Society of China =,* **24** (2014) *4*, 961-968, doi: 10.1016/S1003-6326(14)63149-6.

[60] T. Motegi, K. Kondou, R. Chi, and S. Aoyama: Continuous Casting of Semisolid Al-Di-mg Alloy. *Proceeding of the 4th Decennial International Conference on Solidification Processing:* 4th Decennial International Conference on Solidification Processing 7-10 July, 1997); Anonymous Eds.: (Department of Engineering Materials, University of Sheffield, Sheffield, UK, pp. 14-16.

[61] S.G. Shabestari, H. Saghafian, F. Sahihi, and M.H. Ghoncheh: Investigation on Microstructure of Al-25 Wt-%Mg2Si Composite Produced by Slope Casting and Semi-Solid Forming. *International Journal of Cast Metals Research (Online),* **28** (2015) *3*, 158-166, doi: 10.1179/1743133614Y.0000000143.

[62] J. Jiang and Y. Wang: Microstructure and Mechanical Properties of the Semisolid Slurries and Rheoformed Component of Nano-Sized SiC/7075 Aluminum Matrix Composite Prepared by Ultrasonic-Assisted Semisolid Stirring. *Materials Science & Engineering A, Structural Materials :,* **639** (2015)350-358, doi: 10.1016/j.msea.2015.04.064.

[63] B. Šarler and R. Vertnik: A Numerical Benchmark Test for Continuous Casting of Steel III. *IOP Conference Series.,* **84** (2015) *1,* 012056, doi: 10.1088/1757-899X/84/1/012056.

[64] P.D. Lee, A. Chirazi, and D. See: Modeling Microporosity in Aluminum–silicon Alloys: A Review. *Journal of Light Metals,* **1** (2001) *1,* 15, doi: 10.1016/s1471-5317(00)00003-1.

[65] Z. Sun, R.E. Logé, and M. Bernacki: 3D Finite Element Model of Semi-Solid Permeability in an Equiaxed Granular Structure. *Computational Materials Science,* **49** (2010) *1*, 158-170, doi: 10.1016/j.commatsci.2010.04.042.

[66] T. Takahashi, M. Kudoh, and S. Nagai: Estimation of Effective and Specific Permeability in the Mushy Zone of Steel Ingot by the Method of Seepage into Cylindrical Hole. *Tetsu to Hagane,* **68** (1982) *6*, 623-632, doi: 10.2355/tetsutohagane1955.68.6_623. (written in Japanese).

[67] K.M. Kareh, P.D. Lee, R.C. Atwood, T. Connolley, and C.M. Gourlay: Revealing the Micromechanisms Behind Semi-Solid Metal Deformation with Time-Resolved X-Ray Tomography. *Nature Communications,* **5** (2014) *1*, 4464, doi: 10.1038/ncomms5464.

[68] Z. Sun, R.E. Logé, and M. Bernacki: 3D Finite Element Model of Semi-Solid Permeability in an Equiaxed Granular Structure. *Computational Materials Science,* **49** (2010) *1*, 158-170, doi: 10.1016/j.commatsci.2010.04.042.

[69] W.O. Dijkstra, C. Vuik, and L. Katgerman: Network Model of Fluid Flow in Semi-Solid Aluminum Alloys. *Computational Materials Science,* **38** (2006) *1*, 67-74, doi: 10.1016/j.commatsci.2006.01.007.

[70] Y. Natsume: Numerical Simulation of Macrosegregation Formed due to Solidification Shrinkage and Bridging of Solidification Structures. *Tetsu to Hagane,* **103** (2017) *12*, 738-746, doi: 10.2355/tetsutohagane.TETSU-2017-062.

[71] H. Jacobi and K. Wünnenberg: Final Solidification, Centre Segregation and Precipitation Phenomena in Continuously Cast Round Billets. *Steel Res,* **68** (1997) *6*, 258-265, doi: 10.1002/srin.199701787.

[72] D. Stauffer, Aharony A. *Introduction to Percolation Theory / by Dietrich Stauffer and Ammon Aharony.* 2nd ed. (Taylor & Francis, an imprint of Taylor and Francis, Boca Raton, FL, 2014) .

[73] R. Eckhardt: Stan Ulam, John Von Neumann, and the Monte Carlo Method. *Los Alamos Science,* **15** (1987), 131-137.

[74] G. MacKay and N. Jan: Forest Fires as Critical Phenomena. *Journal of Physics A: Mathematical and General,* **17** (1984), L757-L760

Chapter 2

Prevention of drainage by percolated primary crystals

in the cell walls of aluminum alloy foam

fabricated via the semi-solid route

2. Prevention of drainage by percolated primary crystals in the cell walls of the aluminum alloy foam fabricated via the semi-solid route

2.1. Introduction

Drainage in the cell walls must be prevented to fabricate uniform metal foams. In the melt route, the apparent viscosity is increased by adding a thickening agent [1]. This thickening agent is an impurity for the base alloy, and therefore, there is a risk of lowering the mechanical properties of the metal foam. The semi-solid route does not use any thickening agent and instead uses primary crystals [2]. These primary crystals aggregate in a cell wall and prevent drainage [3]; this effect is referred to as the clogging effect, which is considered one of the stabilization mechanisms of the semi-solid route. However, the clogging effect has only been confirmed in an alloy film that simulated one cell wall in a metal foam. There is no clarity regarding primary crystals preventing drainage in actual cell walls in aluminum alloy foams. In addition, the prevention of drainage in the entire foam is yet to be observed. Therefore, the mechanism of the clogging effect in the entire foam needs to be established. Further, the minimum amount of primary crystals in the cell wall required to fabricate a stable foam needs to be determined.

The drainage phenomenon occurs equally in both cell walls and foams, and the drainage of the entire foam involves the lattice structure formed by numerous cell walls when observing this phenomenon on a macroscopic scale. However, calculating the amount of primary crystals required for drainage prevention is difficult through macro-scaled observations. Preventing only one of the many complex flows cannot help to effectively control the drainage of the entire foam. Instead, it is easier to calculate how many flows comprising the lattice structure should be prevented to prevent the drainage in the entire foam. Observing the drainage phenomenon on a microscopic scale indicates that drainage within the cell walls occurs through a single flow path. Calculating the amount of primary crystals required to prevent drainage through a single flow path is relatively straightforward. Thus, it is possible to determine whether the drainage of the entire foam can be prevented by counting the number of cell walls in which the drainage is prevented and calculating the percentage of those cell walls over all cell walls.

Percolation theory, which can describe liquid flow in a variety of structures [4], can solve these issues. Liquid flow can be prevented when the ratio of obstacles in the liquid flow (percolation probability) exceeds the percolation threshold. For the metal foam, there are two types of flow structures: tube-type flow and lattice-structural flow. The former describes the drainage in a cell wall. The cell wall is considered as the tube; the drainage of molten metal, liquid flow; and primary crystals, obstacles. Therefore, the minimum amount of primary crystals required for fabricating stable foams can be determined by adopting the percolation theory. The lattice-structural flow describes the

drainage in the entire foam. Each side in a lattice structure is a cell wall, and therefore, the lattice structure is considered a combination of the tube-type flows. The clogging effect can be expanded into the entire foam because of this combination.

Even if the clogging effect does work in actual metal foams, the effect does not always work on all cell walls. The key factor here is why a cell wall without primary crystals exhibits stability. Further, the necessary fraction of primary crystals is yet to be identified even for the case where the clogging effect works properly on one cell wall. Moreover, the quantity of "clogged cell walls" required for the stabilization of metal foams remains known. Percolation theory can explain why flow is inhibited even if it is not completely blocked by obstacles, thereby enabling us to investigate the effect of primary crystals on metal foams.

Thus, this chapter aims to suggest the stabilization mechanism of aluminum alloy foam in the semi-solid route that employs primary crystals. To this end, an aluminum alloy foam was fabricated via the semi-solid route, and subsequently, the primary crystals inside the metal foam were observed. Further, the length ratio of the primary crystals was measured considering the percolation theory.

2.2. Materials and Methods

Each fabrication process, including the casting process of the master alloy and the foaming process of the aluminum alloy foam, were conducted in 2015 by Mr. Ryunosuke Kochi (Graduated in 2016). Section 2.2.1, 2.2.2, and 2.2.3 explains the fabrication processes conducted by Mr. Kochi. The analysis processes after Section 2.2.4 were conducted by the author of this thesis (Ms. Satomi Takamatsu).

2.2.1. Fabrication apparatus

Figure 2-1 shows the fabrication apparatus used in this chapter. Figure 2-1(a) and 2-1(b) show an actual photograph of the exterior of the electric furnace and a schematic illustration of the interior of the furnace, respectively. The impeller located at the electric furnace was angled to stir the semi-solid slurry effectively. The details of the impeller are presented in Figure 2-1.
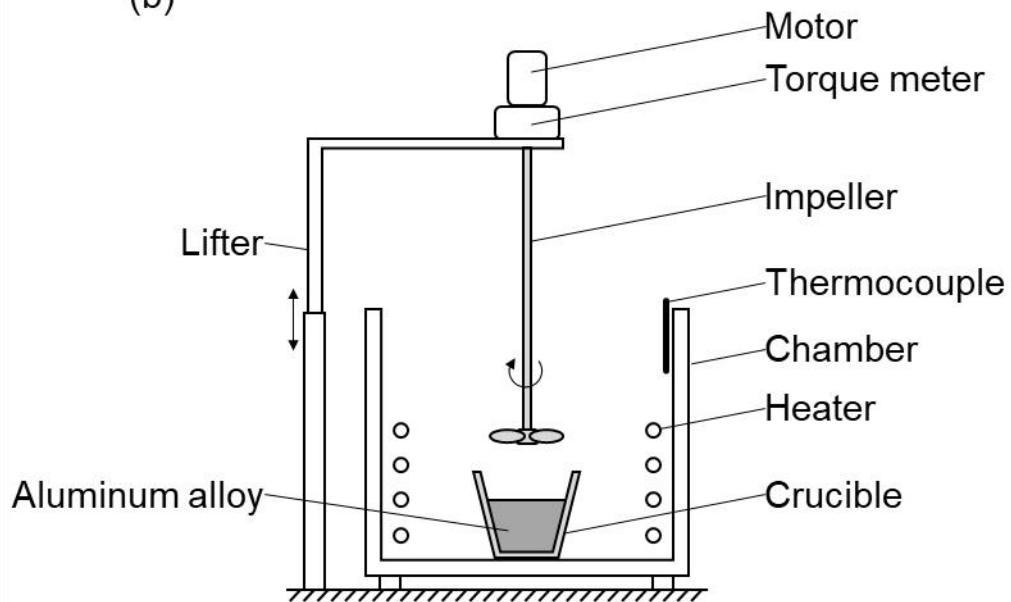
**Figure 2-1 Electronic furnace used in this study. (a) Exterior image of the furnace. (b)
Schematic of the electronic furnace.**

2.2.2. Casting process for the master alloy

Figure 2-2 presents the schematic of the casting process of the master alloy. High-purity aluminum ingots and Al-25.3 mass% Si ingots (Table 2-1) were weighed to satisfy Equation 2-1.
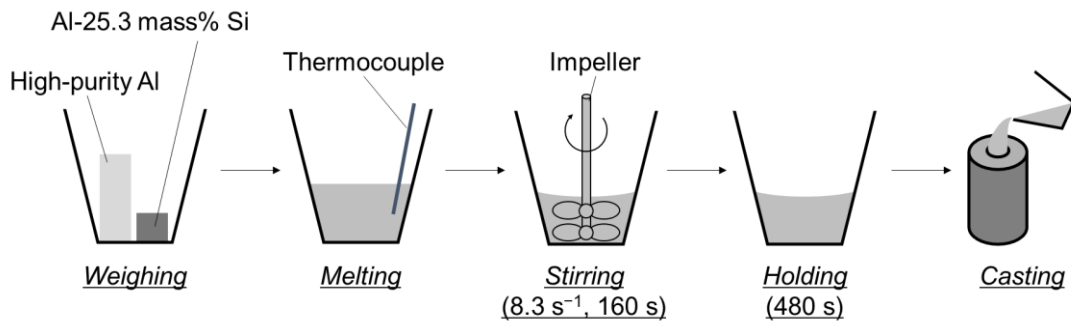
Figure 2-2 Schematic of the fabrication process for casting the Al-6.4 mass% Si alloy from high-purity aluminum and Al-25.3 mass% Si alloy.

$$6.4 = \frac{25.3 \times x}{x + y} + \frac{0.004 \times y}{x + y} \qquad (2-1)$$

where, x and y represent the mass of the Al-25.3 mass% Si alloy and the high-purity aluminum, respectively.

The weighed alloys were set together in a stainless crucible to ensure that the silicon content was 6.4 mass%. The crucible was coated with Aron Ceramic (Toagosei Co., Ltd, Tokyo, Japan), which is a heat-resistant inorganic adhesive filler made of SiO_2, to avoid the chemical reaction between iron and aluminum. The ingots were heated in an electronic furnace in air till the temperature reached 800 °C. Subsequently, the melt was stirred by rotating two impellers made of stainless at 8.3 s^{-1} for 160 s. The surfaces of the impeller and the shaft connected to the impeller were coated with Aron Ceramic. The size and angle of the impellers are shown in Figure 2-3. The angles of the upper and lower impellers were set to 60° and 30°, respectively.
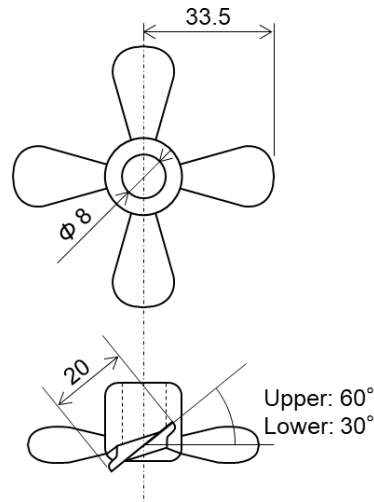
Figure 2-3 Size and angle of the impellers used for stirring.

After stirring, the melt was kept still for 480 s and then sand-cast in a mold (ϕ 30 mm $\times$ 315 mm in length). The cast material was used as the master alloy.

Table 2-1 Chemical composition of the high-purity aluminum and Al-25.3 mass% Si alloy

Element	Si	Fe	Cu	Al
High-purity aluminum (mass%)	0.004	0.003	0.0001	Bal.
Al-Si (mass%)	25.3	0.15	0.00	Bal.

2.2.3. Foaming process

Figure 2-2 shows a schematic of the fabrication process of the aluminum alloy foam via the semi-solid route. First, 70 g of the master alloy was weighed, and then, it was placed on a stainless-steel crucible coated with Aron Ceramic and boron nitride. The master alloy was then heated to 800 °C and completely melted in the electronic furnace in air. A type-K thermocouple was set to measure the temperature of the melt. The temperature of air in the furnace measured using another type-K thermocouple was used as the feedback temperature for the power output of the heater controlled with a proportional–integral–derivative (PID) controller. The melt was slowly cooled to solidify the primary crystals (primary α) until the semi-solid slurry temperature reached 615 °C. According to the Al-Si binary phase diagram, the volume fraction of solid is 12% when the temperature of the Al-6.4 mass% Si alloy is 615 °C [5]. The volume fraction of solid is a fraction of the solid phase (primary crystals in this study) existing in the solid-liquid mixture (semi-solid slurry). In this study, the volume fraction of solid is indicated as f_s, and defined as an important parameter that represents the condition of each fabricated foam. After the temperature stabilized at 615 °C, TiH_2 wrapped in an aluminum foil (100 $\times$ 100 mm^2) was added into the semi-solid slurry as a blowing agent so that the content of TiH_2 became

1 mass% of the alloy. TiH_2 was dry treated at 150 °C for 24 h previously. The thermocouple was removed from the slurry after adding TiH_2. The semi-solid slurry was stirred with a rotating impeller at a speed of 15 s^{-1} for 100 s to disperse the TiH_2 and grain the primary crystals. The size and angles of the impeller are shown in Figure 2-5. Torque τ was measured using a torque meter during stirring. The impeller was drawn up immediately after stirring, and the slurry was maintained at the set temperature for 200 s to enable sufficient foaming. Finally, the aluminum alloy foam was cooled down with water and solidified.
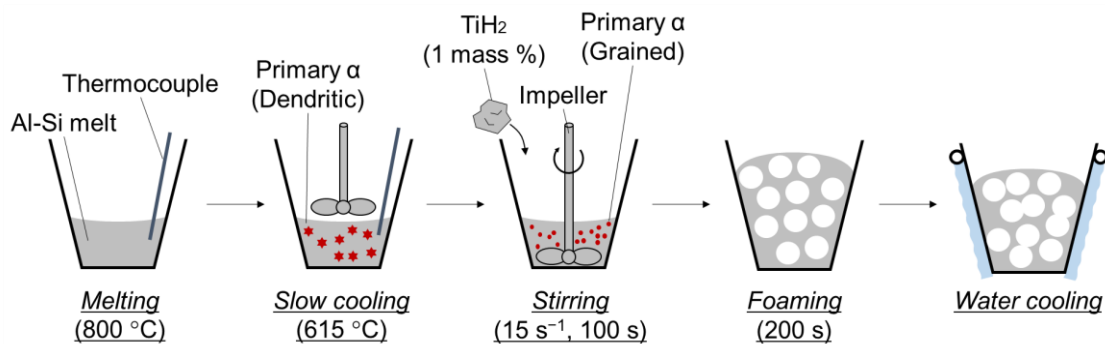
Figure 2-4 Schematic illustration of the foaming process via the semi-solid route.
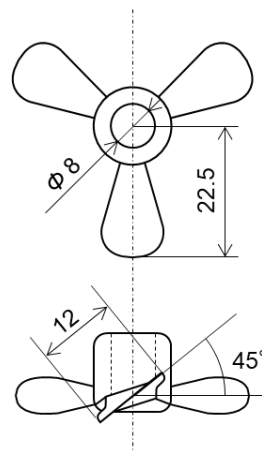
Figure 2-5 Size and angle of impeller for stirring the semi-solid slurry to fabricate the aluminum alloy foam.

2.2.4. Evaluation of pore structure

The densities of the aluminum alloy foam ρ_p [kg/m^3] were measured using Archimedes' principle as follows: The mass of the foam in air M_{air} [kg] was measured using a spring balance. The foam was sunk into the water completely, and the mass of the foam in the water M_{water} [kg] was measured using a spring balance. Finally, the density ρ_p was calculated from Equation 2-2.

$$\rho_p = \frac{M_{air}}{M_{air} - M_{water}} \times \rho_{H2O} \qquad (2-2)$$

In Equation 2-2, ρ_{H2O} [kg/m^3] represents the density of H$_2$O at room temperature, 1×10^3 kg/m^3. The porosity p and pore distribution were evaluated quantitatively. The porosity is the fraction of gas phase inside the entire foam. The porosity p of the aluminum alloy foam was evaluated using Equation 2-3 with the density of Al-6.4 mass% Si alloy ρ_{np} of 2.67×10^3 kg/m^3 [6].

$$p(\%) = \left(1 - \frac{\rho_p}{\rho_{np}}\right) \times 100 \qquad (2-3)$$

After measuring the porosity p, the aluminum alloy foam was cut in half through the center as indicated in Figure 2-6. The only half specimen was cut into six specimens. The cross section was observed using an optical microscope (VHX-5000, Keyence corporation, Japan) and divided into measurement windows that were 0.5 mm in height. Further, parts where the pore areas spread out of the specimen were eliminated from the measurement window. The sum of the areas of these parts was considered as the area of the metallic part A_m [mm^2] in a measurement window. To evaluate the pore structures, the binarized cross-sectional images of the measurement windows were constructed by setting an appropriate threshold to separate the pores from the other parts. In each measurement window, the area of each pore A_p [mm^2], area of the measurement window A_w [mm^2], area of primary crystal A_{pr} [μm^2], and each pore perimeter L_p [mm] were measured using the image analysis software WinROOF^{TM} 6.4.0 (Mitani Corp., Japan). In addition, the pore area ratio in each measurement window was calculated by dividing the sum of all pore areas (ΣA_p) by parameter A_w, as shown in Figure 2-3.
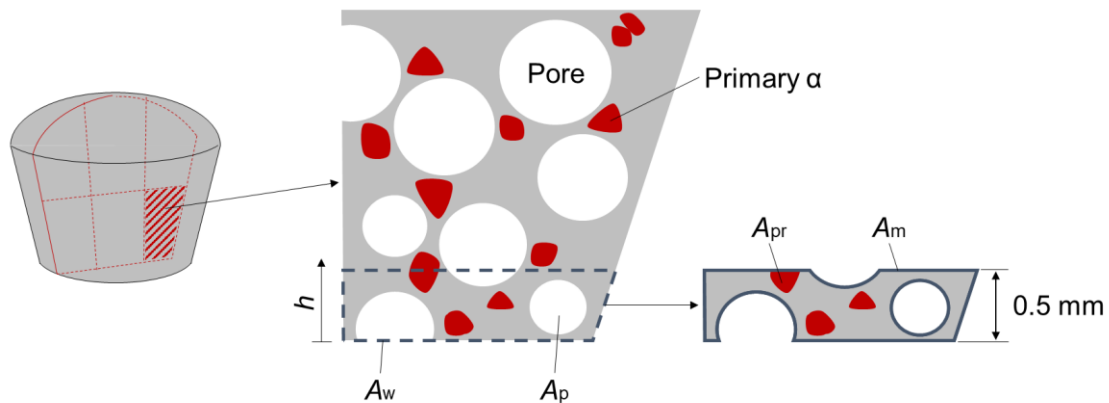
Figure 2-6 Calculated areas of pore A_p, primary crystals A_{pr}, and metal part A_m.

Each equivalent circle pore diameter d_p [mm] was calculated using Equation 2-3, and the average equivalent circle pore diameter $\overline{d_p}$ [mm] was calculated by dividing the sum of all values d_p by the total number of pores in the measurement window.

$$d_{\mathrm{p}} = 2\sqrt{\frac{A_{\mathrm{p}}}{\pi}} \qquad\qquad (2-3)$$

The average pore circularity $\bar{e}$ was calculated using Equation 2-4.

$$\bar{e} = \frac{1}{N_{\mathrm{p}}} \sum_{i=1}^{N_{\mathrm{p}}} \frac{4\pi A_{\mathrm{p}i}}{L_{\mathrm{p}i}^{2}} \qquad\qquad (2-4)$$

In Equation (2-4), N_{p} and i represent the total number of pores in the window and the serial number of a pore, respectively. The distributions of these pore parameters, $\Sigma A_{\mathrm{p}}/A$, $\overline{d_{\mathrm{p}}}$, and e, were plotted on graphs. Further, the cell walls were evaluated by Voronoi tessellation using the image analysis software ImageJ 1.53a (National Institutes of Health, Bethesda, US) to apply the percolation theory. In this analysis, each pore was replaced with a Voronoi polyhedron centering the center of the pore. Each Voronoi edge was recognized as the cell wall.

2.2.5. Microstructural observation

Each specimen from the six cut parts mounted in resin was ground using waterproof abrasive papers, a diamond suspension with a satin polishing cloth, and colloidal silica with a suitable polishing cloth using a polishing machine (MECATECH 334, Presi, Tokyo, Japan). The colloidal silica included an etching agent. The polished surface was observed with the optical microscope (VHX-5000, Keyence, Miyagi, Japan). In the microscopic images, the grained crystals, which are approximately 200 μm in size, were defined as primary crystals and filled with red color. The areas of each primary crystal A_{pr} and the metallic part A_{m} [mm^2] were measured with WinROOF$^{\mathrm{TM}}$ using the same process shown in the previous section. The area ratio of the primary crystals was calculated by dividing the sum of the area of the primary crystals ΣA_{pr} in the measurement window by the area of the master alloy A_{m}, as shown in Figure 2-3. Each equivalent circle diameter of the primary crystal d_{pr} [μm] was calculated using Equation (2-3), with the parameter A_{p} replaced by A_{pr}. Furthermore, the ratio of the area of the primary crystals to the area of each cell wall p_{cw} was calculated by dividing the area of the cell wall A_{cw} by the total area of the primary crystals ΣA_{pr}, as shown in Equation (2-5), where i represents the number of primary crystals. The area of the cell wall A_{cw} was defined as the metallic part with the same length as the Voronoi edge. The distributions of $\Sigma A_{\mathrm{pr}}/A_{\mathrm{m}}$ were plotted on a graph.

$$p_{\mathrm{cw}} = \frac{\Sigma A_{\mathrm{pr}i}}{A_{\mathrm{cw}}} \qquad\qquad (2-5)$$
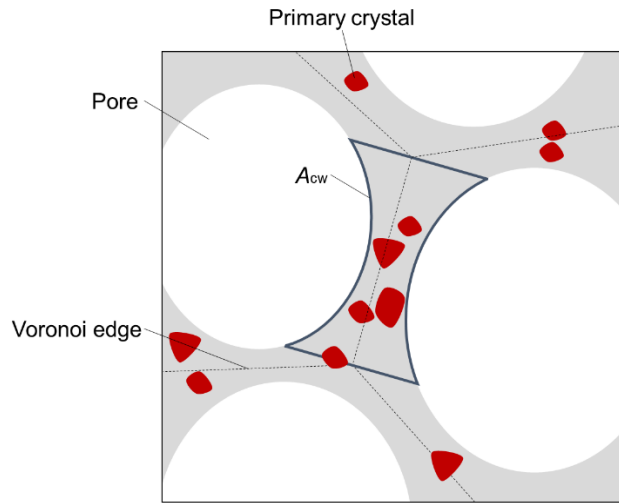
Figure 2-7 Schematic of the cell wall defined by Voronoi tessellation.

The cross-sections were etched using Weck's reagent via immersion for 48 s at room temperature [7,8]. Weck's reagent was prepared by mixing 4 g $KMnO_4$, 1 g $NaOH$, and 100 g distilled water. After etching, the microstructures on the cross-sections were observed using an optical microscope. Observing all solidifying segregations in their entirety is difficult, and therefore, only the sufficiently etched parts were observed. The parts in the semi-solid state before growing are referred to as the original parts. The original area of each primary crystal in the semi-solid state A_{pr}' was evaluated using WinROOF^{TM}. The original equivalent circle diameter of each primary crystal d_{pr}' was calculated using Equation (2-3) with A_p replaced by A_{pr}'. The grown radius of each primary crystal Δr [μm] was calculated using Equation (2-6).
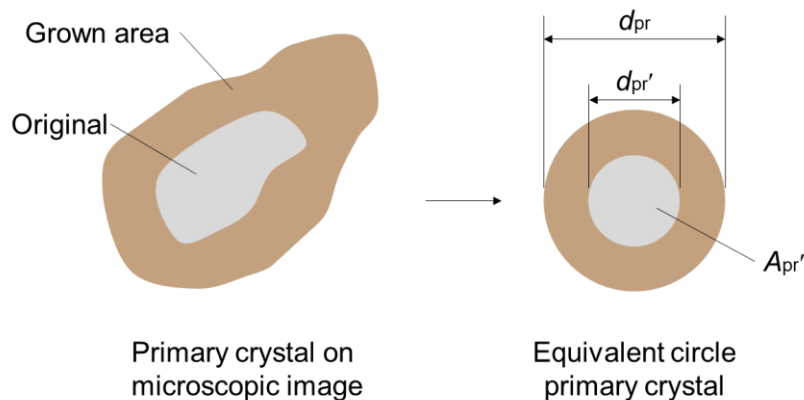
Figure 2-8 Measurement of the diameter of the original primary crystal and grown area of the primary crystal.

$$\Delta r = \frac{d_{pr} - d_{pr}'}{2} \qquad (2-6)$$

2.3. Results

2.3.1. Pore distributions

The porosity p of the fabricated aluminum alloy foam was calculated to be 30.2% with a measured ρ_{np} of 2.67×10^3 kg/m³. Figure 2-9 shows the cross-section of the aluminum alloy foam. Figure 2-10(a-c) show the distribution of the pore area ratio $\Sigma A_p/A_w$, average equivalent circle diameter of the pore $\overline{d_p}$, and average pore circularity $\bar{e}$ in the height direction for every 0.5 mm, respectively. The aluminum alloy foam was fabricated with a near-uniform pore structure through the semi-solid route.

5 mm

Figure 2-9 Cross section of fabricated aluminum alloy foam through the semi-solid route.
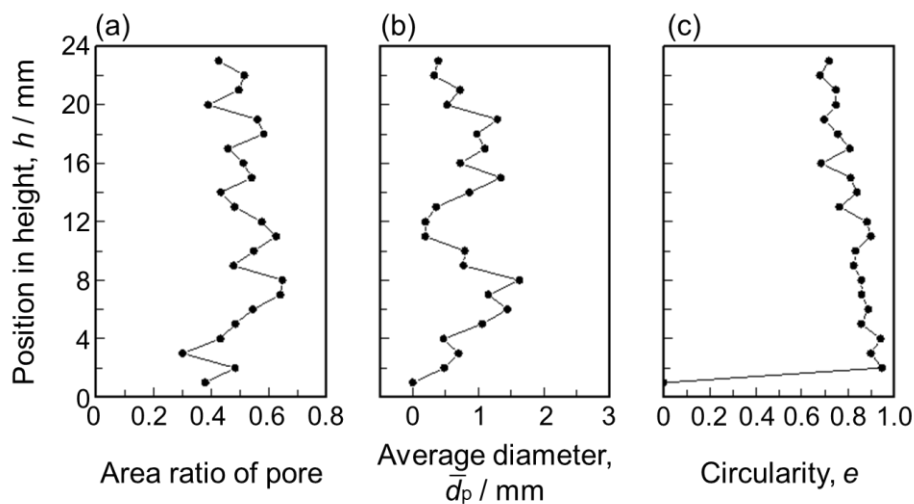
Figure 2-10 Distribution of pore morphologies in the height direction. (a) Area ratio of the pore to the area of measurement window $\Sigma A_p/A_w$. (b) Average equivalent circle diameter of pore $\overline{d_p}$. (c) Circularity of pore e.

60

2.3.2. Microscopic observation for the primary crystals

Figure 2-11(a) shows the microscopic image on the cross-section of the aluminum alloy foam. Some primary crystals were present inside not only the plateau border, which is the connection point of the cell walls, but also on the cell walls. Figure 2-12(a) and 2-12(b) show the microscopic images of the primary crystals before and after etching using Weck's reagent. Three types of crystal shapes were observed. One type was completely grained primary crystals, indicated in red in Figure 2-11(b, c). The second type was conjoined grained crystals, and the other was dendrite crystals. In Figure 2-12(b), the brown area surrounding the white area represents the grown area.
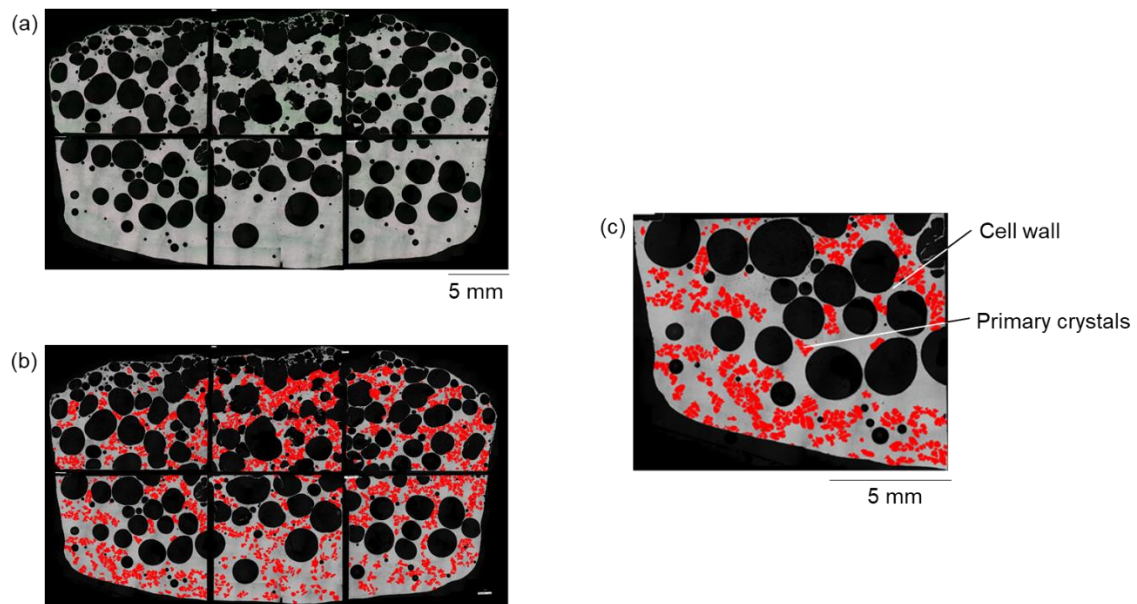
Figure 2-11 Microscopic images of the cross-section of the fabricated aluminum alloy foam. (a) Cross-section of the foam. (b) Primary crystals are shown in red. (c) Magnified image of the cross-section.
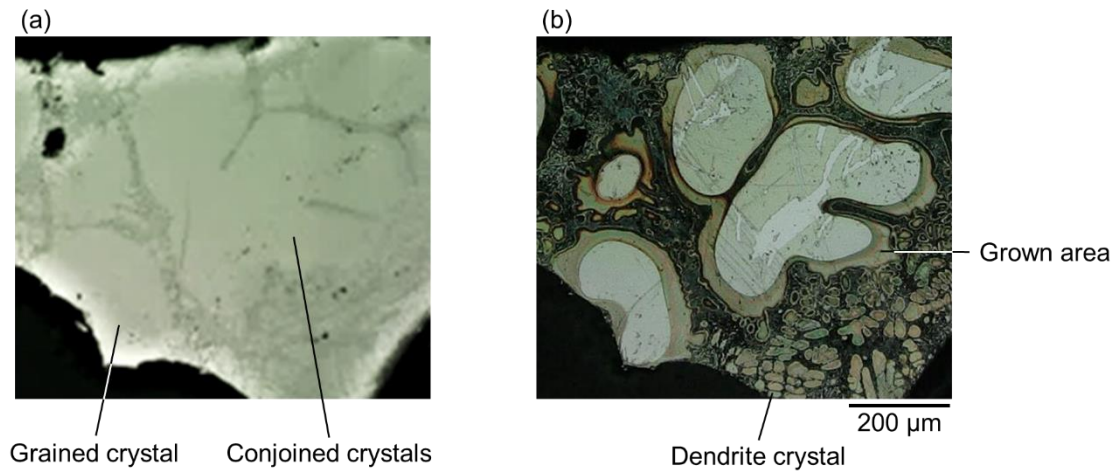
Figure 2-12 Magnified microscopic images of the primary crystals. (a) Before and (b) after etching with Weck' reagent.

Figure 2-13 shows the area ratio of the primary crystals in the height direction for every 0.5 mm. The average area fraction of the primary crystals was 27%. This value, including some primary crystals grown during the water cooling process, is two times higher than the set volume fraction of solid of 12% at 615 °C.
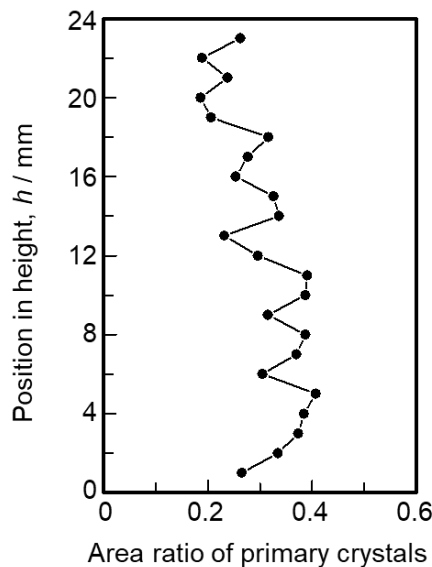
Figure 2-13 Distribution of the area ratio of the primary crystals to the area of the metallic part in the height direction.

Figure 2-14 shows the torque history during the stirring process. The value of torque τ decreases along with the time of stirring. Therefore, the equivalent circle diameters of the primary

crystals are considered to decrease because of stirring.
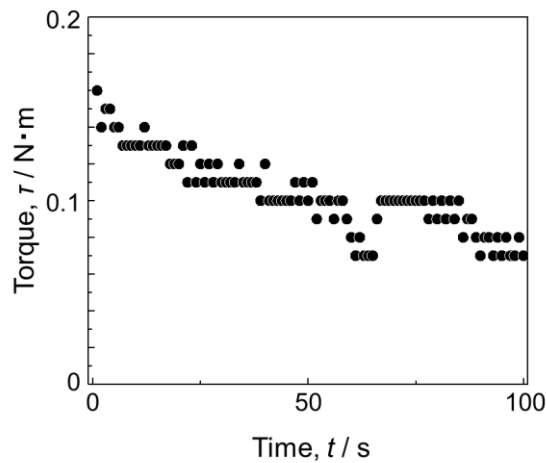
Figure 2-14 Torque history during the stirring process.

2.4. Discussion

2.4.1. Original size of the primary crystals in the semi-solid state

The dendritic primary crystals were crystalized after the slow cooling process during fabrication. The temperature of the semi-solid slurry was kept constant after the slow cooling process to keep the volume fraction of solid constant. Therefore, the observed primary crystals are the crystals that formed during the slow cooling process. Stirring the semi-solid slurry converted the primary crystals to grained crystals. However, some of the observed crystals had dendrites, and therefore, the primary crystals must have grown during the water-cooling process. This study focuses on the stabilization mechanism during the foaming process, and therefore, the original size of the primary crystals in the semi-solid state needs to be measured to discuss this mechanism quantitatively.

Figure 2-12(b) shows the microscopic image after etching by Weck's reagent. The brown area surrounding the white grain crystal can be considered as the segregated part in solidifying, which are determined to be the original primary crystals [8]. According to the phase diagram, the white grain crystals contain 99% of Al and 1% of Si. However, the brown part has more Si content because of the segregation. The molten metal solidified relatively rapidly, and therefore, diffusion could not keep up with the inner and outer solidification areas, thereby resulting in segregation. The structure that appeared as one crystal before etching had two crystals surrounded by the segregated part after etching. This clearly indicates the growth of primary crystals.

The original size of the primary crystals needs to be calculated to discuss the stabilization mechanism during the foaming process. The grown radius of each primary crystal Δr is plotted in Figure 2-15.
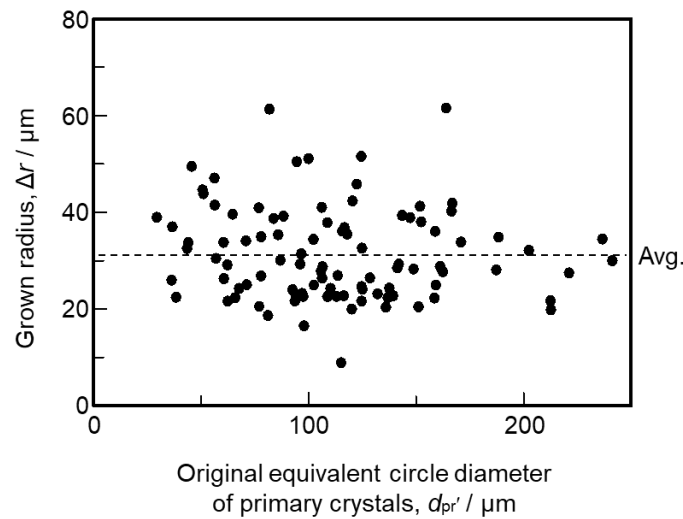
Figure 2-15 Grown radius of each primary crystal Δr.

The Δr values are approximately equal irrespective of the size of the primary crystals before growth, and therefore, the growth rate slows down with an increasing radius of the primary crystals. The average grown length $\overline{\Delta r}$ is calculated by dividing the sum of all values Δr by the number of primary crystals; this value is approximately 31 μm. The original diameter of all primary crystals on the cross-section d_{pr}' is calculated by subtracting 31 from each d_{pr}. Furthermore, the average of the original diameter $\overline{d_{pr}'}$ is calculated as 192 μm, which is still larger than the preferred range described in the Introduction. The original area of all primary crystals A_{pr}' is calculated using Equation (2-7). The original area fraction of the primary crystals is calculated as 17% by dividing $\Sigma A_{pr}'$ by the parameter A_m. This value approximately equals the set volume fraction of solid of 12%. The subsequent discussions will be based on the original size of the primary crystals in the semi-solid state, that is, the volume fraction of solid during the foaming process will be considered as 12%.

$$A_{pr}' = \pi \left(\frac{d_{pr}'}{2} \right)^2 \qquad (2-7)$$

2.4.2. Percolation theory on stabilization mechanism

The percolation theory explains the phenomenon of flow inhibition despite the absence of complete blockages with obstacles. In this theory, percolation probability is defined as the percentage of obstacles in a system. The flow of the system is inhibited by obstacles when the percolation probability exceeds the percolation threshold p'. The percolation threshold changes depending on the structure and dimensions of the system. Therefore, the required amount of obstacles required to inhibit the flow will also change.

We applied this theory to the stabilization mechanism of the aluminum alloy foam, which was considered as a lattice structure comprising cell walls as paths for the melt. The primary crystals

were considered as obstacles in each cell wall, and cell walls with a sufficient number of primary crystals that exceed the percolation threshold were considered to have been clogged, with inhibited flows. Further, these cell walls were considered as obstacles in the lattice structure. Finally, if the percolation probability exceeded the percolation threshold, the flow of the lattice structure was inhibited. This implies that the drainage of the aluminum alloy foam was prevented by the primary crystals. In addition, the stabilization mechanism in three-dimensional aluminum alloy foam is discussed in the last section.

i. Percolation theory for cell walls

First, the following discussion about percolation theory applied to cell walls is summarized in Figure 2-16. From a microscopic observation, the cell walls can be grouped into three categories: those crossed by the primary crystals, those with a narrow path through the primary crystals, and those without any primary crystals. The cell walls in the first category are clogged by crossed primary crystals according to the percolation theory. However, it remains unclear if the cell walls in the second and third categories are clogged by the primary crystals. Therefore, the percolation model for a flow is applied to the cell walls [9]. In this model, the percolation probability of the cell wall model is defined as the area ratio of the primary crystals in the cell wall to the area of the cell wall p_{cw}. The percolation threshold of this model, p_{cw}', is approximately 0.581. Kuwahara *et al.* reported that the critical volume fraction of solid f_{s_cr}, which is the area fraction of the primary crystals required for inhibiting drainage, is in the range of 20–45%, and the expression $p_{cw}' \approx \sqrt{f_{s\_cr}}$ is established. The values of p_{cw} at all cell walls are compared with p_{cw}', and cell walls with p_{cw} larger than p_{cw}' ($p_{cw} > p_{cw}'$) are recognized as the aggregated parts with primary crystals. Cell walls with p_{cw} smaller than p_{cw}' are recognized as the non-aggregated parts. According to the percolation theory, the aggregated parts are kept stable because of the inhabitation of drainage by the clogging effect of the primary crystals. These aggregated parts are defined as the clogged cell walls. The above discussion about percolation theory applied to cell walls is summarized in Figure 2-16.
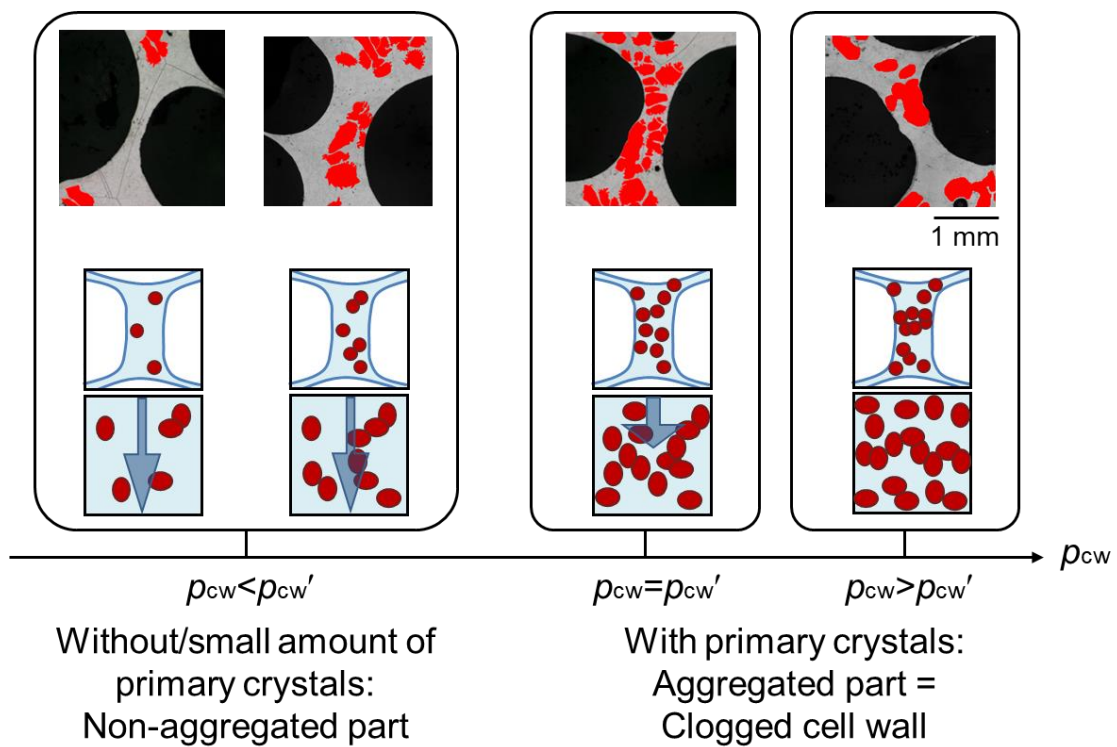
Figure 2-16 Applying percolation theory to the stability of the cell wall.

ii. Percolation theory for the structure of the foam

Figure 2-17 is a schematic depiction of the following discussion on percolation theory for the structure of the foam. In the previous section, it was revealed that the clogged cell walls were kept stable by the primary crystals; however, the non-aggregated parts also remained stable, even if they did not have a sufficient number of primary crystals. The percolation theory for a lattice structure was applied to the aluminum alloy foam to clarify this point. Figure 2-17 presents a schematic of the percolation theory applied to the structure of the entire foam.
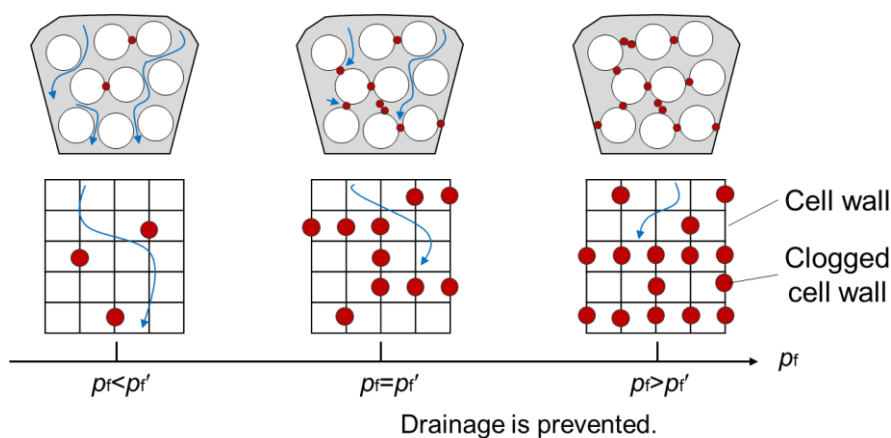
Figure 2-17 Applying percolation theory to the stability of the entire foam.

The aluminum alloy foam can be considered a simple lattice structure model comprising cell walls, wherein each side of the lattice structure acts as a path. According to the percolation theory for a lattice structure model, the flow through the entire structure is prevented when enough sides of the lattice are clogged with obstacles. Here, the primary crystals can be regarded as the obstacles, and the cell walls as the sides of the lattice. Therefore, the calculation of the percentage of the clogged cell wall reveals why non-aggregated parts are retained. The percolation probability for this lattice model, p_f, can be calculated using

$$p_f = \frac{n_{cc}}{N_{cw}} \qquad (2-8)$$

In Equation (2-8), N_{cw} and n_{cc} represent the number of all cell walls and the number of clogged cell walls, respectively. The percolation threshold p_f' for the simple lattice structure model is calculated using

$$p_f' = \frac{1}{n_s - 1} \qquad (2-9)$$

In Equation (2-9), n_s represents the number of sides exiting one vertex of the lattice. The cell walls correspond to the sides, the plateau border corresponds to the vertex, and z is 3; therefore, the p_f' is approximately 0.33 [4]. In this study, the value p_f was approximately estimated as 0.34, which is slightly larger than p_f'. In other words, non-aggregated parts remain stable because their drainage is inhibited by the existence of aggregated parts that exceed the percolation threshold. In summary, the aluminum alloy foam can be kept stable by the clogging effect of the primary crystals.

The points established thus far are shown in the graphs presented in Figure 2-18. Figure 2-18(a) shows the number of cell walls with each percolation probability p_{cw}. The dotted vertical line indicates the percolation threshold of the cell wall model p_{cw}'. Figure 2-18(b) shows the increasing cumulative percentage of cell walls with each value p_{cw}, wherein the dotted horizontal line indicates the percolation threshold of the lattice structure p_f'. The percentage of cell walls within the range of 0.581−1.0 in p_{cw} represent the percolation probability of the lattice structure p_f. Figure 2-18(b) indicates that the point p_f is located above the line of p_f'. Therefore, the aggregated parts help keep the aluminum alloy foam stable with the clogging effect at some cell walls.
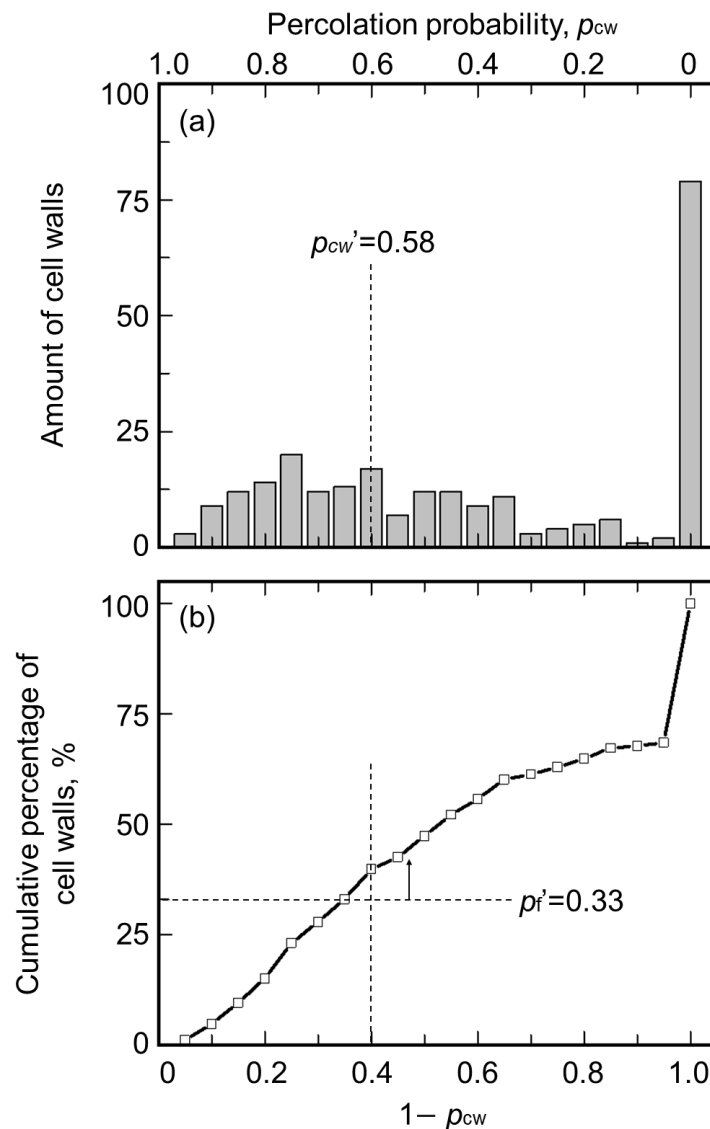
Figure 2-18 Graph of the relationship between the percolation probability and the cell wall.

iii. Discussion of percolation theory in three dimensions

Thus far, we have discussed the stabilization mechanism based on only two-dimensional information. However, a three-dimensional perspective is required because primary crystals and cell walls are in fact arranged in three dimensions. Further, the percolation threshold for the lattice model varies with the number of dimensions, and thus, a three-dimensional assessment and exact model for percolation theory are necessary. In this section, we examine whether the stabilization mechanism in the previous discussion is valid for three-dimensional models.

Based on the quantitative microscopic analyses, the spherical diameter of the crystals can be calculated easily from the diameter of the circle. Hensler suggested that the spherical diameter of the crystals S_{pr} can be calculated using the equation [10]

$$S_{\mathrm{pr}} = d_{\mathrm{pr}}{}' \left(\frac{4}{\pi}\right)^2 = 1.62 d_{\mathrm{pr}}{}' \qquad\qquad (2-10)$$

The S_{pr} values for all primary crystals were calculated. The cross-sectional area of the cell wall viewed in the flow direction $A_{\mathrm{cw}}{}''$ was calculated as follows: half of the length of the cell wall L_{cw} (same length as the Voronoi edge) was squared and multiplied by π. Further, the cross-sectional area of the primary crystal in the flow direction $A_{\mathrm{pr}}{}''$ was calculated using the same procedure. The p_{cw} values were recalculated by dividing $A_{\mathrm{pr}}{}''$ by $A_{\mathrm{cw}}{}''$. Cell walls with a p_{cw} value larger than $p_{\mathrm{cw}}{}'$ can be redefined as the aggregated parts.

The percolation probability for the foam p_{f} was recalculated as approximately 0.61. In the next step, p_{f} was compared with the percolation threshold. The structure of the aluminum alloy foam is also three-dimensional, and therefore, the percolation threshold for a three-dimensional model needs to be estimated. The lattice shape of the aluminum alloy foam is similar to a hexagonal column, and it is referred to as the honeycomb stack structure. Van der Marck clarified the percolation threshold for the honeycomb stack to be approximately 0.59 [11]. A comparison of p_{f} with this threshold showed that the stabilization mechanism using primary crystals is also valid in three-dimensional models.

Thus, primary crystals are considered one of the factors that can help stabilize the foam.

2.5. Conclusion

The stabilization mechanism of the aluminum alloy foam was discussed by observing the primary crystals considering the percolation theory. The results can be summarized as follows:

1. Some primary crystals were aggregated in the stable cell walls. In addition, the percolation probability exceeded the reference percolation threshold (0.581) in some stable cell walls (clogged cell walls). The clogged cell wall can retain its shape for a long time because of the presence of the primary crystals.

2. Cell walls with insufficient primary crystals also remained stable. Therefore, the fact that clogged cell walls inhibit the drainage of non-aggregated cell walls is considered as a factor that can help maintain the stability of the foam.

References in Chapter 2

[1] T. Miyoshi, M. Itoh, S. Akiyama, and A. Kitahara: ALPORAS Aluminum Foam: Production Process, Properties, and Applications. *Adv Eng Mater,* **2** (2000) *4*, doi: 10.1002/(sici)1527-2648(200004)2:4<179::aid-adem179>3.0.co;2-g.

[2] T. Hanafusa and K. Ohishi: Making of Porous Metallic Material by the Semi-solid Aluminum Alloy. *BULLETIN OF HIROSHIMA PREFECTURAL TECHNOLOGY RESEARCH INSTITUTE EASTERN REGION INDUSTRIAL RESEARCH CENTER,* (2010) *23*, 28-29, (written in Japanese).

[3] T. Kuwahara, A. Kaya, T. Osaka, S. Takamatsu, and S. Suzuki: Stabilization Mechanism of Semi-Solid Film Simulating the Cell Wall during Fabrication of Aluminum Foam. *Metals,* **10** (2020) *3*, 333, doi: 10.3390/met10030333.

[4] D. Stauffer, Aharony A. *Introduction to Percolation Theory / by Dietrich Stauffer and Ammon Aharony.* 2nd ed. (Taylor & Francis, an imprint of Taylor and Francis, Boca Raton, FL, 2014) .

[5] J.L. Murray and A.J. McAlister: The Al-Si (Aluminum-Silicon) System. *Bulletin of Alloy Phase Diagrams,* **5** (1984) *1*, 74-84, doi: 10.1007/BF02868729.

[6] S.P. Nikanorov, M.P. Volkov, V.N. Gurin, Y.A. Burenkov, L.I. Derkachenko, B.K. Kardashev, L.L. Regel, and W.R. Wilcox: Structural and Mechanical Properties of Al–Si Alloys obtained by Fast Cooling of a Levitated Melt. *Materials Science and Engineering: A,* **390** (2005) *1-2,* 63, doi: 10.1016/j.msea.2004.07.037.

[7] L. Gao, Y. Harada, and S. Kumai: Analysis of Microstructure Evolution and Precise Solid Fraction Evaluation of A356 Aluminum Alloy during Partial Re-Melting by a Color Etching Method. *J Mater Sci,* **47** (2012) *18*, 6553-6564, doi: 10.1007/s10853-012-6585-x.

[8] E. Weck, Leistner E. *Metallographic Instructions for Colour Etching by Immersion. II. Beraha Colour Etchants and their Different Variants.* (DVS GmbH, Düsseldorf, 1983) .

[9] L.N. Smith and C.J. Lobb: Percolation in Two-Dimensional Conductor-Insulator Networks with Controllable Anisotropy. *Physical Review. B, Condensed Matter,* **20** (1979) *9*, 3653-3658, doi: 10.1103/PhysRevB.20.3653.

[10] J.H. Hensler: The Relation between Grain Section and Grain Size. *J Inst Metals,* **96** (1968) *6,* 190-192.

[11] R. Kimmich, A. Klemm, and M. Weber: Flow, Diffusion, and Thermal Convection in Percolation Clusters: NMR Experiments and Numerical FEM/FVM Simulations. *Magnetic Resonance Imaging,* **19** (2001) *3,* 353-361, doi: 10.1016/S0730-725X(01)00248-X.

Chapter 3

Preferred volume fraction of solid for stable foams and

the effect of oxygen on the stability of foams

3. Preferred volume fraction of solid for stable foams and the effect of oxygen on the stability of foams

3.1. Introduction

Uniformity and reproducibility of the aluminum alloy foams are necessary to realize reliable industrial products. However, the drainage of the cell wall causes it to rupture, thereby making the pores ununiform and heterogeneous [1,2]. One of the effective approaches to keep the structure of the foams uniform and stable is preventing drainage. The semi-solid route uses primary crystals to prevent drainage. As discussed in Chapter 2, primary crystals can help prevent drainage not only in the cell walls but also in the entire foam by adopting the percolation theory on the clogging effect. The theoretical minimum area fraction of primary crystals in one cell wall required to prevent the drainage was obtained. However, the minimum volume fraction of solid required to prevent drainage has not been clarified. In addition, there is a need to identify the maximum volume fraction of solid. Comparative experiments need to be performed to determine the preferred range of the volume fraction of solid.

However, it can be difficult to perform comparative experiments for the semi-solid route because it is considerably sensitive to changes in temperature. This sensitivity can be attributed to the volume fraction of solid, which can change easily because of small changes in temperature. The temperature of the semi-solid slurry during the foaming process can significantly affect reproducibility, and therefore, accurate temperature control is necessary to maintain a constant temperature. However, the temperature of the melt slightly differs from the setting temperature in each experiment, and even under the same setting temperature with severe temperature control. If the temperature of the melt becomes considerably higher than the setting temperature, the pores become coarse because of drainage. Therefore, the allowance fluctuation of temperature from the setting temperature to fabricate foams with high reproducibility and the effect of the fluctuation in temperature on the pore morphology needs to be determined.

The atmosphere in the furnace can be changed when the comparative experiments become available by revealing the allowance fluctuation of the temperature. Previous research on the melt route revealed that not only the thickening agent but also the oxygen in the atmosphere improves the stability of the foam. The thickening particles are fixed on the oxide layer generated on the gas/liquid boundary (pore/cell wall boundary) of the pores because of the oxygen in the atmosphere. However, it remains unclear if the gas/liquid boundary of the pores in the foam fabricated through the semi-solid route comprise oxide particles. One approach that considers the gas/liquid boundary to be oxide or have an O_2-rich area follows the steps indicated in Figure 3-1. As shown in Figure 3-1, the surface of the melt is covered with oxides during the melting process, thereby generating a thick oxide layer. The rotating impeller can crush this oxide layer and grind it into oxide particles. The oxide particles are

distributed because of the stirring process. Finally, the oxide particles are fixed on gas/liquid boundary. In addition, O_2 gas is inherently contained in the base ingot, which ensures that the gas/liquid boundary has oxide particles.
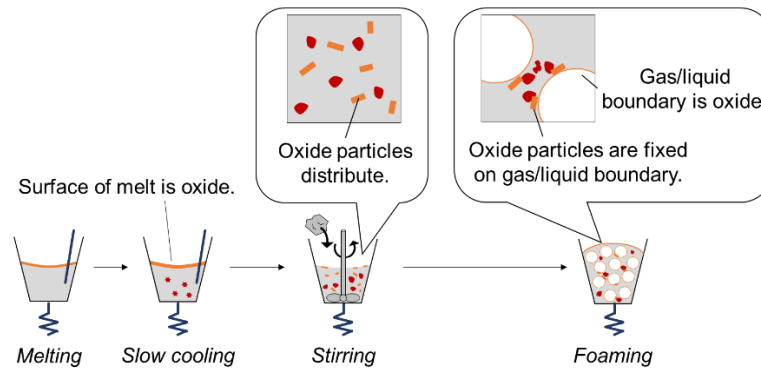
Figure 3-1 Schematic of the formation of oxide particles in the foams.

This chapter aims to assess the reproducibility of the foam, effect of increasing the volume fraction of solid on the clogging effect, and effect of oxygen on the stability of the foams. To achieve these objectives, aluminum alloy foams were fabricated via the semi-solid route under the same setting of fabrication conditions. Subsequently, the volume fraction of solid calculated from the actual temperature of the melt and pore morphologies were compared. Finally, the effect of changing the volume fraction of solid on the clogging effect was discussed by adopting the percolation theory. There is no precedent for the expected outcomes in this study, such as the reproducibility of the semi-solid route and the effect of the fluctuating volume fraction of solid on the pore morphology in the semi-solid route. Further, the semi-solid route has not been studied systematically with temperature control. This chapter is expected to offer new insights into the fabrication conditions of the semi-solid route.

3.2. Materials and methods

The fabrication apparatus used in this chapter is explained in 3.2.1. The fabrication processes of the aluminum alloy foam are discussed in 3.2.2. In this section, the chemical compositions of the used aluminum alloy and high purity air are also indicated. Five aluminum alloy foams are fabricated via the semi-solid route under the same setting conditions. After the fabrication, each foam is analyzed to measure the porosity, pore diameter, and circularity on the cross-section of the foam.

3.2.1. Fabrication apparatus

Figure 3-2(a) and 3-2(b) show the photograph and schematic of the electronic furnace used in this study, respectively. The furnace was installed in a vacuumed chamber to limit the effect of outside air on the alloy. The chamber was connected to a vacuum pump and gas cylinders of high purity air and Ar gas. The electronic furnace used in this chapter, which enables controlling the

atmosphere and concentration of oxygen in the chamber, is different from that used in Chapter 2. A Bourdon tube pressure gauge (AT1/4Rx60x-0.1MPa, Migishita Seiki Mfg. Co., Ltd., Hyogo, Japan) and a Pilani pressure gauge (M-350PG-SD, Canon Anelva Corp., Kanagawa, Japan) were set to measure the total pressure P_t in the furnace. A zirconia-type oxygen meter (OXITEC5000, ENOTEC GmbH, Nordrhein-Westfalen, Germany) was used to measure the concentration of oxygen C in the furnace.

The two type-K thermocouples TC-1 and TC-2 were set inside the furnace to measure the temperatures of the melt T_1 and the bottom of the crucible T_2, respectively. The edge of TC-2 was pressed against the center of the bottom of the crucible using the elastic force of the curved TC-2. Further, TC-2 worked as an indirect measurement device instead of TC-1, which cannot measure the accurate temperature of the alloy during the foaming process because it measures the temperature of the gas inside a pore. The heater was controlled by a PID controlling system which used T_2 as the feedback temperature.
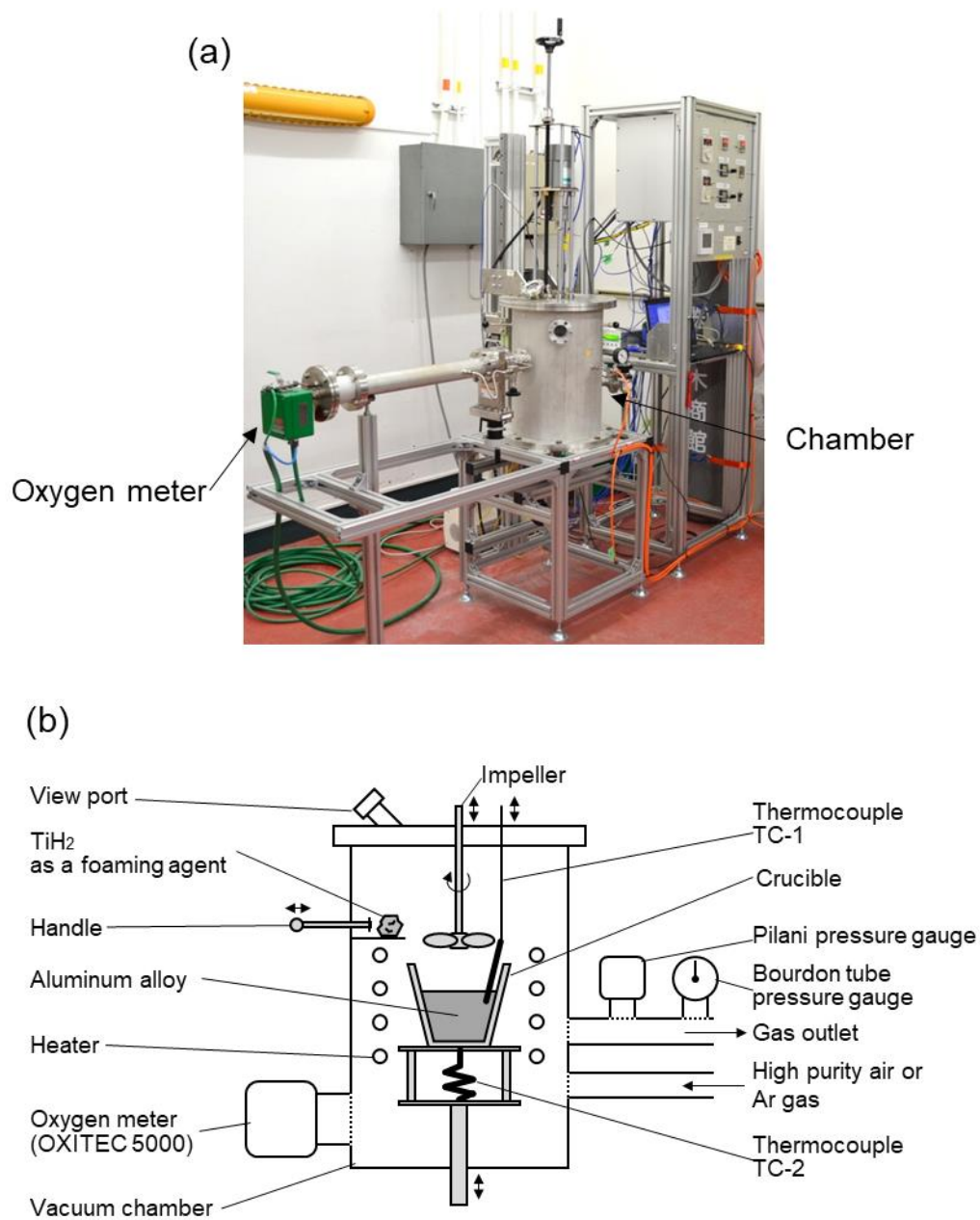
**Figure 3-2 Electronic furnace used in this study. (a) Exterior image of the furnace. (b)
Schematic of the electronic furnace.**

3.2.2. Fabrication of the aluminum alloy foam via the semi-solid route

Figure 3-3 shows a schematic of the fabrication processes of the Al-6.4 mass% Si alloy foam
via the semi-solid route. Five aluminum alloy foams were fabricated via the semi-solid route under
the same setting conditions. The processes employed for the semi-solid route in this study are as
follows: Al-6.4 mass% Si alloy was used as a base alloy for the fabrication to ensure that the volume
fraction of solid was 15% at 613 °C [3]. 100 g of the Al-6.4 mass% Si alloy supplied by UACJ
Corporation was weighed and set into a stainless crucible coated with Aron Ceramic.

Table 3-1 shows the chemical composition of the Al-6.4 mass% Si alloy described in the mill sheet provided by the supplier. During the entire fabrication process, TC-1 and TC-2 measured the temperatures at the same time.
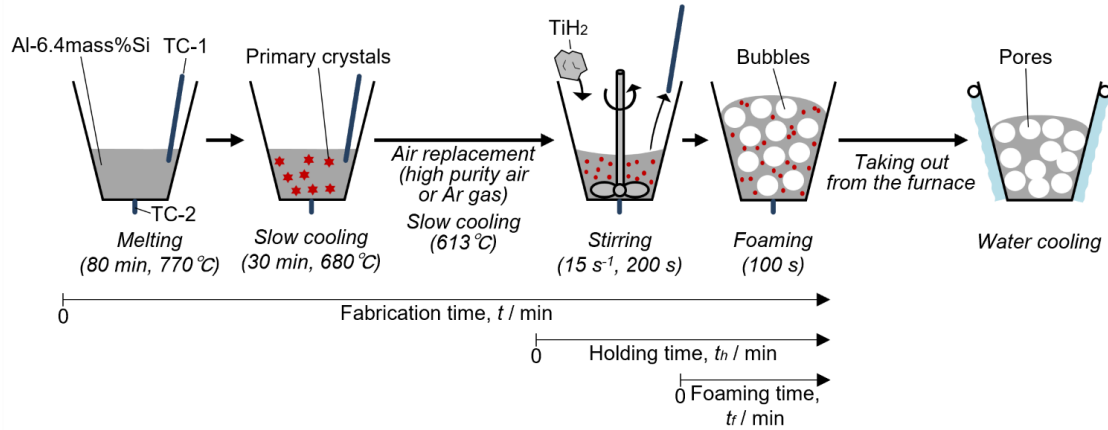
Figure 3-3 Fabrication process of the aluminum alloy foam via the semi-solid route.

Table 3-1 Chemical composition of the Al-6.4 mass% Si alloy.

Element	Si	Fe	Cu	Al
Mass%	6.4	0.0	0.0	Bal.

The Al-6.4 mass% Si alloy was heated in the vacuumed furnace for around 80 min until T_2 reached 770 °C. The fabrication time t started when the heater was turned on. The aluminum alloy was completely melted by this process. Next, the molten alloy was cooled slowly for 30 min until T_2 reached around 680 °C. Subsequently, high-purity air with 20% oxygen was inserted into the furnace to replace the remaining air in the furnace. The high-purity air was provided from a commercial gas cylinder purchased from Suzuki Shokan Co., Ltd. Table 3-2 shows the gas composition of the high-purity air as described in the mill sheet provided by the supplier. The high-purity air includes little H_2O, and therefore, no pores will be made from water vapor. The process of replacing the air, vacuuming, and inserting high-purity air was repeated three times to avoid the effect of outside air. The gas was inserted until the pressure reached 0.1 MPa.

Table 3-2 Chemical composition of commercial high-purity air.

Component	O_2	CO	CO_2	H_2O	N_2
vol ppm	20×10^4	< 0.1	< 0.1	< 0.54	Bal.

The molten alloy was slowly cooled to crystalize the primary crystals until T_1 reached the setting temperature (613 °C). At this temperature, the volume fraction of solid of the semi-solid slurry f_s was 15%, as calculated by the thermodynamics calculation software Thermo-calc 2020a (Thermo-Calc Software, Stockholm, Sweden). After T_1 became constant at the set temperature, TC-1 was pulled out. Hereafter, T_1 during foaming could not be measured directly, and therefore, the calibrated alloy temperature T_1' was calculated using the calibration equation. The calibration equation was generated by calculating the coefficients α and β, which satisfied Equation (3-1), using T_1 and T_2 measured in the entire fabrication process.

$$T_1' \, (°C) = \alpha T_2 \, (°C) + \beta \qquad (3-1)$$

The impeller was lowered to be slightly above the surface of the semi-solid slurry to preheat the impeller. Two packs of 1 g TiH_2 wrapped in a 10×10 mm^2 aluminum foil were added into the semi-solid slurry as a blowing agent immediately after the removal of TC-1. TiH_2 was placed in the electronic furnace in advance, as shown in Figure 3-3. The impeller stirred the semi-solid slurry at a rotational speed of 15 s^{-1} for 100 s. After stirring, the impeller was pulled out. T_2 was controlled to be constant in the range of $\pm$ 0.5 °C from the temperature immediately before the addition of TiH_2 for 5 min. Then, the slurry was held for 200 s for the foaming. After foaming, the heater was turned off. The heating time ended at the same time. The foamed slurry was removed from the furnace and solidified via water cooling immediately. This experiment was repeated five times under the same setting fabrication conditions.

After the five fabrications under the high purity gas atmosphere, the allowance range of the temperature to obtain the high reproducibility was revealed, as explained in Section 3.4.2. Based on that fabrication process, two foams were fabricated with the same fabrication conditions but under different atmospheres, i.e., high purity air and Ar gas. The Ar gas was provided from a commercial gas cylinder purchased from Suzuki Shokan Co., Ltd.

3.2.3. Measuring the porosities of the fabricated foams

The densities of the seven fabricated foams ρ_p were measured using Archimedes' principle as follows: The mass of the foam in air M_{air} was measured using a spring balance. Then, the foam was sunk into the water completely, and the mass of the foam in the water M_{water} was measured using a spring balance. Finally, the density ρ_p was calculated using

$$\rho_p = \frac{M_{air}}{M_{air} - M_{water}} \times \rho_{H2O} \qquad (3-2)$$

In Equation (3-2), ρ_{H2O} represents the density of H_2O at room temperature, i.e., 1×10^3 kg/m^3. Each porosity p was calculated from Equation (3-3) using the density of the Al-6.4 mass% Si alloy ρ_{np} of 2.67×10^3 kg/m^3 [4].

$$p(\%) = \left(1 - \frac{\rho_p}{\rho_{np}}\right) \times 100 \qquad (3-3)$$

3.2.4. Microscopic observation of the fabricated foams under the same setting fabrication conditions using an optimal microscope

The five foams fabricated under the same fabrication conditions were cut on a plane through the center. The cross-sections of the foams were observed using an optical microscope, and the equivalent pore diameter of the cross-sectional pore d_{pr} and pore circularity e were measured from the cross-sectional image using the image analysis software ImageJ 1.53c (National Institutes of Health, MD, USA). Further, the distributions of d_{pr} and e were obtained. Subsequently, the half specimens were cut into six pieces, and each specimen was filled in an epoxy resin. The cross-section was polished using waterproof abrasive papers and abrasive agents. Further, the cross-section was etched with Weck's reagent to visualize solute segregation in a primary crystal of the Al-Si alloy [5]. Weck's reagent was prepared by mixing 4 g KMnO$_4$, 1 g NaOH, and 100 g distilled water [6]. After etching, the microstructure of each foam on the cross-section before and after etching was observed from the microscopic images to recognize the primary crystals.

The microscopic observation of the fabricated foams was performed under different concentrations of oxygen using scanning electron microscopy (SEM), electron probe micro analysis (EPMA), and Auger electron spectroscopy. The two foams fabricated under different concentrations of oxygen were cut on a plane through the center. The cross-section images of the foams were photographed.

As shown in Figure 3-4, parts near the top surface and gas/metal boundary (cell wall) of the foam fabricated under high purity air were cut. Each surface that can be oxidized was coated with a resin including Ag (TK PASTE CR-2800, Osaka, Japan, KAKEN TECH Co., Ltd.) to protect the oxide layer. The specimens were coated with the resin and polished. After polishing, the polished surfaces were observed using SEM (JEM-1400Flash, Tokyo, Japan, JEOL Ltd.), EPMA (JXA-8230, Tokyo, Japan, JEOL Ltd.), and Auger analysis (JAMP-9500F, Tokyo, Japan, JEOL Ltd.) to evaluate the

concentration of oxygen quantitatively.
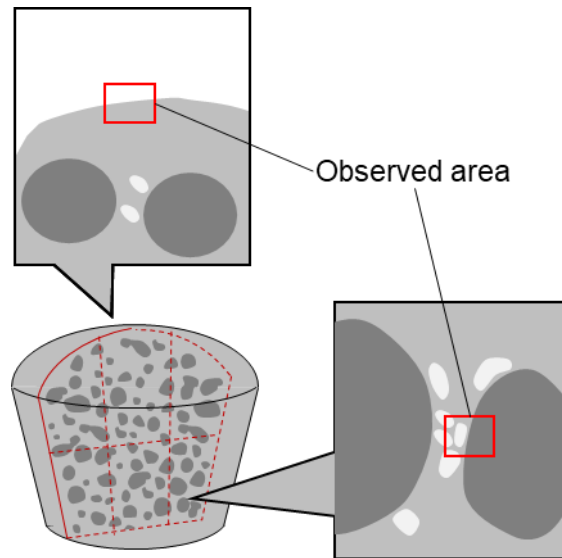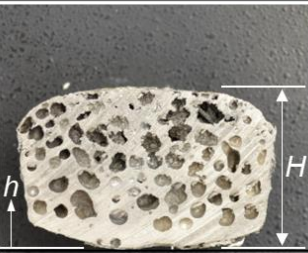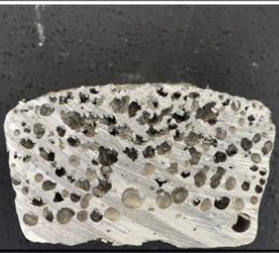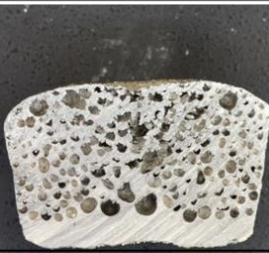
**Figure 3-4 Schematic of the observed area using SEM, EPMA, and Auger electron
spectroscopy.**

3.3. Results

3.3.1. Fabricated aluminum alloy foams

Figure 3-5 shows the cross-sectional images of the aluminum alloy foams fabricated at the same setting temperature. Porosities p are indicated under the corresponding foam. Foams A, B, and C have uniform and stable pores because they have small diameters and high circularity. The stability and size of the pores were evaluated for the following parts. Foam D has flattened pores, which seem to have collapsed after foaming. Foam E has connected pores; further, there are large pores, especially in the lower part of foam E.
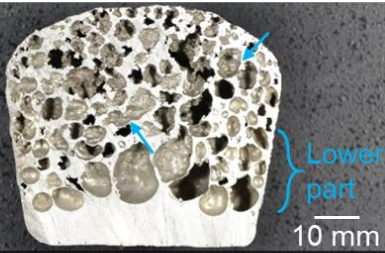
**Figure 3-5 Cross-section images of the fabricated aluminum alloy foams A, B, C, D, and E. Red
arrow indicates the flattened pores, and the light blue arrows indicate the connected pores.**

Porosity p varies considerably for foams A, B, C, and D. The relative standard deviation of
porosity σ_p of foams A, B, C, and D was calculated as 4% using Equation (3-4), where the parameter
p_i represents the individual porosity of the foams A, B, C, D, and E. Parameter $\bar{p}$ represents the average
porosity of the fine foams.

$$\sigma_p(\%) = \frac{\sqrt{\dfrac{\sum_{i=1}^{5}(p_i - \bar{p})^2}{n_f - 1}}}{\bar{p}} \times 100 \qquad (3-4)$$

The relative standard deviation of all foams was calculated as 23%, which is six times larger
than the value calculated except that for foam E. The large pores with low circularity of the foam E
enabled it to have a larger porosity compared to that of the others.

Figure 3-6 shows the distribution of the pore morphologies of each fabricated foam in the
height direction. The top position of the colored area on each graph shows the maximum height H (as
indicated in Figure 3-5) of each foam. As shown in Figure 3-6, the distributions of the circularity e of
foams A, B, and C are biased towards 1.0. In addition, foams A, B, and C have small pores inside, as
indicated by the distribution of equivalent circle diameter of pore d_{pr}. Thus, the pores in foams A, B,
and C are recognized as stable pores.

The distributions of pore circularity e of foams D and E spread across the wide area

compared to those of foams A, B, and C. These distributions represent the actual coarse pores of foams D and E. The flattened pores in foam D and the connected pores in foam E lower the circularity e. The average pore diameters of foams D and E are around 8.1 mm and 15.5 mm, respectively, whereas those of foams A, B, and C are around 3.4 mm, 2.6 mm, and 2.5 mm, respectively. The average pore diameters of foams A, B, and C are close to those reported in previous chapter. The plot of foam E placed around 60 mm in diameter is the largest pore located in the lower part of the foam, as shown in Figure 3-6. This pore broadens the distribution of the pore diameter d_{pr}. Therefore, the pores in foams D and E are not stable. Pores that have low circularity and a large diameter are recognized to be in the poor state, whereas pores with a small diameter and high circularity are considered to be stable pores.
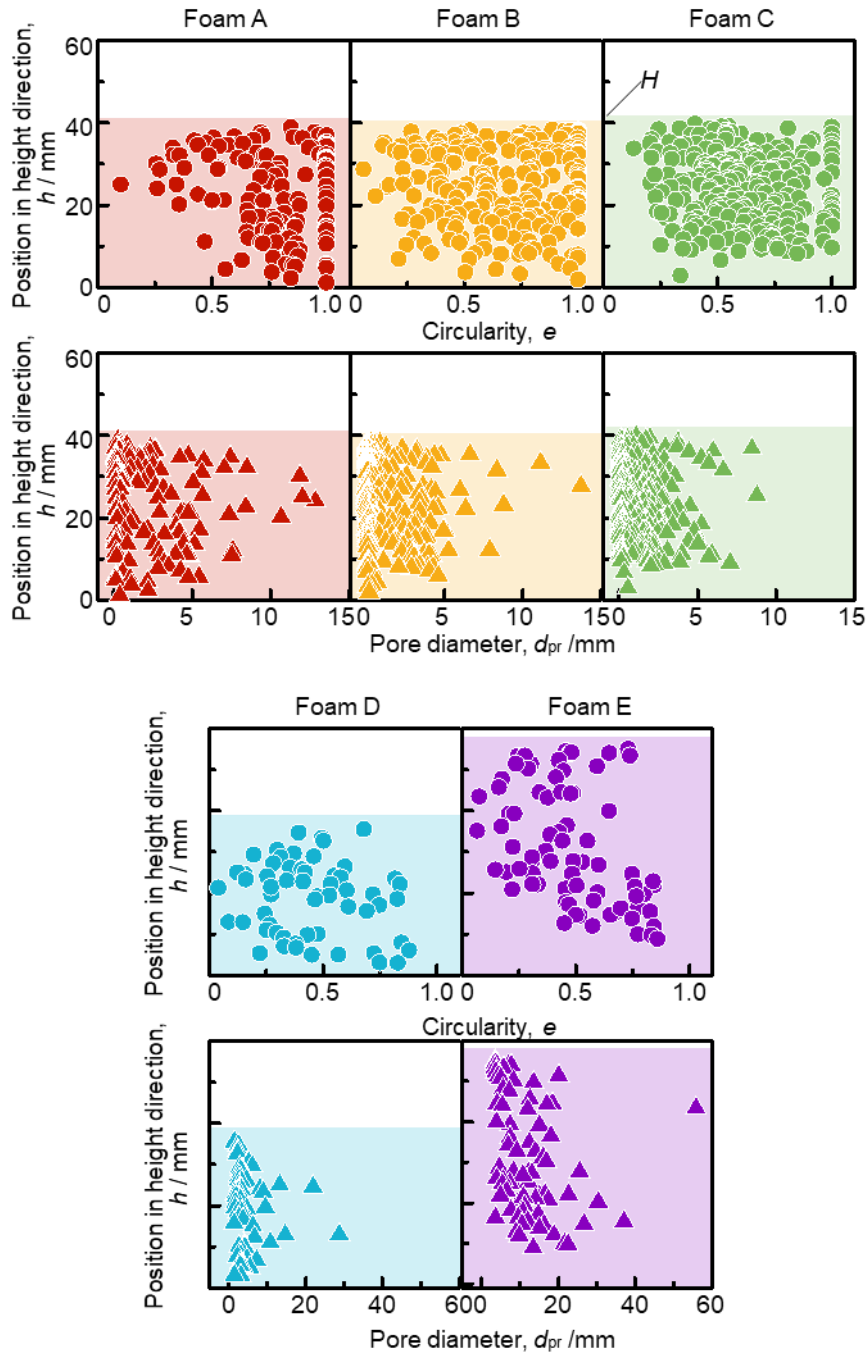
**Figure 3-6 Distributions of the pore circularity and pore diameter of foams in the height
direction for foams A, B, C, D, and E.**

3.3.2. Temperature and pressure history during fabrication

Figure 3-7 shows the temperature history of the fabrication process conducted in this chapter.
Figure 3-7(a) shows temperature history for the entire fabrication process and Figure 3-7(b) shows
that for the foaming process (around 170–270 min). Each color indicates each foam already shown in
Figures 3-5 and 3-6. The solid lines indicate the temperature of the melt T_1 and the dashed lines indicate

the temperature of the bottom of the crucible T_2. The thick lines indicate the calibrated temperature of the melt T_1', as shown in Figure 3-7(b). The arrows vertical to the horizontal axis indicate the removal of the impeller and the start of the foaming process.
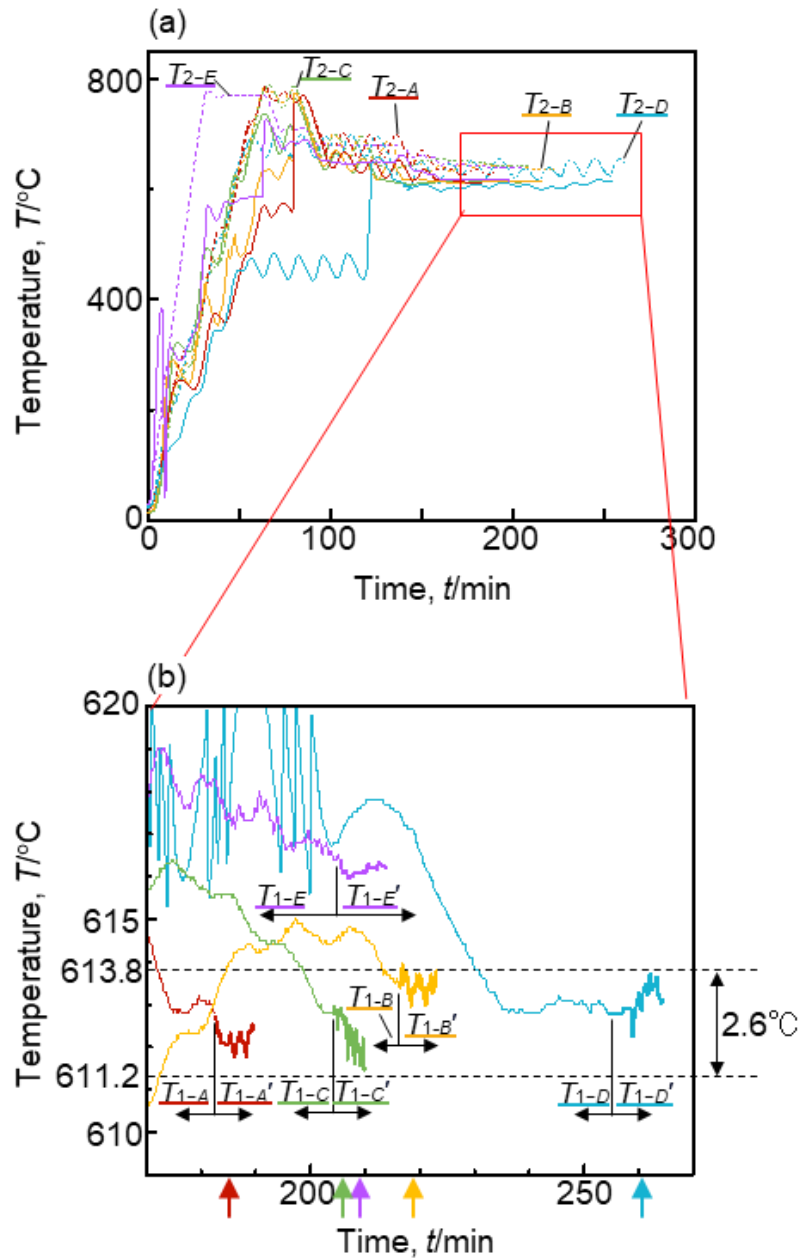
Figure 3-7 Temperature history of each foam during fabrication. Dashed lines indicate the temperature of the bottom of the crucible and solid lines indicate the temperature of the melt. (a) Temperature history during the entire heating time. (b) Close-up temperature history around the foaming process.

The calibration temperature T_1' was calculated using Equation (3-5) obtained by substituting

coefficients α and β into Equation (3-1).

$$T_1{'}\ (°C) = 0.96T_2(°C) + 7.8 \qquad\qquad (3-5)$$

The coefficients in Equation (3-1) were determined to coincide with the history of T_1 5 min just before foaming. Figure 3-8 shows the relationship between the temperature of the melt $T_{1\text{-}A}$ and the calibrated temperature $T_{1\text{-}A}{'}$ during the fabrication of foam A. The determination coefficient R^2 was calculated as 0.974. As indicated by the determination coefficient, the calibration equation was well-matched for predicting the temperature of the melt during foaming.
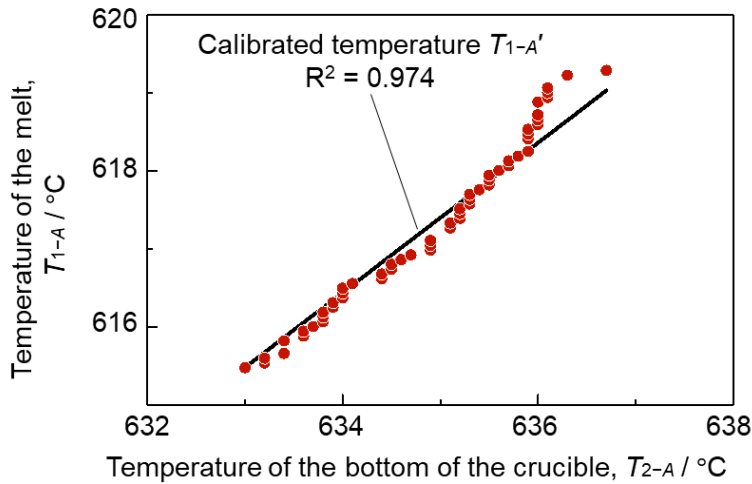
**Figure 3-8 Relationship between the temperature of the melt and the bottom of the crucible.
Black line obtained by the liner fitting indicates the calibrated temperature.**

Each temperature history had a different heating time, which is the period from when the heater is turned to when it is turned off. The results indicated that temperature oscillation lengthens the time for controlling the temperature constant. As indicated in the right-side graph, each foaming temperature differed slightly. Foam E had the highest temperature of the melt during foaming. Further, foam D had the longest heating time and temperature oscillation. Foams A, B, and C showed considerably similar temperature histories throughout the entire fabrication process.

3.3.3. Pressure history during fabrication

Figure 3-9(a) shows the total pressure P_t measured by the Pilani pressure gauge and O_2 partial pressure P_{O2} calculated by multiplying P_t with the concentration of oxygen C (Figure 3-10). Figure 3-9(b) shows the close-up graph of the O_2 partial pressure P_{O2}. Each vertical dashed line indicates the start of the holding time of each foam. Figure 3-9(c) shows the O_2 partial pressure P_{O2} during the foaming process on the axis of the holding time, which starts after the addition of TiH_2, and ends when the foaming process ends. Each color corresponds to the fabricated foam, as in the previous figures. The results indicate that the highest and lowest partial pressures when the foaming process

ended were for foams D and B, respectively. The difference between the highest and lowest pressures was 0.012 MPa. The difference between the highest and lowest total pressures when the foaming process ended was 0.035 MPa.
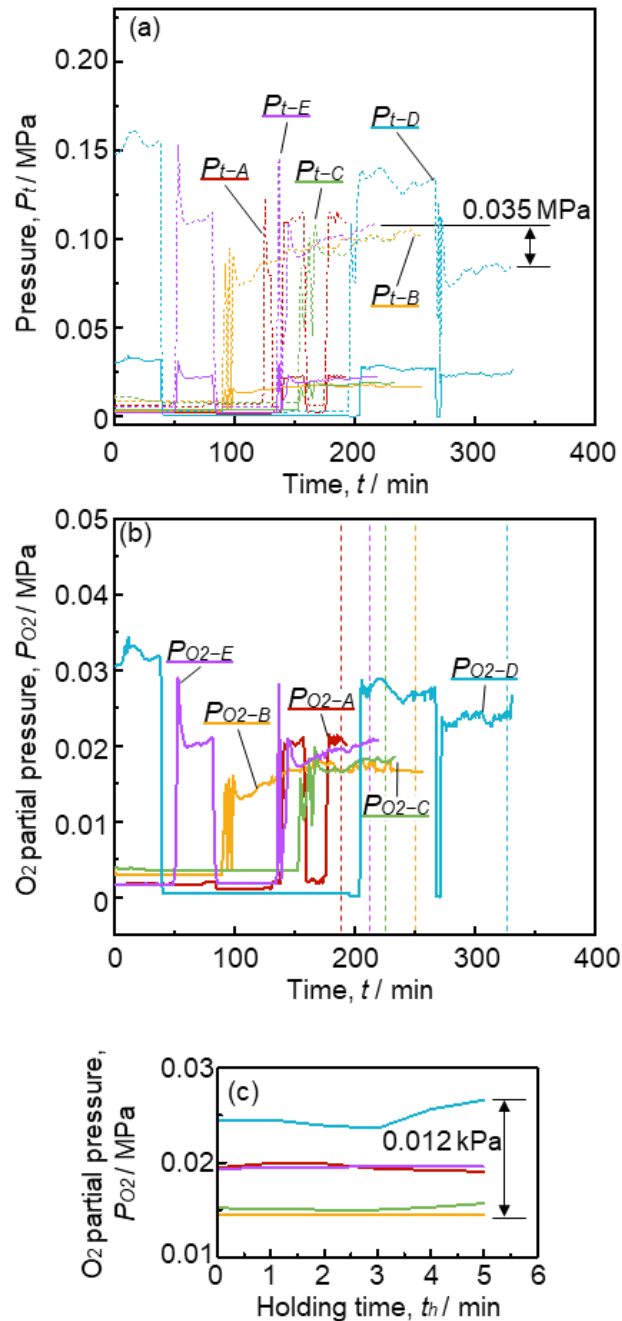
Figure 3-9 History of pressure during the fabrication of each foam. (a) Total pressure and O_2 partial pressure. (b) Close-up history of partial pressure of oxygen. (c) Close-up history of partial pressure of oxygen at start of the holding process.
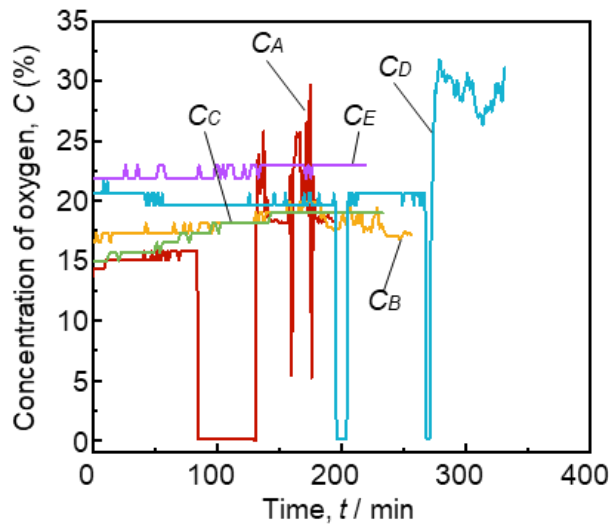
Figure 3-10 History of the concentration of oxygen during the entire heating time.

3.4. Discussion

3.4.1. Effect of H_2 generated through the decomposition of TiH_2 during the foaming process

The difference between the highest and lowest O_2 partial pressure P_{O2} when the foaming process ended was 12 kPa. Further, the relative standard deviation of the concentration of oxygen C of each foam when the foaming process ended was as small as 8%.

According to Figure 3-9, the total pressure P_t during the foaming process of each fabrication increased by around 0.1 kPa. In this process, TiH_2 added into the semi-solid slurry as the blowing agent was thermally decomposed and generated H_2 gas. If 2 g of the added TiH_2 decomposed thermally, the generated H_2 gas was calculated to be around 8.9×10^{-4} m^3. The volume of the furnace is around 0.19 m^3, and therefore, the pressure raised during foaming can be calculated as 0.5 kPa using Boyle–Charle's law. However, some TiH_2 remains undecomposed in the foam [7]. Therefore, the amount of the generated H_2 gas would have been considerably smaller. The results indicate that the increment in the total pressure P_t can be attributed to the generated H_2 gas. The concentration of oxygen C was not affected by the generated H_2 gas. The O_2 partial pressure P_{O2} changed during foaming because it was affected by changes in total pressure P_t. In fact, the concentration of oxygen C changed slightly. Therefore, the generated H_2 gas remains in the foam as pores.

3.4.2. Reproducibility among multiple experimental runs via the semi-solid route

As shown in Figure 3-6, there are differences in the temperature histories between the fabricated foams even though the fabrication processes and conditions were controlled. An allowance range of fabrication conditions to obtain high reproductivity through the semi-solid route must be determined to discuss the effect of the increase in the volume fraction of solid on the clogging effect.

Foams A, B and C are compared to confirm the allowance of the fabrication conditions because their temperature histories are remarkably similar to each other, especially in the cooling and foaming processes. The relative standard deviation of porosity σ_p was calculated as 5%. Further, the relative standard deviation of the average circularity σ_c and that of the average equivalent pore diameter σ_d were calculated to be as small as 11 and 5%, respectively. Thus, foams A, B and C were fabricated under high reproductivity fabrication process. The calibrated temperature T_1' of foams B and C, when the foaming process ended, were 613.8 and 611.2 °C, respectively. The difference between the two temperatures is 2.6 °C, as shown in Figure 3-7. According to the phase diagram calculated by Thermo-Calc, there was a change of 5% in the volume fraction of solid among foams A, B, and C. Therefore, the fabrication processes via the semi-solid route conducted in this study show high reproductivity when the change in the volume fraction of solid is under 5%.

3.4.3. Characteristics of temperature and the microstructure of the foam with poor morphology

Foams C and D must be compared because their temperatures of the melt during foaming was almost the same around 613 °C; however, foam D takes a long time to control the temperature constant. Further, the pores in foam D are in the poor state, whereas the pores in foam C are stable, as indicated in Section 3.1. Figure 3-11(a) shows the temperature histories of foams C and D. Figure 3-11(b) indicates the close-up temperature history around 150 min to 250 min. Figure 3-11(b) clearly indicates that the temperature history of foam D changed at frequent intervals with a large temperature gradient. The temperature oscillation lengthens the entire heating time, and therefore, the longer entire heating time caused by the temperature oscillation can lower pore morphologies.
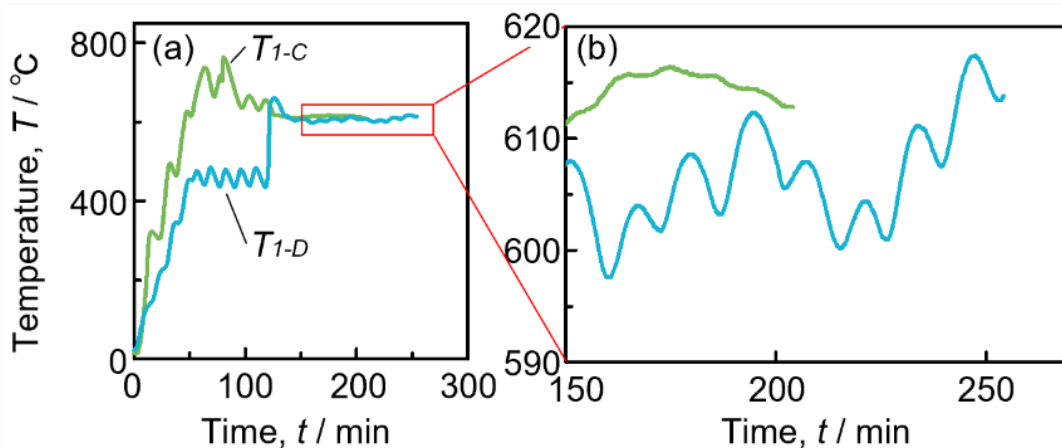
Figure 3-11 Temperature history of foams C and D. (a) History of TC-1. (b) Close-up temperature history around the foaming process.

Figure 3-12 shows microscopic images of the cross section of foams C and D. The upper

row shows the microstructure polished without etching, and the lower row shows the microstructure after etching with Weck's reagent. The microscopic images obtained after etching indicate that foam C has a granular primary crystal α, indicated by a white area surrounded by a brown circle and a white arrow (a). The white part indicates the original primary crystals that existed during the foaming process. The brown circle around the white part represents solute segregation. Further, eutectic crystals are observed in foam C, indicated by the white arrow (b). Foam D has both a dendritic and granular primary crystals α. Most dendritic parts are colored brown, as indicated by the white arrow (c). The eutectic crystals were observed in foam D, and these crystals grew during foaming. The average size of grained primary crystal α besides the brown circle in foams C and D were calculated as 102 μm and 131 μm, respectively. The average size of the dendritic primary crystals α in foam D was calculated as 180 μm. The average circularities $\bar{e}$ of foams C and D were calculated as 0.60 and 0.49, respectively. Therefore, the dendritic primary α also lowers pore circularity.
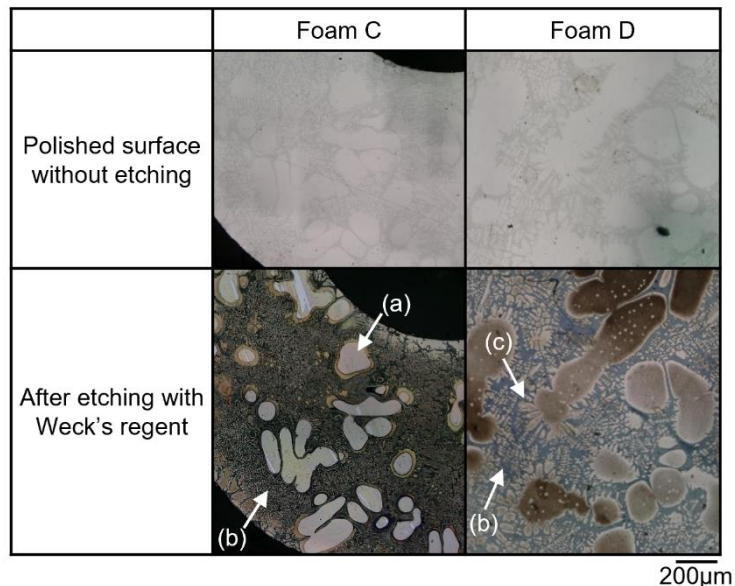
Figure 3-12 Microscopic images of primary crystals in foams C and D. Upper and bottom images indicate the microscopic images before and after etching by Weck's reagent. (a) White part is the grained primary α crystalized during the slow cooling process. (b) Darker part represents the eutectic crystals. (c) Dendritic white part surrounding the brown part represents the dendritic primary crystal α, crystalized during the holding or water-cooling process. (d) The gray part represents the eutectic crystals.

3.4.4. Effect of TiH$_2$ on the reproducibility

The TiH$_2$ absorbs the heat when it is thermally decomposed. Therefore, the temperature of the melt was considered to be lowered locally around the packs of the TiH$_2$. According to the previou research, the endothermic energy of the TiH$_2$ is around 31.1 kcal./mol [8]. If the 2 g of the TiH$_2$ generate

the hydrogen gas inside the 100 g of molten aluminum silicon alloy (AC4C), there will be temperature reduction of around 53 °C. However, the TiH_2 was pre-heated before addition in the furnace, therefore, the temperature reduction was smaller than the expectation. However, the decrease in temperature causes a decrease in the volume fraction of solid, which may have reduced the reproducibility.

3.4.5. Relationship between the clogged cell wall and volume fraction of solid

The maximum difference in the calibrated temperature T_1' between foams C and E was calculated as 4.5 °C. According to the calculation of the Thermo-Calc, the difference in the volume fraction of solid was 9.8%. Two effects are possible when the volume fraction of solid increases: one is that the number of clogged cell walls will increase; the other is that the fraction of primary crystals in already clogged cell walls will increase, and thus, the number of clogged cell walls will not increase. In the former case, the foam structure can be recognized as more stable because the drainage of each cell wall is prevented. Based on these hypotheses, the effect of an increment of 9.8% in the volume fraction of solid on the clogging effect will be revealed in this section.

Figure 3-13 shows microscopic images for a closer look at one cell wall inside foams E, B, and C. The primary crystals are colored red to improve the visibility of the microstructure. Each average size of primary crystals in foams B, C, and E was calculated as 112, 109, and 110 μm, respectively.
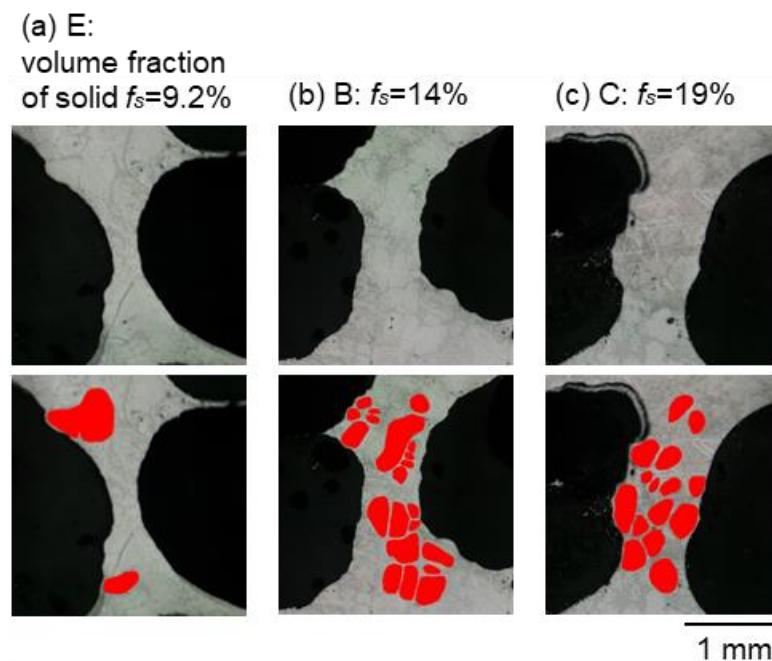
Figure 3-13 Images in the top row are microscopic images of one cell wall inside foams (a) E, (b) B, and (c) C. Primary crystals are colored red in the bottom images.

Figure 3-14 shows the graph that indicates the area ratio of primary crystals in one cell wall to the area of one cell wall A_{pr}/A_{cw} in foams B, C, and E. Each plot indicates one cell wall. The plots are located in the red area when the area ratio of primary crystals in the cell wall A_{pr}/A_{cw} exceeds the percolation threshold, 0.58 in this case [9]. In these cases, the cell walls are recognized as clogged cell walls, and the drainage in the clogged cell walls is prevented by primary crystals. According to Figure 3-13(a), which shows the cell wall of foam E, the cell wall did not have a sufficient number of primary crystals to prevent the drainage. The area ratio A_{pr}/A_{cw} of this cell wall was calculated as 0.21. The area ratio A_{pr}/A_{cw} of foams B and C, shown in Figures 3-13(b) and (c), was calculated as 0.63 and 0.60, respectively. Therefore, Figures 3-13 (b) and (c) show clogged cell walls with prevented drainage. Based on the percolation theory, the foam can be recognized as stable foam when the percentage of clogged cell walls exceeds the percolation threshold of 0.33 [10]. This time, the percentage of the clogged cell walls to all cell walls in foam E was calculated as 0.12, which is smaller than the threshold. Therefore, foam E was not the stable foam according to both the distributions of the pore morphologies and the percolation theory.

The distributions of foams B and C in Figure 3-14 show that the distribution of A_{pr}/A_{cw} located in the red area is not significantly different. The percentages of clogged cell walls to all cell walls of foams B and C were calculated as 0.34 and 0.45, respectively. Both values exceeded the percolation threshold for the planar lattice structure of 0.33, and therefore, foams B and C were recognized as stable foams.
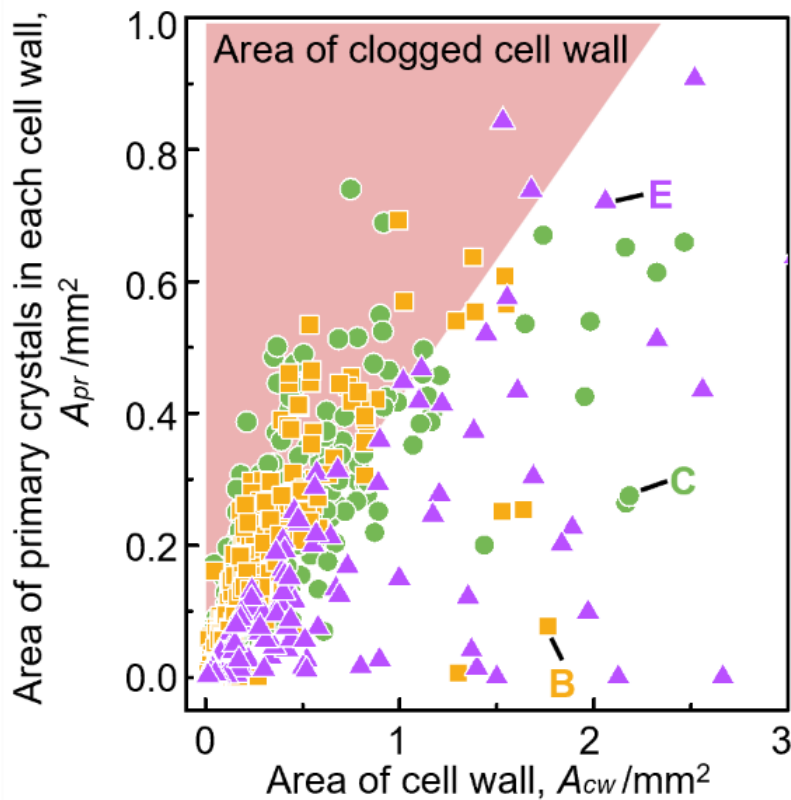
**Figure 3-14 Relationship between the area of primary crystals and area of cell walls in foams
B, C, and E.**

Figure 3-15 shows the relationship between the ratio of the clogged cell wall to all cell walls
r_c and the volume fraction of solid f_s for foams B, C, and E. The plots on the area above the red dashed
line, which is the percolation threshold of 0.33, indicate a stable foam. The fitting curve was obtained
as Equation (3-6) by linear approximation. The coefficient of determination R^2 was calculated as 0.959
by subtracting 1 from this value. When the coefficient of determination R^2 increases, the residual error
of fitting also increases. Therefore, a value of R^2 close to 1 indicates a good fit.

$$r_c = 0.033f_s - 0.16 \qquad (3-6)$$

According to Figure 3-15, the ratio of clogged cell walls to all cell walls increases with an
increase in the volume fraction of solid. Therefore, the results proved the hypothesis mentioned in
Section 4.3 that foams with a higher volume fraction of solid are more stable because the drainage in
more cell walls is prevented. Further, the preferred range of the volume fraction of solid can be
determined from Figure 3-15. According to the intersecting point of percolation threshold 0.33 and the
fitting curve, the minimum limitation of the volume fraction of solid can be determined to be
around15%. The foam will be unstable under 15% in the volume fraction of solid. Further, there will
be no clogged cell walls under 5% in the volume fraction of solid. The ratio of the clogged cell walls
r_c will not change over around 35% in the volume fraction of solid, according to the intersecting point

of the fitting curve and black dashed line. Therefore, the green area in Figure 3-15 can be recognized as the preferred range to fabricate the foam stabilized by the clogging effect. Finally, the mechanism of pore stabilization by primary crystals when the volume fraction of solid increases.
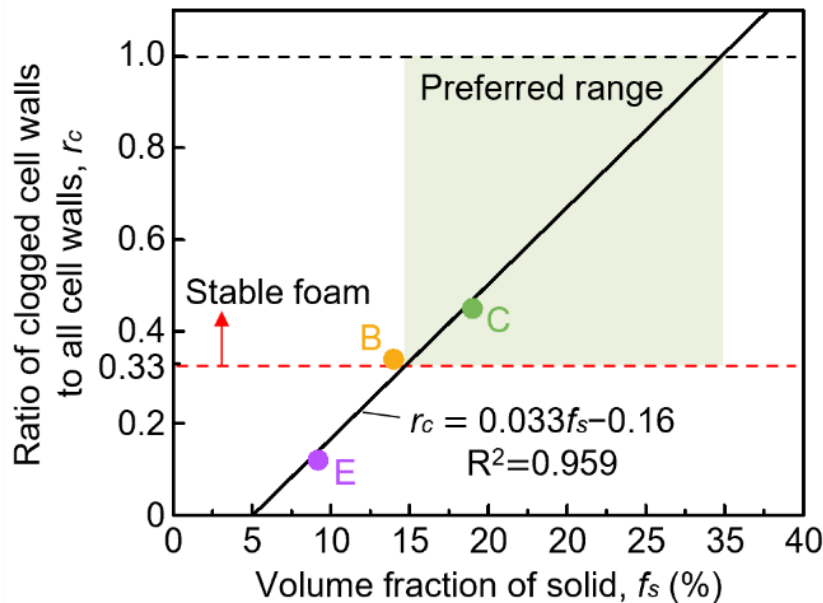
Figure 3-15 Relationship between the ratio of the clogged cell walls to all cell walls and volume fraction of solid. Plots show foams B, C, and E. Black line indicates the fitting curve. The green area indicates the preferred range where stable foams can be fabricated with the proper range of the volume fraction of solid.

Figure 3-16 shows the schematic describing the stabilization of foams in each foaming stage during the foaming time arranged by each volume fraction of solid. The foaming time indicates the entire foaming process which starts after the removal of the impeller and ends when the foaming process ends, as shown in Figure 3-4. Figures 3-16 (a-c), (d-f), and (g-i) show how pores become stable when the volume fraction of solid is high but lower than 35%, slightly exceeds 15%, and is lower than 15%, respectively. The green area indicates the preferred range of the volume fraction of solid. Each fabricated foam A, B, C, and E is indicated at its corresponding part for the volume fraction of solid. Foam D is excepted from Figure 3-16 because foam D had the temperature oscillation during the heating.

In the early stages of foaming, the pores are still small. The primary crystals are spread broadly in cell walls regardless of the volume fraction of solid, as shown in Figures 3-16(a), (d), and (g). In the middle stage of foaming, H_2 gas bubbles are generated and grow through the decomposition of the blowing agent, making the cell walls thinner. If the volume fraction of solid is not sufficient to prevent the drainage, as shown in Figure 3-16(h), the pores will go upwards as the drainage advances,

and therefore, the liquid phase stands in the lower part. Few clogged cell walls are generated because the primary crystals do not gather in the cell walls. The primary crystals begin to clog the cell walls if the volume fraction of solid is in the preferred range, as shown in Figures 3-16(b) and (e). The drainage in the clogged cell walls will be prevented based on the clogging effect. An important point is that the ratio of the primary crystals in each clogged cell wall will become almost the same as each other. Further, the ratio of the primary crystals in clogged cell walls will not change even if the volume fraction of solid increases above 15%. Schematic (x) in Figure 3-16 describes the two examples of the clogged cell walls in the case of a higher volume fraction of solids compared to that of Figure 3-16(e). The fraction of the primary crystals in the two cell walls in the schematic (x) is the same as each other. Moreover, the fraction of the primary crystals indicated in the schematic (x) seems to be the same as the clogged cell wall indicated in Figure 3-16(e). These schemes indicate that primary crystals tend to gather and prevent the drainage in more cell walls. Therefore, the primary crystals will not gather in already clogged cell walls as described in the schematic (x') in Figure 3-16.

The cell walls become thinner in the late stage of foaming. As shown in Figures 3-13(c) and (f), clogged cell walls remain stable because of the clogging effect with a sufficient fraction of the primary crystals. However, cell walls will be ruptured as shown in Figure 3-16(i) if the volume fraction of solid is lower than the preferred range. Finally, pores in the poor state will be generated in this case, and therefore, it can be concluded that the clogging effect works more effectively when the volume fraction of solid exceeds the 15% value defined by the percolation theory.
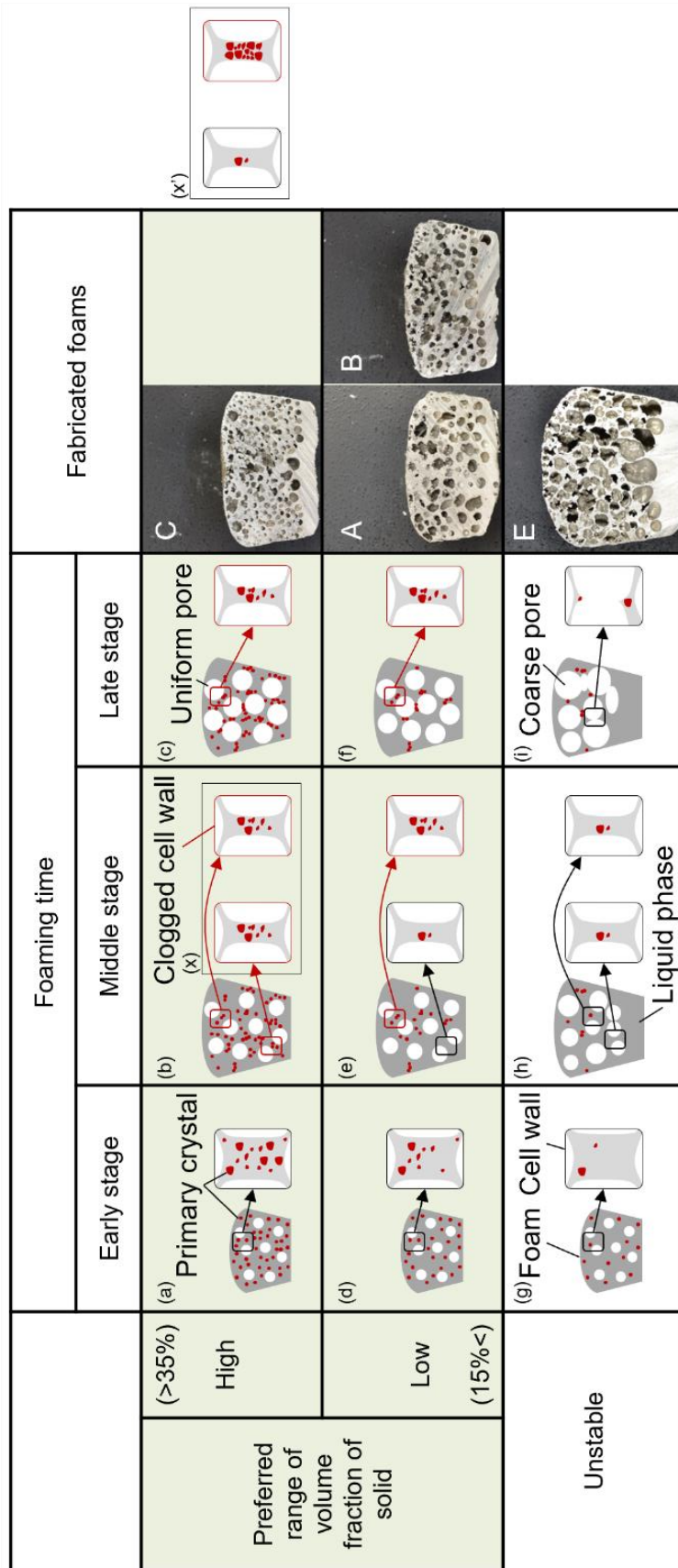
Figure 3-16 Stabilization mechanism at each stage of foaming. (a-c) Higher fraction of the solid smaller than 35%. (x) Actual cell walls with enough fraction of the primary crystals to prevent the drainage. The fraction of the primary crystals does not change significantly among the cell walls. (x') Cell walls with or without a sufficient fraction of primary crystals to prevent the drainage. The fraction of the primary crystals changes among the cell walls. Those conditions do not occur in actual aluminum foams fabricated through the semi-solid route. (d-f) Lower fraction of the solid larger than 15%. (g-i) Unstable stage with a lower fraction of the solid smaller than the 15%.

3.4.6. Oxidation of the aluminum alloy near the liquid/gas boundary

Figure 3-17 shows the pressure history of foams fabricated under the atmosphere with different concentrations of oxygen. According to Figure 3-17, the concentration of oxygen at the end of the foaming process for the foam fabricated in high-purity air and Ar gas was calculated as 18% and 10 ppm, respectively.
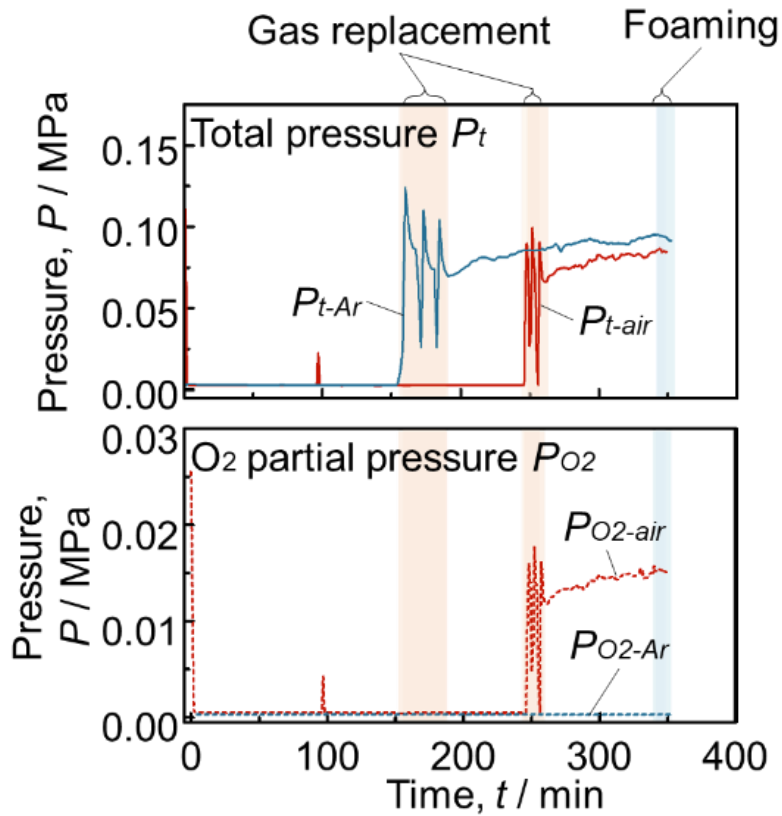
Figure 3-17 Pressure history of foams fabricated under different concentrations of oxygen. (a) History of total pressure P_t. (b) History of O_2 partial pressure P_{O2}.

Figure 3-18 shows the cross section of each fabricated foam. The values of porosity p were also indicated under the images. The foam fabricated in 18% oxygen has a higher porosity as 61.5% compared to that in the 10-ppm oxygen, for which the porosity is 51.0%. Therefore, the oxygen in the atmosphere during fabrication may improve the porosity and keep the pores stable.

Concentration of O_2 $C=61.5\%$ $C=61.5\%$
Porosity $p=61.5\%$ $p=51.0\%$

10 mm
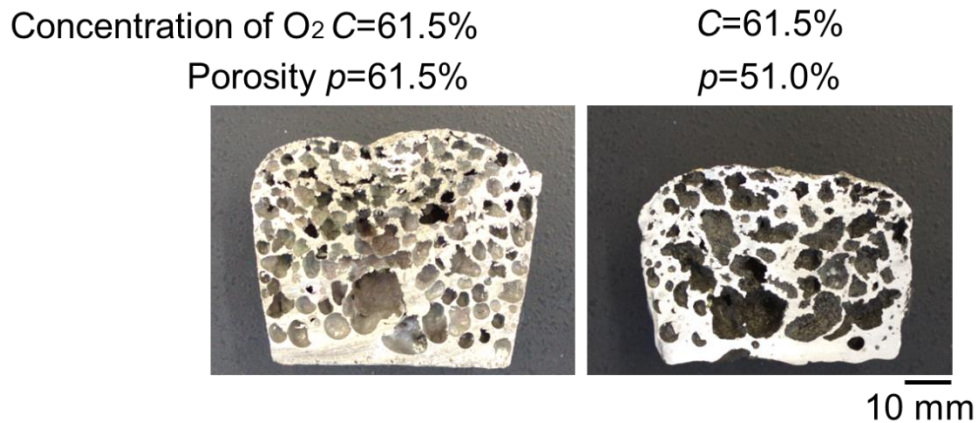
Figure 3-18 Cross-sections of foams fabricated under 18% O_2 (a) and 10 ppm O_2 (b). The values of porosity are indicated under the images.

Figure 3-19 (a) shows the SEM image indicating the pore/metal boundary of the foam fabricated under 18% oxygen. Auger analysis results indicate that there is an area where 200-μm-thick layer with oxide particles insides. The primary crystals can be observed in the oxide area in Figure 3-19(b). In addition, the oxide particles may be Al_2O_3, according to the EPMA analysis. Since the amount of oxides observed in this study are very small, there is no risk of strength reduction. Therefore, oxygen in the atmosphere can generate oxidation on the boundary and fix the primary crystals near the boundary.
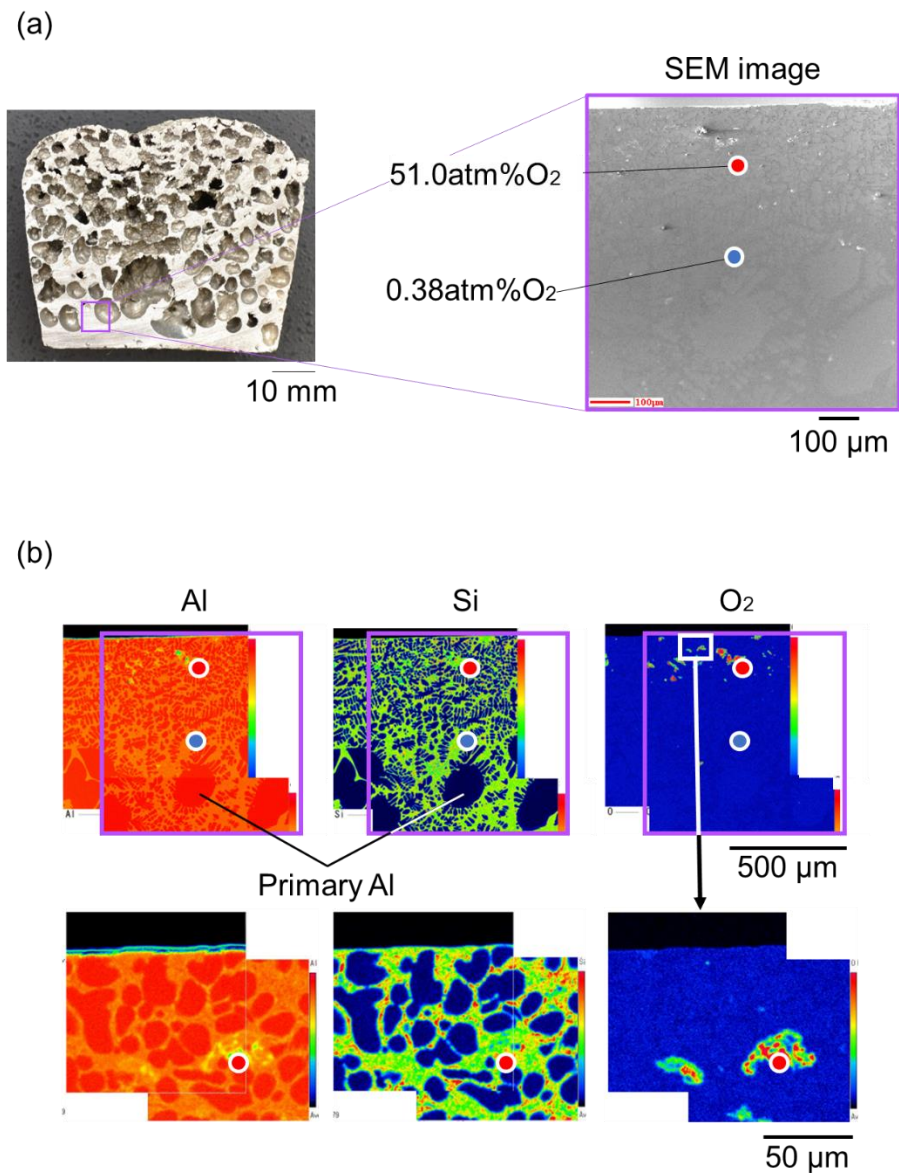
Figure 3-19 Microscopic images around the gas/liquid boundary of the pores in the foam fabricated under 18% O₂. (a) SEM image around the gas/liquid boundary. Quantitative values of O₂ measured by the Auger analysis. (b) EPMA images around the gas/liquid boundary on the same field of view as the SEM image.

3.5. Conclusion

Aluminum alloy foams were fabricated via the semi-solid route using a hypoeutectic aluminum silicon alloy. The fabrication process and effect of the volume fraction of solid on the clogging effect were discussed. The results are summarized as follows:

The fabrication process through the semi-solid route conducted in this chapter ensured the reproductivity for the fabrication of the aluminum alloy foam. The fluctuation of ±1.3 °C (±2.5% in

the volume fraction of solid) around 612.5 °C, which is close to the setting temperature of 613 °C, does not have a major effect on pore morphology.

The number of clogged cell walls increases when the volume fraction of solid increases beyond 15%. An increase in the number of clogged cell walls is more effective for the clogging effect compared to the increase in the fraction of the primary crystals in the already clogged cell walls. The preferred range of the volume fraction of solid for the fabrication of the stable foam, which was defined to have uniform pores with a small diameter and high circularity in this study, was between 15–35%. If the Al-Si alloy foam is fabricated with a certain volume fraction of solid, the clogging effect works most effectively and the cell walls become most stable when the volume fraction of solid is 35%.

Al_2O_3 particles generated from the oxygen in the atmosphere aggregate around the surface of the gas/liquid boundary. The oxygen may increase the stability of the foam. The stabilization mechanism investigated in this study can be adopted for the fabrication of foams of other hypoeutectic aluminum alloys. Further, the effect of temperature control on the deviation of the properties of aluminum alloy foams can be applied to other fabrication processes via the semi-solid route.

References in Chapter 3

[1] V. Gergely and T.W. Clyne: Drainage in Standing Liquid Metal Foams: Modelling and Experimental Observations. *Acta Materialia,* **52** (2004) *10*, 3047-3058, doi: 10.1016/j.actamat.2004.03.007.

[2] K. Heim, G.S.V. Kumar, F. Garcia-Moreno, I. Manke, and J. Banhart: Drainage of Particle-Stabilised Aluminium Composites through Single Films and Plateau Borders. *Colloids and Surfaces. A, Physicochemical and Engineering Aspects,* **438** (2013), 85-92, doi: 10.1016/j.colsurfa.2013.02.019.

[3] J.L. Murray and A.J. McAlister: The Al-Si (Aluminum-Silicon) System. *Bulletin of Alloy Phase Diagrams,* **5** (1984) *1*, 74-84, doi: 10.1007/BF02868729.

[4] J. Schmitz, B. Hallstedt, J. Brillo, I. Egry, and M. Schick: Density and Thermal Expansion of Liquid Al–Si Alloys. *J Mater Sci,* **47** (2012) *8*, 3706-3712, doi: 10.1007/s10853-011-6219-8.

[5] E. Weck, Leistner E. *Metallographic Instructions for Colour Etching by Immersion. II. Beraha Colour Etchants and their Different Variants.* (DVS GmbH, Düsseldorf, 1983) .

[6] S. Lei, L. Gao, Y. Harada, and S. Kumai: Microstructure Analysis of Quenched Semi-Solid A356 Aluminum Alloy Slurry by using Weck's Reagent. *Mater Trans,* **61** (2020) *6*, 1077-1083, doi: 10.2320/matertrans.L-M2020814.

[7] Y. Hangai, T. Takagi, S. Koyama, R. Suzuki, and Y. Kamakoshi: Refoaming of deformed aluminum foam fabricated by precursor foaming process using remaining foaming agent and densification using friction stir welding. *Materials letters*, **351** (2023), 135008, doi: 10.1016/j.matlet.2023.135008.

[8] R.M. Haag and F.J. Shipko: The Titanium-Hydrogen System2. *J Am Chem Soc,* **78** (1956) *20*, 5155-5159, doi: 10.1021/ja01601a005.

[9] L.N. Smith and C.J. Lobb: Percolation in Two-Dimensional Conductor-Insulator Networks with Controllable Anisotropy. *Physical Review. B, Condensed Matter,* **20** (1979) *9*, 3653-3658, doi: 10.1103/PhysRevB.20.3653.

[10] D. Stauffer, Aharony A. *Introduction to Percolation Theory / by Dietrich Stauffer and Ammon Aharony.* 2nd ed. (Taylor & Francis, an imprint of Taylor and Francis, Boca Raton, FL, 2014) .

Chapter 4

Cell wall structure stabilized with primary crystals

in the aluminum alloy foam fabricated via the semi-solid route

4. Cell wall structure stabilized with primary crystals in the aluminum alloy foam fabricated via the semi-solid route

4.1. Introduction

The inner pore structures of porous metals have gained considerable research attention. Recently, the optimization of the structure of open-cell porous metals has been investigated extensively [1-3]. Orthopedic applications and shock-absorbing materials require the structure to be optimized to achieve sufficient stiffness and high shock-absorbing efficiency. Open-cell porous metals can be designed digitally and fabricated using advanced manufacturing technology. The typical design strategy uses a computer aided design (CAD) that includes Platonic and Archimedean polyhedral solids to determine the structure [1-7]. Regularly arranged structures can be expressed quantitatively, e.g., FCC or BCC. Further, a Voronoi tessellation, which is a tessellation pattern in which a number of points scattered in a space subdivide some cells enclosing a plane closest to each point, is used to design the structure [2,8]. The Voronoi tessellation allows faster modeling because the arbitrary structure can be generated by controlling only the distance between the points. However, there are no examples of a quantitative definition of the structure, which can be expressed in terms of porosity.

The optimization and observation of the inner structure of closed-cell porous metals is widely studied. Previous research focused on observing the inner structure of the closed-cell porous metals using X-ray computed tomography (CT) instead of structural optimization. The inner structure can be observed nondestructively using X-ray CT[9]. Elmoutaouakkil *et al.* conducted two- and three-dimensional observations of three types of foams using X-ray CT (Figure 4-1). Deformed pores in closed-cell porous metals during the compression test was observed in situ [10,11]. Compression tests can be performed continuously on the same specimen to continuously follow the deformation behavior of a specific pore (Figure 4-2). X-ray tomoscopy, which analyzes the three-dimensional shape of the pores and changes over time, records the evolution of pores during foaming, as indicated in Figure 4-3 [12-14]. Further, the finite element method used for modeling can be obtained from the observed results using X-ray CT [15].
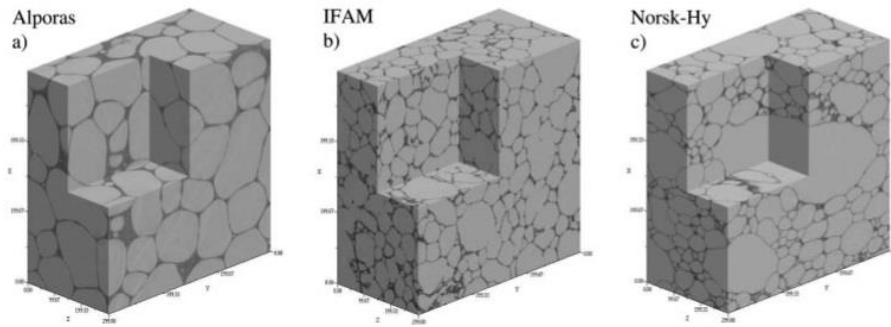
Figure 4-1 Three-dimensional rendering (volume size = 18 × 18 × 9 mm³) of the three aluminum alloy foams obtained by the X-ray CT system. (a) Alporas. (b) IFAM. (c) Norsk-Hydro [9].
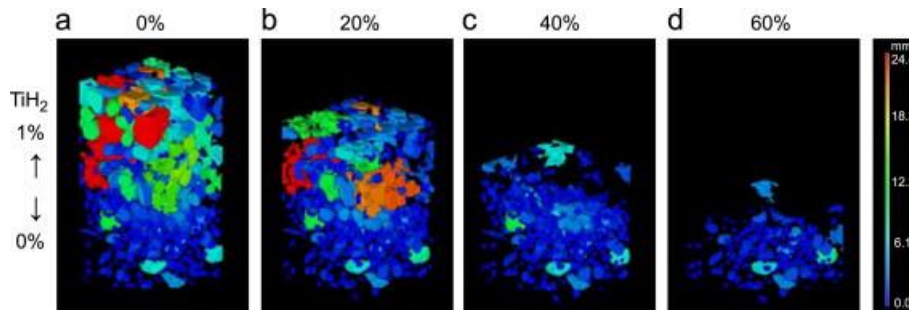
Figure 4-2 Color maps of the pore volumes obtained from the X-ray CT system during sequential deformation changing with the compressive strain [10].
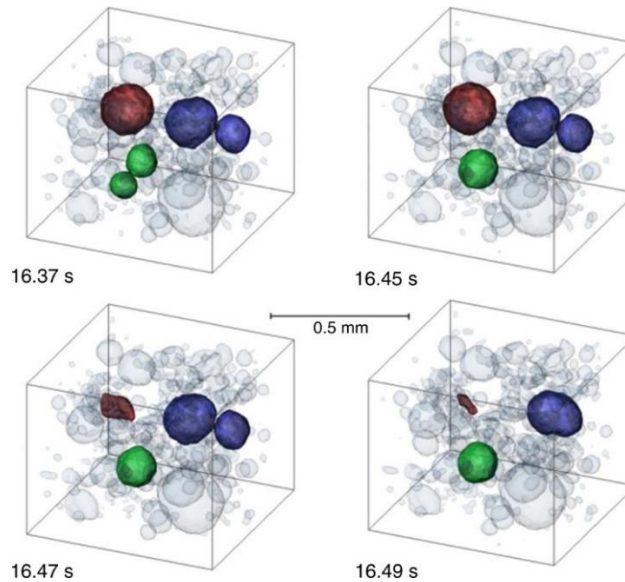
Figure 4-3 Evolution of a group of five bubbles in a liquid metal foam. Three-dimensional rendering of the topological rearrangement of bubbles in a close neighborhood inside a volume of 0.74 × 0.74 × 0.63 mm³. A cascade of events can be observed, starting with the merger of two bubbles (green), collapse of another (red), and another merger of two bubbles (purple) [14].

Several studies have investigated the inner structure of porous metals. However, even though it is possible to arrange or obtain the structure of the porous metals, parameters are not defined to explain the structure using one value. To the best of our knowledge, there are no studies that characterize the structure; however, the pore arrangement in the height direction and the distribution of each pore diameter have been evaluated quantitatively. Thus, it is necessary to quantitatively evaluate the structure of the stable foams fabricated in this study, thereby necessitating the need for determining parameters that represent the structure.

In Chapter 2, we applied the percolation theory to foam and clarified that the clogging effect can be expanded from the cell wall into the entire foam. The minimum amount of primary particles required to suppress drainage was determined using a percolation threshold [16-18]. However, these values are theoretical values calculated based on a regular shape or experimentally calculated values based on an approximate shape, and therefore, they are not the accurate percolation thresholds of the foam and cell walls. Kuwahara *et al*. used a single alloy film that simulates the drainage flow to calculate the accurate percolation threshold of the cell wall. As shown in Figure 4-4, a single alloy film has only one drainage flow; however, the actual cell wall may have some inflows and outflows connected to the drainage flow. The inflows and outflows are also the drainage flows of other cell walls. Hereafter, this combination of the drainage flow (main cell wall), inflows, and outflows are referred to as the "*cell wall structure*." The number of inflows and outflows must change depending on the inner structure of the foam. In addition, if all cell walls have the same volume and same amount of clogged primary crystals, the drainage in the cell wall with less outflows than inflows can be prevented easily compared to those with opposite cell walls. Figure 4-5(a, b) shows the two types of cell walls with different numbers of inflows and outflows. The cell wall indicated in Figure 4-5(a) has three outflows and two inflows, which indicates that the volume of the cell wall tends to decrease. The cell wall shown in Figure 4-5(b) has two outflows and three inflows, indicating that the volume of the cell wall tends to increase. Thus, the cell wall shown in Figure 4-5(b) can be more stable compared to that shown in Figure 4-5(a) even if they have same amount of primary crystals. Thus, the difference in the number of inflows and outflows is an important parameter for calculating the accurate percolation threshold of each cell wall. This new parameter can satisfy the demands of providing the parameter representing the structure of the foam because the difference in the number of inflows and outflows can be expressed by the value.
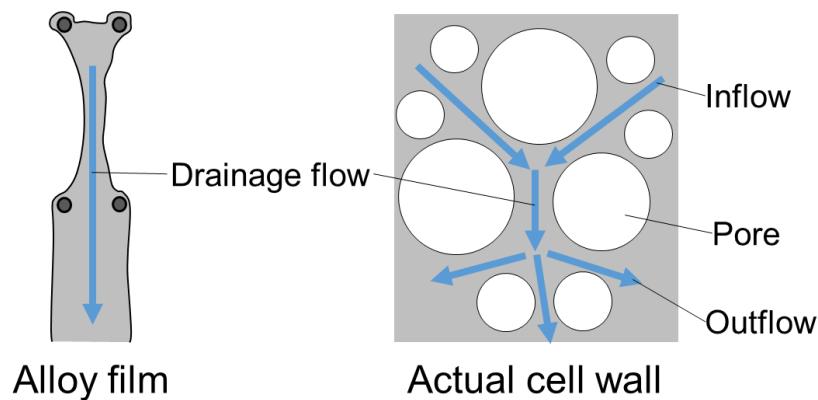
Figure 4-4 Drainage in the alloy film and actual cell wall.
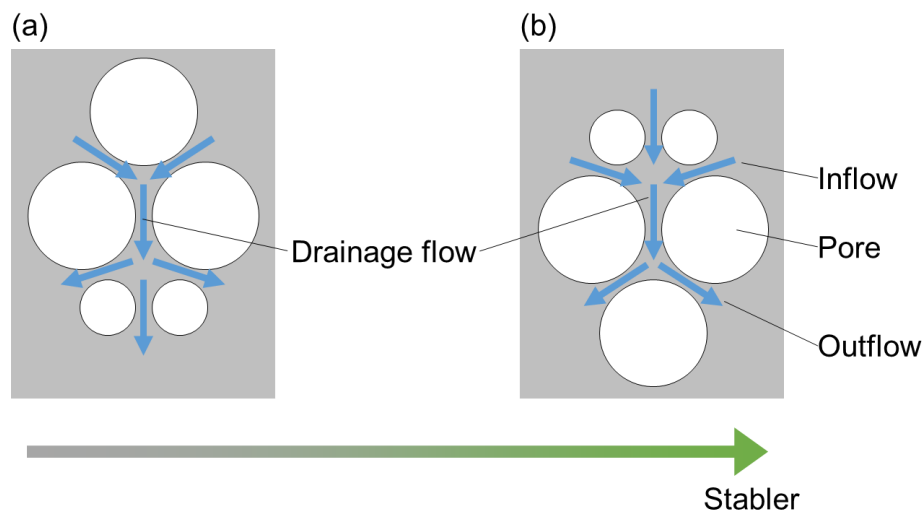
Figure 4-5 Two types of cell walls with different numbers of inflows and outflows. (a) Number of outflows is larger than that of inflows. The drainage seems to be developed easily. (b) The number of outflows is smaller than that of inflows. The drainage does not seem to be as developed as that shown in (a).

The difference in the number of inflows and outflows, which is expressed as δ, describes the one structure of cell walls around one specific drainage. The value of δ cannot describe the distribution of the cell wall structures. Therefore, it is necessary to obtain the spatial distribution of the cell wall structures. Further, it is useful to obtain distributions in the directions of the x, y, or z axis; however, it does not show the relationship between the cell wall structures. A pair distribution function is an effective method to describe the spatial distribution of the cell wall structures. The pair distribution functions can describe distances between the pair of objects. Pair distribution functions are widely used in discussion on the structure of the liquids and glasses. The main feature of liquids and glasses is that they have a disordered structure. A cell wall structure is not organized, and therefore, the pair

distribution function can describe the structure of the foam. This means that the nearest neighbor cell wall structure of the target cell wall structure can be obtained from the pair distribution function.

This study aims to clarify the structure of the foam in a quantitative manner by observing the inner structure of the foam using X-ray CT and by analyzing the spatial distribution of the cell walls. A cell wall structure that contains the drainage flow in main cell wall, inflows, and outflows will be defined to achieve these objectives. The cell wall structures are classified into some groups, which are determined based on the difference in the number of inflows and outflows. The spatial distribution of the cell wall structures can be obtained using pair distribution functions.

4.2. Experimental procedure

Aluminum alloy foam fabricated and observed in Chapter 2 is also used in this Chapter. This section describes the fabrication procedure and observation method of the inner structure. An Al-6.4 mass% Si alloy was cast from the Al-25.3 mass% Si alloy and high purity aluminum with the same procedure as described in Section 2.2.1 of Chapter 2. Subsequently, the cast Al-6.4 mass% Si ingot was melted. The aluminum alloy foam was fabricated from the molten aluminum alloy through the semi-solid route with the same procedure as detained in Section 2.2.2 of Chapter 2.

4.2.1. X-ray CT observations and the calculation of the volume of cell walls

The fabricated aluminum alloy foam was cut in half through the center. Only half of the specimen was cut into six specimens. The inner structure of each specimen was observed using an X-ray CT system (v|tome|x L300, Tokyo, Japan, Baker Hughes Japan Co., Ltd). Figure 4-6 indicates the schematic of the X-ray CT system. The X-ray CT observation was conducted by the Tokyo Metropolitan Industrial Technology Research Institute (Tokyo, Japan). The X-ray source was tungsten. During X-ray irradiation, the stage, where the specimen was placed, was rotated. Focus object distance (FOD) and focus detector distance (FDD) were 100 mm and 1000 mm, respectively. During the characterization, 3000 projection images were obtained per rotation of the stage.
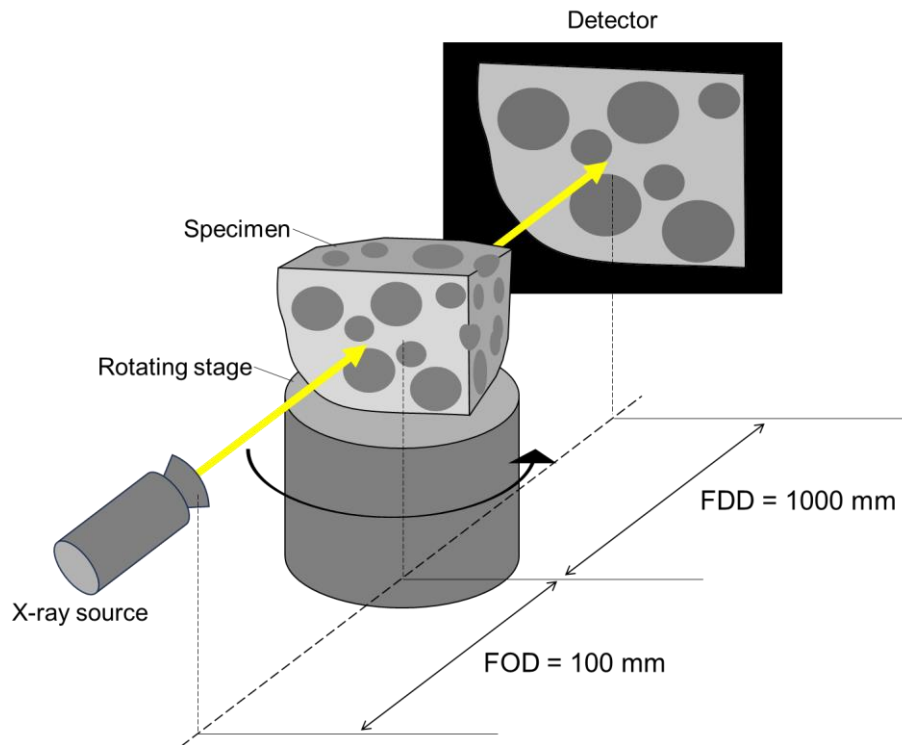
Figure 4-6 Schematic of the X-ray CT system to obtain the projection images of the aluminum alloy foam.

Projection images obtained from X-ray CT were constructed into a three-dimensional voxel model using a three-dimensional data viewer myVGL (version 3.4.0, Volume Graphics GmbH, Germany). Three-dimensional voxel models were converted into a series of continuous images with a spacing of 20 μm in the depth direction (Figure 4-7).
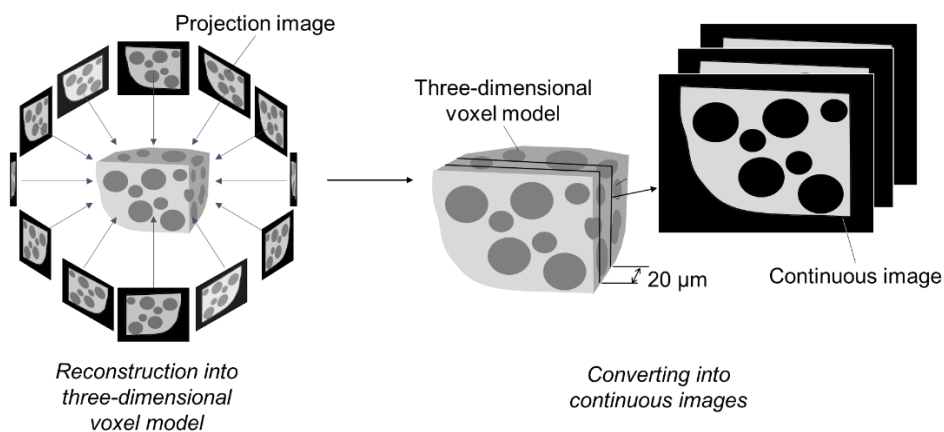
Figure 4-7 Schematic of the reconstruction of projection images into three-dimensional voxel models and converting into continuous images.

4.3. Results

4.3.1. Three-dimensional voxel model of the fabricated aluminum alloy foam

The porosity p was calculated as 30.2%. Figure 4-8(a, b) shows the obtained three-dimensional images of the foam and the close-up of one cell wall, respectively.

(a)
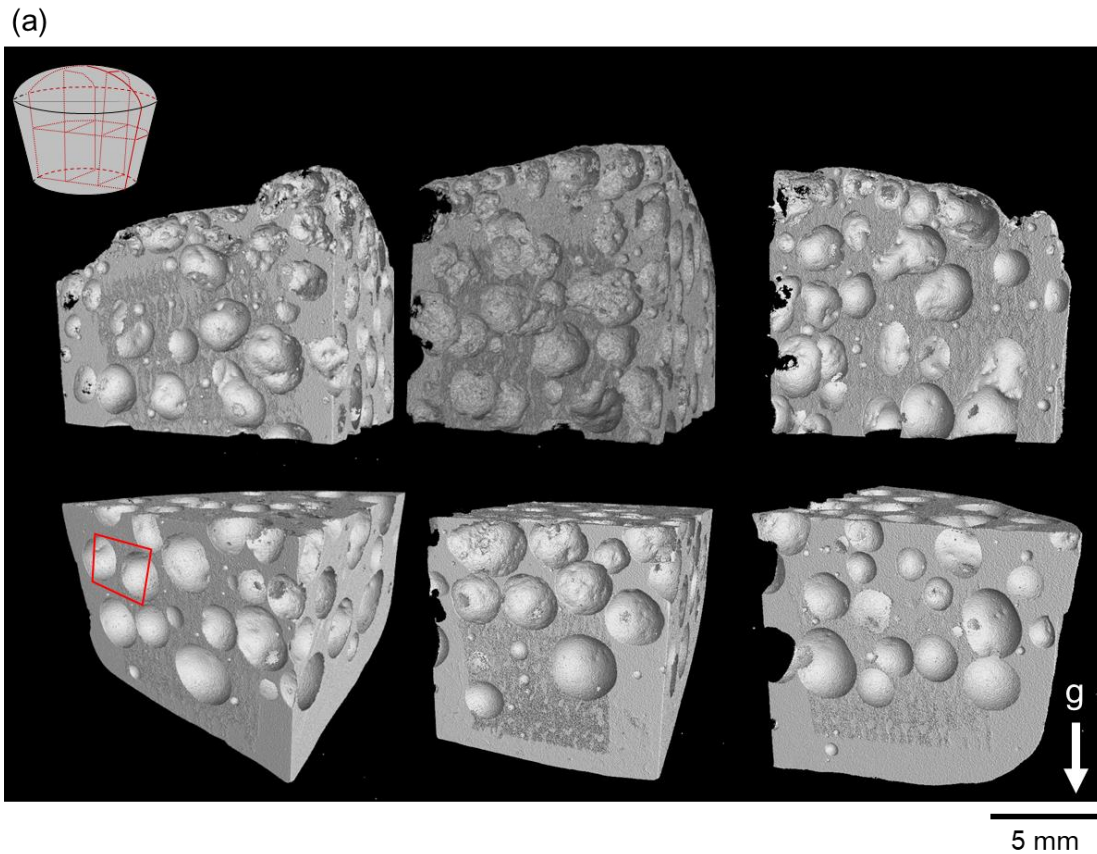
Figure 4-8 Three-dimensional voxel model reconstructed from the projection data obtained by using the X-ray CT system. (a) Six specimens cut from half of the fabricated aluminum alloy foam. The white arrow g indicates the direction of gravity during the foaming process. The red rectangle indicates the area shown in (b), close-up model of one cell wall.
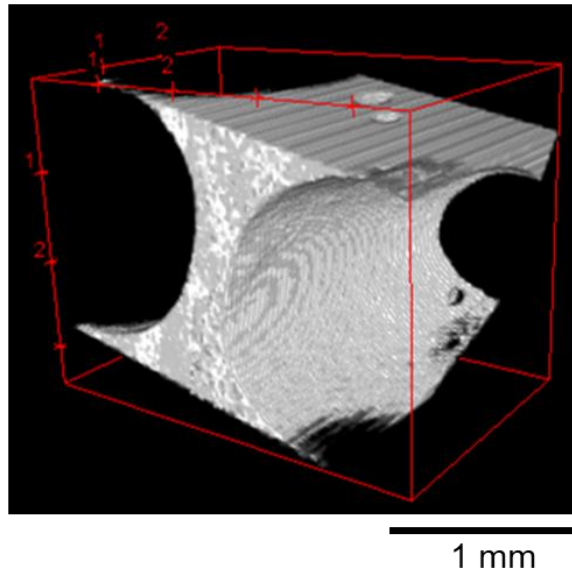
Figure 4-8 - continued
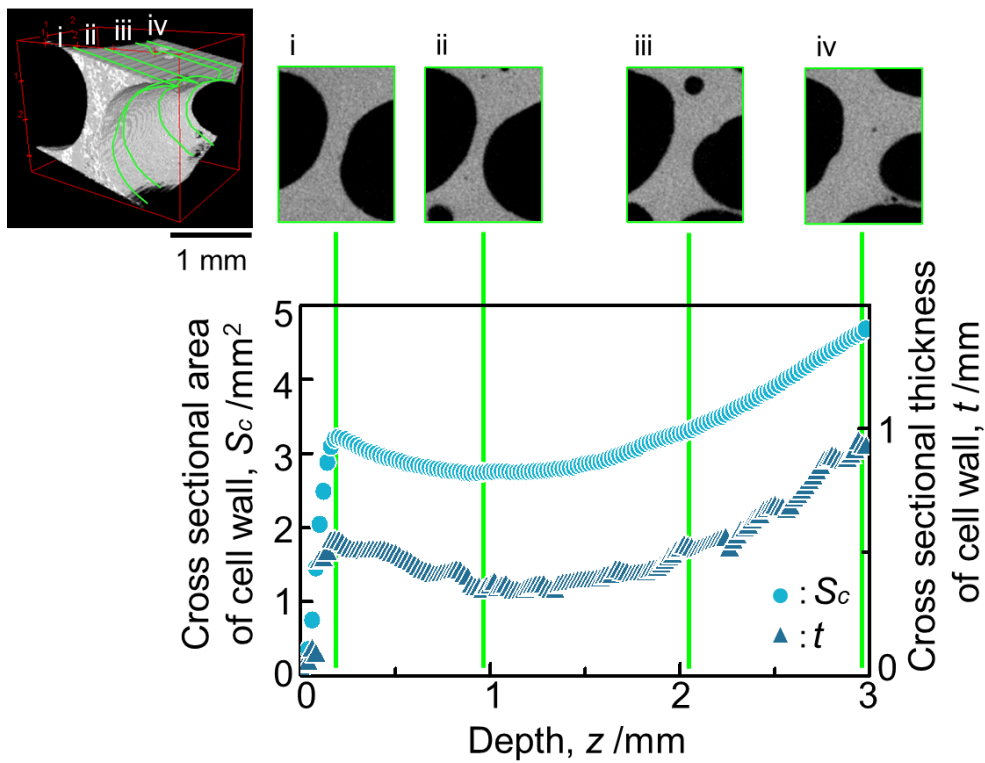
Figure 4-9 Cross-sectional area and thickness of the cell wall changing with the depth direction. Vertical green lines indicate each observed cross-section of the cell wall. Light and dark blue plots indicate the cross-sectional area and thickness of the cell wall, respectively.

Figure 4-9 indicates changes in the cross-sectional area and thickness of the cell wall in the depth direction. The cross-sectional area and thickness had the minimum value at the same thickness.

4.3.2. Microscopic observation of primary crystals

Microscopic images on the cross section of the foams were shown in Figures 2-7 and 2-8 (Section 2.3.2 and 2.4.1 in Chapter 2). Please refer to Chapter 2 for more information about the microscopic observations.

4.4. Discussion

The three-dimensional voxel model were used to observe the five types of the cell wall structures. Each cell wall structure shows a difference in the value of the number of inflows and outflows. The spatial distribution of the cell wall structures will be obtained by calculating the pair distribution function.

4.4.1. Difference in the number of inflows and outflows

Figure 4-8(a) shows that the structure of the cell walls is complex and randomly arranged. In this study, a method was suggested to quantitatively classify the cell wall structure to evaluate its stability in three dimensions. Each cell wall structure shows a difference in the value of the number of inflows and outflows. Cell walls parallel to the gravity direction were extracted to focus on the cell walls affected by only drainage. The number of inflows connected to the upper part of the drainage flow is denoted as n_i. The number of outflows connected to the lower part of the drainage flow is denoted as n_o. The difference in the number of inflows and outflows δ was calculated using equation (4-1).

$$\delta = n_i - n_o \qquad\qquad (4-1)$$

Moreover, it is possible to calculate the percolation threshold of each structure using the Monte Carlo method by defining value δ with the following steps:

i. Create a structure that consists only of the cell wall structure δ simulated as indicated in Figure 4-10(a). The number of all cell wall structures is counted by the value N_δ. The cell walls in a cell wall structure cannot be connected to other cell walls that are connected to the virtual top site or the virtual bottom site as indicated by the black arrow.

ii. Start the Monte Carlo simulation. First, find all paths that go through the virtual top site to the virtual bottom site. Paths that do not go back or upwards. For example, the green path is one of the considered paths shown in Figure 4-10(b). Count the number of paths N_{path}.
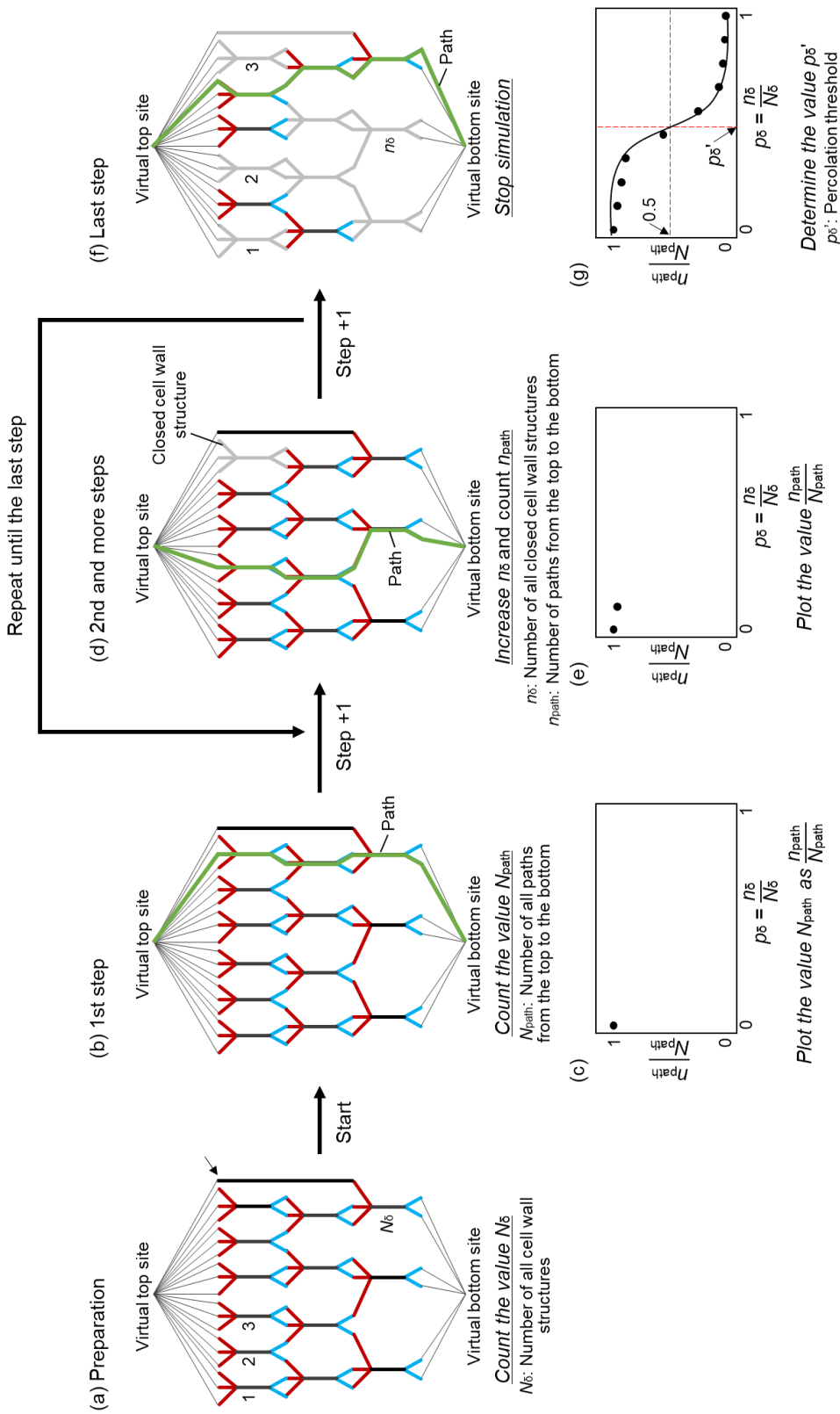
Figure 4-10 Schematic of the Monte Carlo simulation for calculating the percolation threshold. (a) Preparing the structure for the simulation. (b) Count paths from the virtual top site to the virtual bottom site as N_{path}. Plot N_{path} on the graph (b). (d) Increase the number of steps and closed cell wall by 1. Count paths calculated from the virtual top site to the virtual bottom site as n_{path}. Plot the value n_{path}/N_{path} on the graph (e). (f) Final structure obtained after the last step. (g) Final graph obtained from the Monte Carlo simulation.

iii. Prepare the graph with the value $\frac{n_{path}}{N_{path}}$ for the y axis and the value $\frac{n_\delta}{N_\delta}$ for the x axis. Plot the value

N_{path} as the value $\frac{n_{path}}{N_{path}}$ at the value $\frac{n_\delta}{N_\delta}$ is zero, as indicated in Figure 4-10(c).

iv. Increase the number of steps by 1. Increase the number of closed cell wall structures n_δ, which cannot go through, by 1, randomly, as indicated in Figure 4-10(d).

v. Find paths that go from the virtual top site to the virtual bottom site. The paths do not go back or upwards. Count the number of paths as n_{path}. The value n_{path} will become smaller than N_{path}.

Plot the value $\frac{n_{path}}{N_{path}}$ on the graph, as indicated in Figure 4-10(e).

vi. Repeat Steps iv and v for the set steps.

vii. Subsequently, repeat the set steps.

viii. Plot the value $\frac{n_{path}}{N_{path}}$ at each value $\frac{n}{N}$. The value $\frac{n}{N}$ can be recognized as the percolation probability

p_δ.

      Figure 4-10(g) shows the final graph that can be obtained. The value $\frac{n_{path}}{N_{path}}$ decreases rapidly

at a specific percolation probability p_δ, wherein the value can be defined as the percolation threshold p_δ' of the simulated cell wall structure. In this study, the percolation threshold p_δ' was obtained as the

value when the $\frac{n_{path}}{N_{path}}$ was 0.5.

      Figure 4-11 shows the percolation threshold p_δ' of each cell wall structure δ. All cell wall structures observed from the three-dimensional voxel model are also indicated.
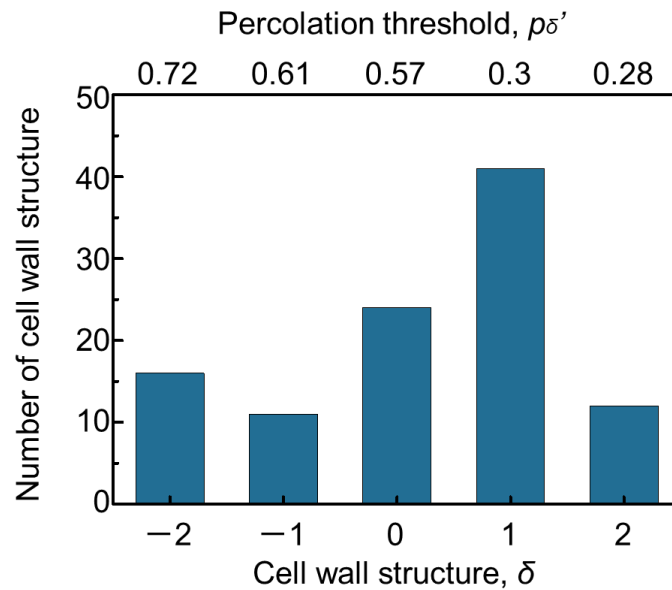
Figure 4-11 Percolation threshold $p_\delta{}'$ of each cell wall structure δ and its number.

Figure 4-12 shows the observed cell wall difference δ and its representative CT image, as well as the percolation threshold calculated using the Monte Carlo method. The cell wall difference δ was observed in the range of -2 to 2. The percolation threshold decreases with an increase in the cell wall difference δ. In other words, cell wall structures with larger δ values hinder drainage with fewer primary crystals. Therefore, cell walls with a larger δ values are more stable, whereas those with smaller δ values are less stable or consistently unstable.

Further, the spatial distribution of cell walls with each δ value was evaluated. Figure 4-13 shows the distribution of cell walls with different δ values along the gravity direction. Each plot represents an individual cell wall. Figure 4-14 illustrates the graph that shows the percentage of cell walls with each δ value measured at every 5 mm height. Figure 4-13 and Figure 4-14 show that cell walls with different δ values are almost uniformly distributed in the height direction, and their proportions do not vary with height. This implies that the cell wall structure is not random but arranged according to a certain rule. Thus, in this study, we decided to employ other methods to evaluate the overall structure of the cell walls.

δ	-2	-1	0	1	2
Typical example of cell wall as 3D image	(g)				
Scheme of cell wall structure					Invisible cell wall on 3D image
Percolation thresholds	0.72	0.61	0.57	0.30	0.28

Upper cell wall: n_i = 4
Lower cell wall: n_o = 2
$\delta = n_i - n_o = 2$

Unstable ← → Stable (easily clogged with small amount of primary crystals)

Figure 4-12 Observed cell wall structures with typical examples of the cell wall as a three-dimensional voxel model and a scheme of the cell wall structure. Calculated percolation thresholds are indicated at the bottom of the graph.
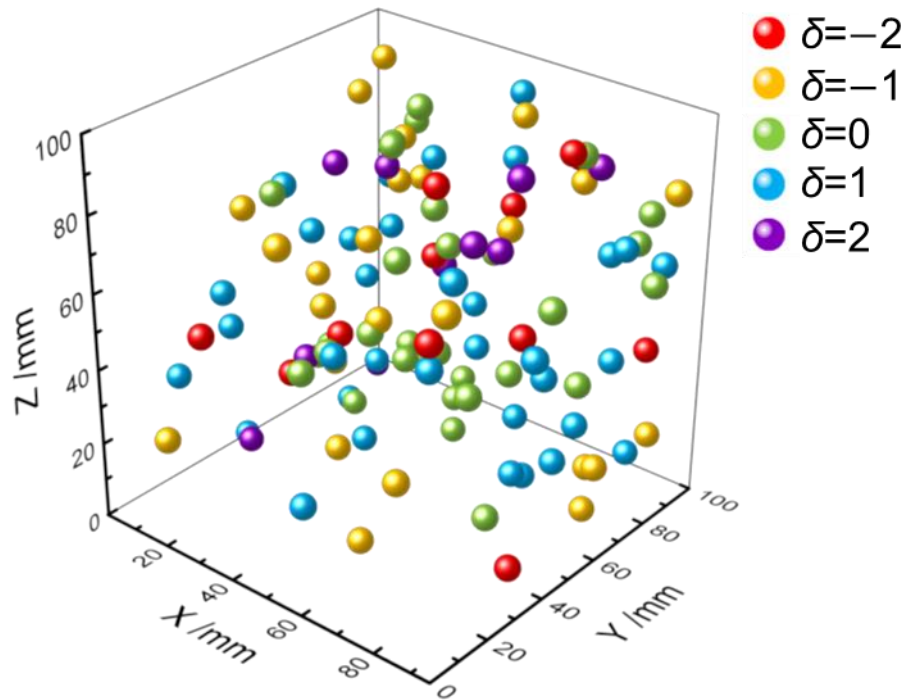
Figure 4-13 Spatial distribution of each cell wall structure δ. Each color represents the cell wall structure.
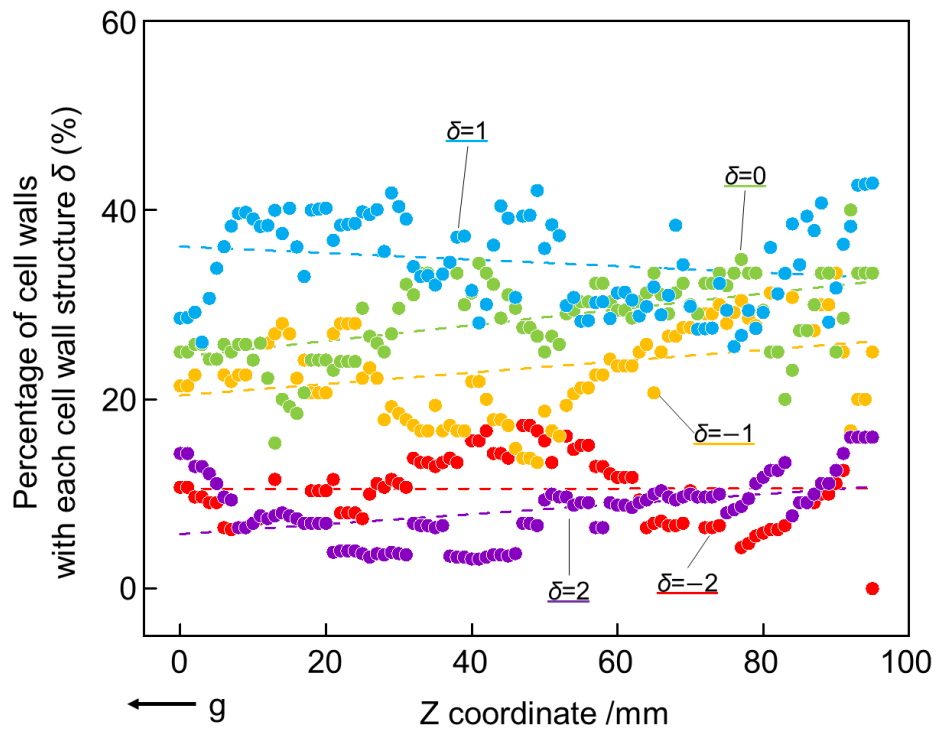
Figure 4-14 Distribution of the cell wall structure with each δ in the height direction.

4.4.2. Pair distribution function

A pair distribution function $g(r)$ can describe the distribution of distances between two arbitrary objects contained within a given volume. The number of objects on the small shell centered on the target object is small when the objects are arranged randomly. The surface area of the shell increases, and therefore, as shown in Figure 4-15, the number of objects on the larger shell may be large. Therefore, the number of objects contained per unit volume of a spherical shell with radius r and thickness dr can represent the distribution of the distance between two arbitrary objects.
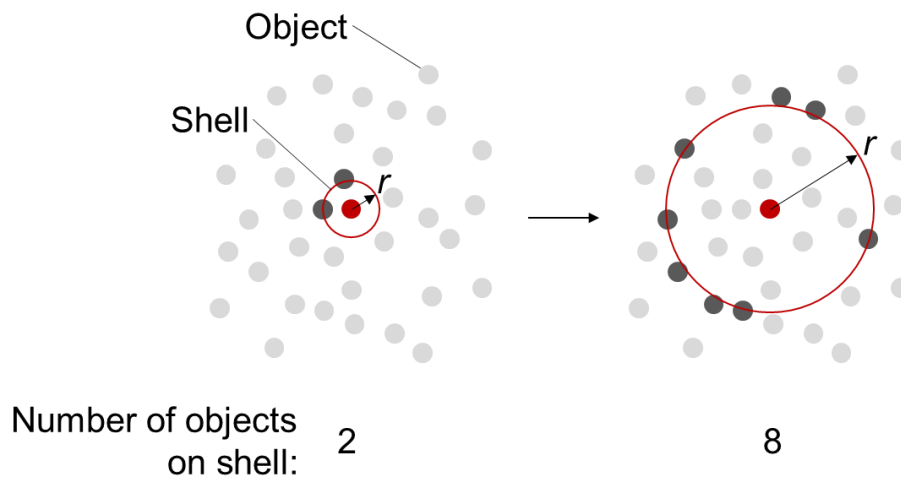
Figure 4-15 Schematic distribution of the objects and the method to count the number of objects on the shell.

The pair distribution function of the pairs of structures, target structure, and distributed structure were calculated. Thus, four pair distribution functions for each target structure were obtained. The nearest neighbor structure of the target structure were determined by comparing the value of r for the first peak of the four pair distribution functions. The pair distribution function was calculated as follows.
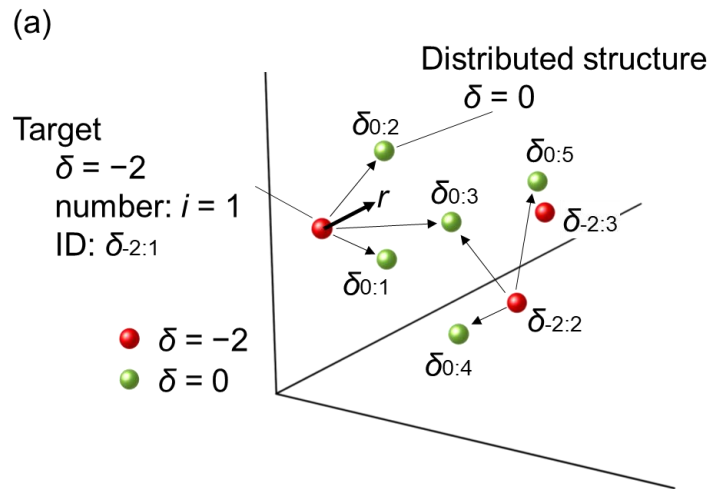
Figure 4-16 Schematic of how to calculate the pair distribution function $g(r)$. (a) Numbering definition of the target and distributed cell wall structure δ.

i. Obtain all coordinates of the cell wall structures. The coordinate is defined as the area centroid of the main cell wall. Each cell wall structure is numbered as the δ_{value} of cell wall structure: number. For example, the first and third cell wall structure within the value of the cell wall structure δ with –2 can be numbered as $\delta_{-2:1}$ and $\delta_{-2:3}$, respectively (Figure 4-16(a)).

ii. Determine the target cell wall structure δ (e.g., −2) and the distributed cell wall structure δ to calculate the pair distribution function (e.g., 0). The examples are shown in Figure 4-16(a).

iii. Calculate the distance r_i between the youngest structure within the target structure (e.g., $\delta_{-2:1}$) and each distributed structure (e.g., $\delta_{0:1}$, $\delta_{0:2}$, $\delta_{0:3}$, $\delta_{0:4}$, and so on). Plot the number of counts on the graph at each distance r_i indicated in Figure 4-16(b). In most cases, each distance r has only one count.

iv. Calculate the distance r_i between the second youngest structure within the target structure (e.g., $\delta_{-2:2}$) and each distributed structure (e.g., $\delta_{0:1}$, $\delta_{0:2}$, $\delta_{0:3}$, $\delta_{0:4}$, and so on). Plot the number of counts on the graph at each distance r_i, as indicated in Figure 4-16(c). Calculate the distance between all target structures and the distributed structure by changing the target structure (Figure 4-16(d)).

v. Merge all graphs into one graph, as indicated in Figure 4-16(e).

vi. Count the number of cell wall structures per range of dr and plot them on the graph as shown in Figure 4-16(f).
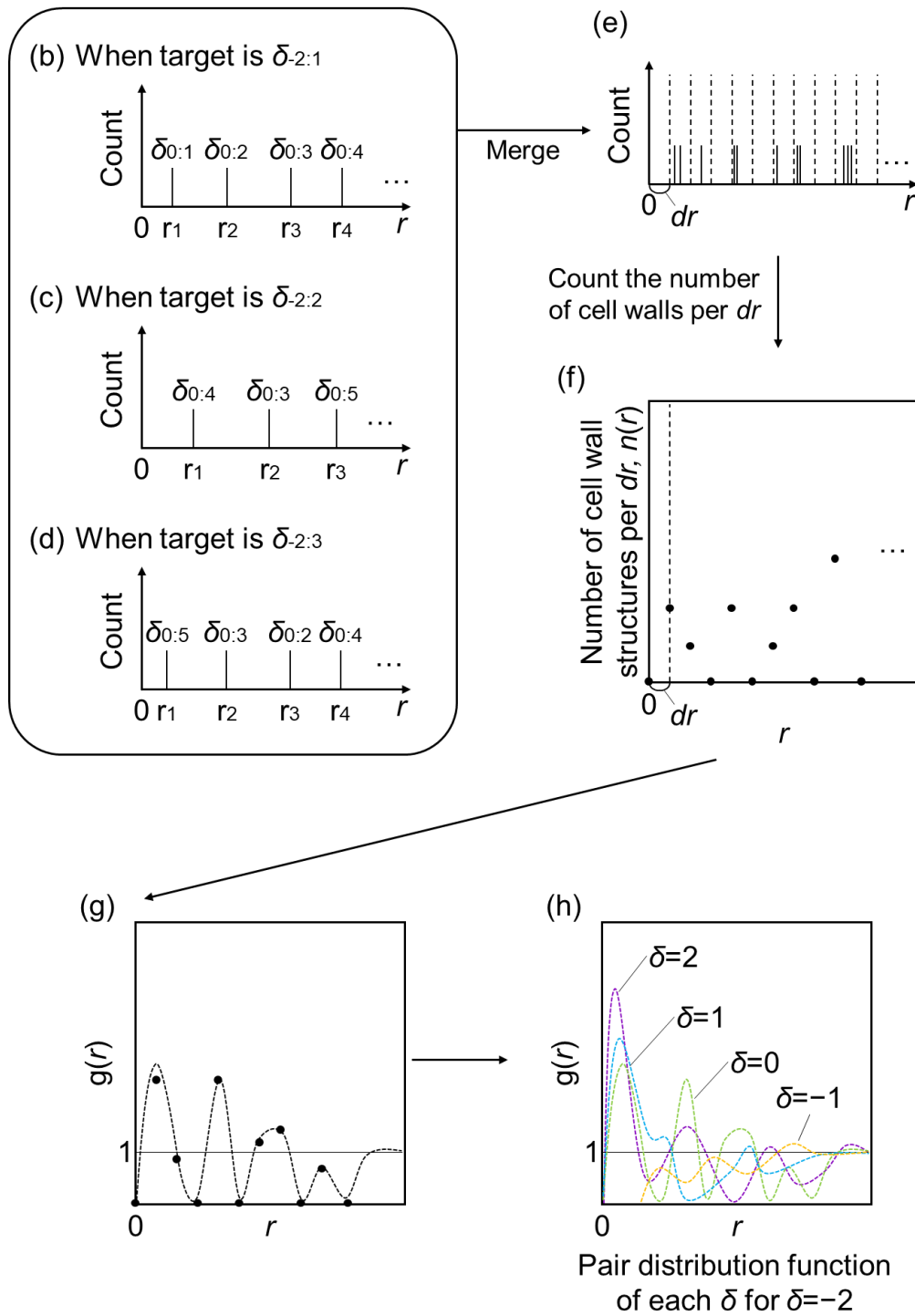
Figure 4-16 -continued. (b-d) Graphs of the counted cell wall structure at each _r_ when the target cell wall structure is $\delta_{-2:1}$, $\delta_{-2:2}$, and $\delta_{-2:3}$, respectively. (e) Merged graph of the counted cell wall structure at each _r_. (f) Graph of the number of cell wall structures per _dr_ n(r). (g) Pair distribution function of the cell wall structure $\delta = 1$ for $\delta = -2$. (h) Pair distribution functions of each δ for $\delta = -2$.

The number of cell wall structures as per the range of dr plotted on the graph, as shown in Figure 4-16(f), indicates the number of cell wall structures that exist within the spherical shell (thickness $= dr$ and diameter $= r$). The number of cell wall structures as per the range of dr $n(r)$ can be expressed by Equation (4-2). The value ρ_δ represents the number density of the distributed cell wall structure in the whole foam.

$$n(r) = 4\pi r^2 dr \cdot \rho_\delta \cdot g(r) \qquad (4-2)$$

The pair distribution function $g(r)$ describes the distribution of the distance between the pair of the structures. Therefore, the pair distribution function $g(r)$ can be calculated as follows.

vii. Divide the value $n(r)$ by $4\pi r^2 dr \cdot \rho_\delta$ and plot the results on the graph, as shown in Figure 4-16(g).

viii. Change the distributed cell wall structure (e.g., $\delta = 1$) and repeat steps iii–vii until all cell wall structures δ are treated as the distributed cell wall structure. Graphs indicated in Figure 4-16(h) can be obtained.

ix. Change the target cell wall structure (e.g., $\delta = -1$) and repeat steps ii–viii until all cell wall structures δ are treated as the target cell wall structure.

The results of the calculated pair distribution functions for each cell wall structure δ are shown in Figure 4-17(a-e). Each graph indicates that the nearest neighbor δ corresponds to each cell wall structure δ. Here, the results are summarized in Figure 4-17(f). The sum of the target cell wall structure δ and its nearest neighbor δ are shown in the table (Figure 4-17(f)). Figure 4-17(f) shows that the sum of most pair of target structure and nearest neighbor is zero. In those pairs of structures, the difference in the number of inflows and outflows complement each other. However, there are also two pairs where the sum is not zero. Thus, some cell wall structures still have extra inflows or outflows that are not connected to the nearest neighbor. However, they are summed to zero when all sums of the pairs of target structure and nearest neighbor were added together. This indicates that the difference in the number of inflows and outflows can be complemented not only by the nearest neighbor but also by the other extra inflows or outflows. Therefore, the cell wall structure of the stabilized foam, which is achieved through the clogging effect with the primary crystals, is rearranged in an order that complements all differences in the number of inflows and outflows.
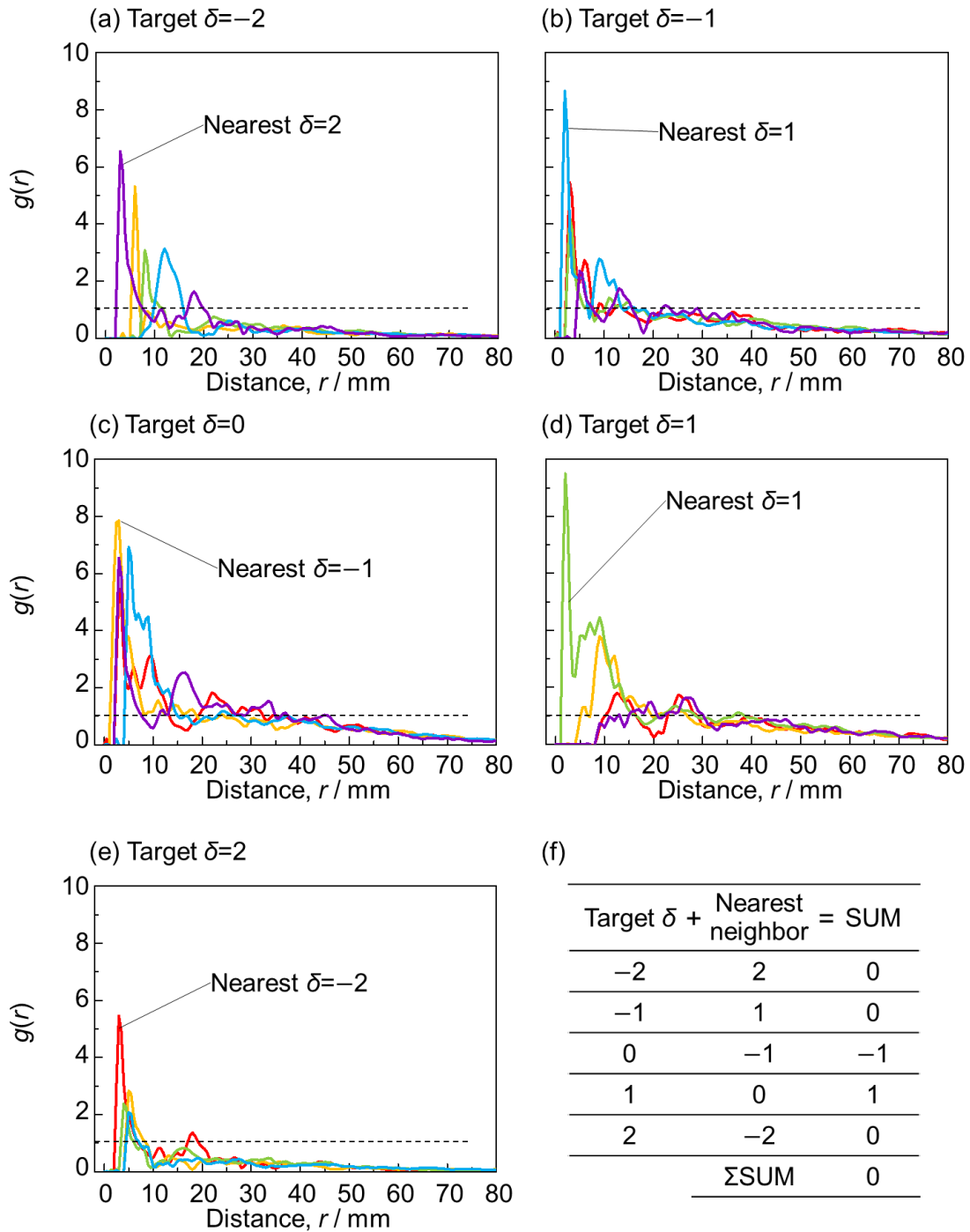
Figure 4-17 Pair distribution function for each target cell wall structure, (a-e) $\delta = -2, -1, 0, 1,$
and 2, respectively. (f) Correspondence table of target δ **and the nearest neighbor. The**
rightmost column indicates the total value of target δ **and the nearest neighbor** δ**.**

Figure 4-18 shows the ideal pair distribution function $g(r)$ in an infinite field filled with small particles. As indicated in the graph, the function converges to the value of 1, it means that the number density of the particles per a volume converges to the number density of particles in the entire field.
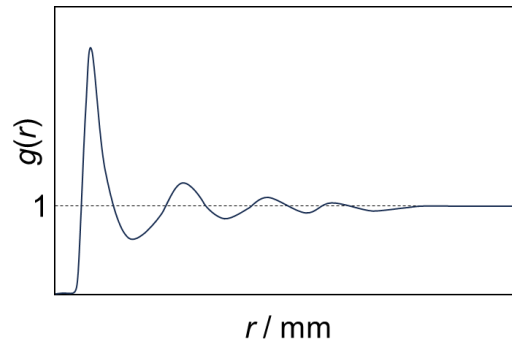
Figure 4-18 Ideal pair distribution function $g(r)$ in an infinite field filled with small particles.

However, the graphs shown in Figure 4-17 indicate that every pair distribution functions $g(r)$ does not converge to 1. The reason can be considered as that the maximum distance within the fabricated aluminum alloy foam is around 45 mm. The pair distribution function tried to measure the cell wall structures outside the fabricated aluminum alloy foam even any cell wall structures do not exist. The number of distributed cell wall structures can be smaller when the distance r is over around the 45 mm. Thus, the pair distribution function does not converge to 1 but decreases.

The 26 of new octant boxes were set surrounding original foam as indicated in . Each width and height of the duplicated box was 50 mm and 25 mm, respectively. Every cell wall structures also be duplicated along with the boxes. Thus, the pair distribution functions were calculated againn from this calibrated results as shown in Figure 4-20.
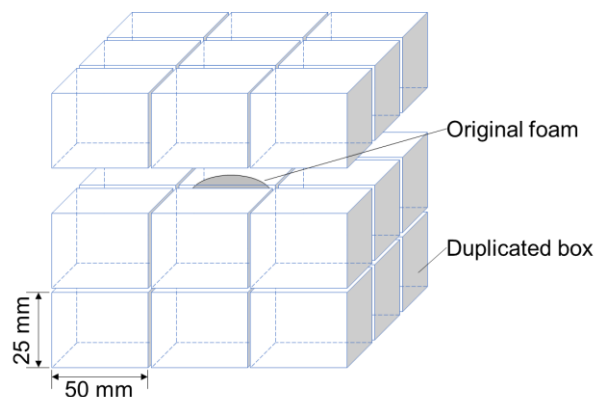
Figure 4-19 Schematic of octant boxes surrounding original foam.
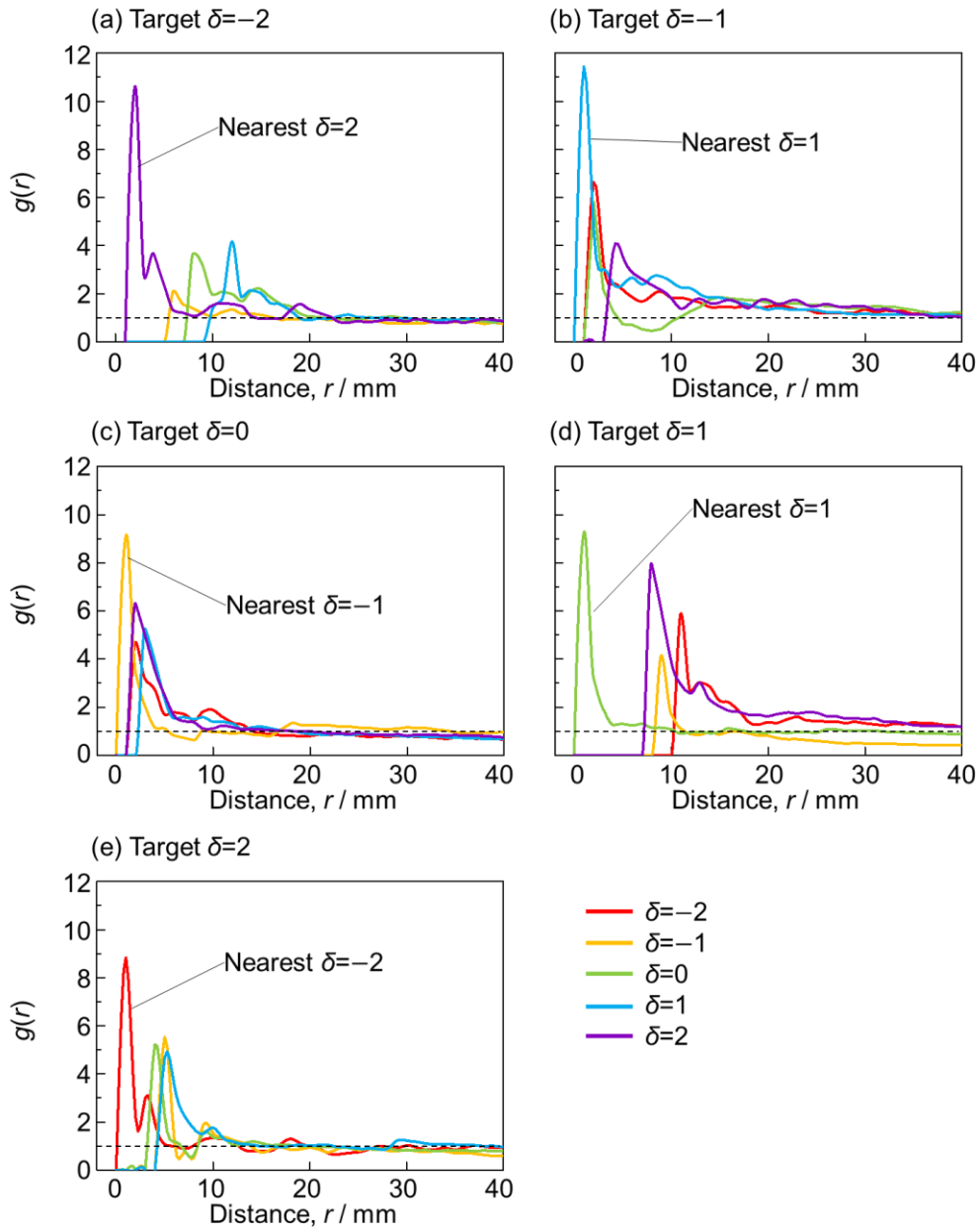
Figure 4-20 Calibrated pair distribution function $g(r)$ obtained from the duplicated cell wall structures inside the duplicated boxed surrounding the original foam.

The relationship between the target cell wall structure and the nearest neighbor did not change. The function finally converge to 1 as shown in Figure 4-20. Therefore, the results indicates that the cell wall structure δ was distributed homogeneously even under the small range.

4.4.3. Clogging effect based on the percolation theory

The percolation theory was applied to the cell walls present in the observed cross-section containing primary grains based on the results obtained so far. In this case, the percolation threshold

was determined using values obtained from the Monte Carlo method, as shown in Figure 4-11. The percentage of cell walls containing primary crystals that exceeded the new percolation threshold increased from 0.34, which was the result obtained using the conventional theoretical value, to 0.46. This increase can be attributed to a larger number of cell wall number differences δ with smaller permeation thresholds, which leads to an overall decrease in the permeation threshold. This result is highly useful for forming stable foam models and can be applied in simulations for further investigating the clogging effect in the future.

4.5. Conclusion

This study involved the fabrication of foam aluminum alloys using a semi-solid foaming method that revealed the following:

1. The structure of cell walls can be defined quantitatively by the difference in the number of inflows and outflows δ. Cell walls with larger δ values exhibit a clogging effect with fewer primary grains, which makes them easily stabilized.

2. In a stable foam, cell walls are rearranged such that the cell wall number differences δ complement each other because of the clogging effect. This structural model is useful for creating models of stable foams.

3. The clogging effect based on the new permeation threshold was examined and the results revealed that the foam exhibited greater stability than that anticipated initially.

These findings contribute to a better understanding of foam formation in aluminum alloys and provide valuable insights for the design and production of stable foams.

References in Chapter 4

[1] X. Wang, S. Xu, S. Zhou, W. Xu, M. Leary, P. Choong, M. Qian, M. Brandt, and Y.M. Xie: Topological Design and Additive Manufacturing of Porous Metals for Bone Scaffolds and Orthopaedic Implants: A Review. *Biomaterials,* **83** (2016)127-141, doi: 10.1016/j.biomaterials.2016.01.012.

[2] K. Kitazono, K. Matsuo, T. Hamaguchi, and Y. Fujimori: Design of Energy-Absorbing Materials for Space Crafts Based on Voronoi Diagrams. *Proceedings of the 11th International Conference on Porous Metals and Metallic Foams (MetFoam 2019):* 11th International Conference on Porous Metals and Metallic Foams (MetFoam 2019) 20-23 Aug, 2019); Anonymous Eds.: (Springer International Publishing, Switzerland, 2020), pp. 3-10.

[3] G. Ryan, A. Pandit, and D.P. Apatsidis: Fabrication Methods of Porous Metals for use in Orthopaedic Applications. *Biomaterials,* **27** (2006) *13,* 2651-2670, doi: 10.1016/j.biomaterials.2005.12.002.

[4] A. Takezawa, Y. Koizumi, and M. Kobashi: High-Stiffness and Strength Porous Maraging Steel Via Topology Optimization and Selective Laser Melting. *Additive Manufacturing,* **18** (2017), 194-202, doi: 10.1016/j.addma.2017.10.004.

[5] C. Lin, T. Wirtz, F. LaMarca, and S.J. Hollister: Structural and Mechanical Evaluations of a Topology Optimized Titanium Interbody Fusion Cage Fabricated by Selective Laser Melting Process. *Journal of Biomedical Materials Research. Part A,* **83A** (2007) *2,* 272-279, doi: 10.1002/jbm.a.31231.

[6] J. Parthasarathy, B. Starly, and S. Raman: A Design for the Additive Manufacture of Functionally Graded Porous Structures with Tailored Mechanical Properties for Biomedical Applications. *Journal of Manufacturing Processes,* **13** (2011) *2,* 160-170, doi: 10.1016/j.jmapro.2011.01.004.

[7] N. Taniguchi, S. Fujibayashi, M. Takemoto, K. Sasaki, B. Otsuki, T. Nakamura, T. Matsushita, T. Kokubo, and S. Matsuda: Effect of Pore Size on Bone Ingrowth into Porous Titanium Implants Fabricated by Additive Manufacturing: An in Vivo Experiment. *Materials Science & Engineering C,* **59** (2016), 690-701, doi: 10.1016/j.msec.2015.10.069.

[8] O.E. Sotomayor and H.V. Tippur: Role of Cell Regularity and Relative Density on Elasto-Plastic Compression Response of Random Honeycombs Generated using Voronoi Diagrams. *International Journal of Solids and Structures.,* **51** (2014), *21-22,* 3776-3786, doi: 10.1016/j.ijsolstr.2014.07.009.

[9] A. Elmoutaouakkil, L. Salvo, E. Maire, and G. Peix: 2D and 3D Characterization of Metal Foams using X-Ray Tomography. *Advanced Engineering Materials,* **4** (2002) *10,* 803-807, doi: 10.1002/1527-2648(20021014)4:103.0.CO;2-D.

[10] Y. Hangai, K. Takahashi, R. Yamaguchi, T. Utsunomiya, S. Kitahara, O. Kuwazuru, and N. Yoshikawa: Nondestructive Observation of Pore Structure Deformation Behavior of Functionally Graded Aluminum Foam by X-Ray Computed Tomography. *Materials Science & Engineering A,* **556** (2012), 678-684, doi: 10.1016/j.msea.2012.07.047.

[11] TODA, OHGAKI, UESUGI, KOBAYASHI, KURODA, KOBAYASHI, NIINOMI, AKAHORI, MAKII, and ARUGA: Quantitative Assessment of Microstructure and its Effects on Compression Behavior of Aluminum Foams Via High-Resolution Synchrotron X-Ray Tomography. *Metallurgical and Materials Transactions. A, Physical Metallurgy and Materials Science,* **37** (2006) *4,* 1211-1219, doi: 10.1007/s11661-006-1072-0.

[12] O. Brunke and S. Odenbach: In Situ Observation and Numerical Calculations of the Evolution of Metallic Foams. *Journal of Physics. Condensed Matter,* **18** (2006) *28,* 6493-6506, doi: 10.1088/0953-8984/18/28/005.

[13] F. García Moreno, M. Fromme, and J. Banhart: Real-Time X-Ray Radioscopy on Metallic Foams using a Compact Micro-Focus Source. *Advanced Engineering Materials,* **6** (2004) *6,* 416-420, doi: 10.1002/adem.200405143.

[14] F. García-Moreno, P.H. Kamm, T.R. Neu, F. Bülk, R. Mokso, C.M. Schlepütz, M. Stampanoni, and J. Banhart: Using X-Ray Tomoscopy to Explore the Dynamics of Foaming Metal. *Nat Commun,* **10** (2019) *1,* doi: 10.1038/s41467-019-11521-1.

[15] E. Maire, A. Fazekas, L. Salvo, R. Dendievel, S. Youssef, P. Cloetens, and J.M. Letang: X-Ray Tomography Applied to the Characterization of Cellular Materials. Related Finite Element Modeling Problems. *Composites Science and Technology,* **63** (2003) *16,* doi: 10.1016/s0266-3538(03)00276-8.

[16] D. Stauffer, Aharony A. *Introduction to Percolation Theory / by Dietrich Stauffer and Ammon Aharony*. 2nd ed. (Taylor & Francis, an imprint of Taylor and Francis, Boca Raton, FL, 2014) .

[17] L.N. Smith and C.J. Lobb: Percolation in Two-Dimensional Conductor-Insulator Networks with Controllable Anisotropy. *Physical Review. B, Condensed Matter,* **20** (1979) *9,* 3653-3658, doi: 10.1103/PhysRevB.20.3653.

[18] S.C. van der Marck: Percolation Thresholds and Universal Formulas. *Physical Review. E, Statistical Physics, Plasmas, Fluids, and Related Interdisciplinary Topics,* **55** (1997) *2,* 1514-1517, doi: 10.1103/PhysRevE.55.1514.

Chapter 5

Conclusions

5. Conclusions

This study focused on stable aluminum alloy foams fabricated through the semi-solid route established in this thesis. Unlike the melt route, the semi-solid route does not use a thickening agent to prevent drainage. Instead, it uses primary crystals to prevent drainage by clogging the cell walls; this phenomenon is referred to as the clogging effect.

To date, the clogging effect was only observed in a simulated single cell wall of the aluminum alloy foam, and it was unclear if it works in actual cell walls of the aluminum alloy foam. Further, drainage was inevitable in some cell walls, even in stable foams. In addition, the theoretical value for the fraction of primary crystals, which was previously identified as 40% in the volume fraction of solid, needed to be verified. Therefore, there was a need to identify if the clogging effect works in the actual cell walls in the stable aluminum alloy foam and if the entire foam is stable because of the clogging effect.

One limitation of fabricating the foam via the semi-solid route is the limited reproducibility. Many companies have fabricated the aluminum alloy foam for commercial use; however, they are not widely utilized because of low producibility. It is difficult to fabricate aluminum alloy foams with high reproducibility consistently under the same setting conditions, and therefore, the manufactures cannot provide products with the desired quality.

To overcome these issues, aluminum alloy foams were fabricated under the same setting conditions in this study, and their pore morphologies were compared. Further, the concentration of oxygen in the furnace was controlled to fabricate two foams under the different concentration of oxygen. The internal structure of the foam fabricated through the semi-solid route was recognized as the closed-cell structure. A foam is considered stable when the pores are aligned homogeneously; however, practically, the pores cannot be aligned homogeneously completely (such as honeycomb structure), and instead they form a random structure because the fabrication process involves random settings. A structural analysis was conducted to improve the mechanical properties, which were observed using X-ray CT. To date, to the best of the author's knowledge, there are no studies that focus on the shape and arrangement of the structure, which consists of the arrangement of individual pores and the connection of cell walls. Therefore, in this study, we defined the cell wall structure δ as the difference in the number of cell walls connected above and below the cell wall of interest and obtained its distribution using a pair distribution function.

Aluminum alloy foams are considerably useful because of their unique properties; however, they are yet to be employed widely in commercial applications because of their high fabrication costs and product reliability issues.

Therefore, this study aimed to clarify the stabilization mechanism of aluminum alloy foams fabricated via the semi-solid route. The following objectives were achieved through this study:

1) The stabilization mechanism was clarified.

2) The preferred range of the volume fraction of solid and effect of oxygen on the stability of the foam were determined.

3) The internal structure of the stable foam, including the cell wall structure δ, was determined.

In Chapter 2, the clogging effect was expanded to the entire aluminum alloy foam by applying the percolation theory. In Chapter 3, the allowance fluctuation of fabricated conditions was determined, and the effect of oxygen on the stability of the foam was identified. The preferred range of volume fraction of solid was revealed. Further, in Chapter 4, the cell wall structure δ was arranged to fill in the gap of number of connected cell walls.

Chapter 2: Prevention of drainage by percolated primary crystals in the cell walls of aluminum alloy foam fabricated via the semi-solid route

Aluminum alloy foam was fabricated through the semi-solid route and the area ratio of primary crystals to the area of cell walls was calculated. When the area ratio exceeded the percolation threshold of the cell wall, the cell wall was recognized as the clogged cell wall of which drainage is prevented. Further, when the fraction of the clogged cell wall exceeded the percolation threshold of the foam, the drainage in the entire foam was considered to be prevented. Therefore, the stability of the foam was confirmed by applying the percolation theory.

Chapter 3: Preferred volume fraction of solid for stable foams and the effect of oxygen on the stability of the foams

Aluminum alloy foams were fabricated under the same fabrication conditions, temperature, and concentration of oxygen. The results revealed that the pore morphologies, diameter, and circularity, showed small standard deviations when the volume fraction of solid was varied by 5%. In addition, the preferred range for the fabrication of stable foams were revealed to be 15−35%. In this preferred range, the clogging effect worked more effectively along with the increasing volume fraction of solid because the fraction of clogged cell wall also increased. Further, aluminum alloy foams were fabricated with different concentrations of oxygen. The porosity of the foam fabricated under the 10 ppm oxygen was lower than that fabricated under 18% oxygen. Thus, oxygen in the atmosphere was found to significantly affect pore stability.

Chapter 4: Cell wall structure stabilized with primary crystals in an aluminum alloy foam fabricated

via the semi-solid route

The internal structure of the foam was observed using X-ray CT scanning. The cell wall structure was classified along with its number difference δ between the inflows connected to the upper side and outflows connected to the bottom side. The pair distribution functions for each structure δ were used to discuss the nearest neighbor of each structure δ. The results revealed that cell walls with each defined cell wall structure δ were arranged to fill in the gap of value δ between each other. Thus, the cell wall structure δ in the entire foam was calculated to be zero.
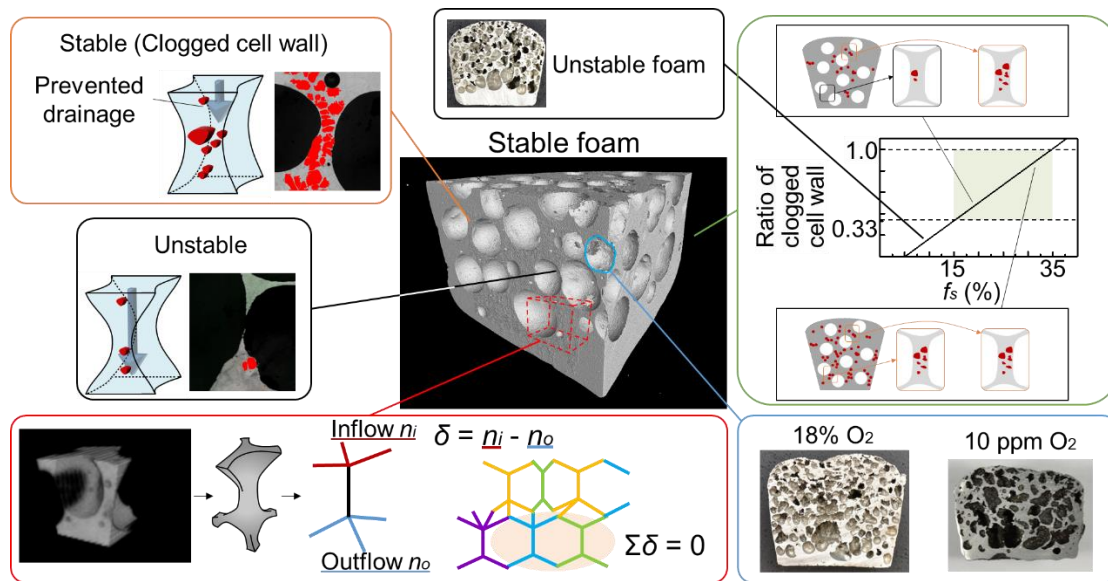

Figure 0-1 Schematic of the summary of this thesis.

5.1. Future application and research challenge

This study clarified the stabilization mechanism for the semi-solid route. The results of this study are expected to help resolve the issues of aluminum alloy foams, i.e., high fabrication costs and low reliability. The determined preferred range of the volume fraction of solid is expected to help lower the fabrication cost because tests to determine the optimal conditions for each fabrication no longer need to be performed. The manufacturers can use the specified volume fraction of solid to fabricate stable foams. Further, aluminum silicon alloy foam can be fabricated easily using the waste chip of the aluminum silicon alloy, which is a considerably common material in the industry. Thus, fabrication cost can be lowered in the future. Moreover, the reliability of the foam will be improved because the stabilization mechanism that can help fabricate stable foams was experimentally verified in this study. The allowance fluctuation is also expected to help improve the reliability of the foam.

However, the influence of the diameter of the primary crystals was not sufficiently understood based on the stabilization mechanism, and the relationship between the mechanical

properties and foam structure continue to remain unclear. Therefore, the preferred fabrication conditions for realizing specific properties cannot be determined based on the results reported in this study. Thus, this study offers two future research subjects: (1) Clarifying the influence of the diameter of the primary crystals on the stability of the foam, and (2) explaining the changes in the mechanical properties based on the structure of the foam.

The distribution of the diameter should be investigated to clarify the effect of the diameter of the primary crystals on the stability of the foam. The average diameter of the primary crystals or the maximum/minimum diameter can be used to discuss the effect of the diameter on the stabilization mechanism. Further, to explain the changes in the mechanical properties based on the structure of the foam, foams with different structure should be fabricated. Moreover, the mechanical properties (compressive behavior, insulating characteristics, and sound isolation) should be tested, and the relationship between the properties and structure should be discussed.

In addition, the stabilization mechanism investigated in this study can be adopted for fabricating foams of other hypoeutectic aluminum alloys. The effect of temperature control on the deviation of the properties of aluminum alloy foams can be applied to other fabrication processes that employ the semi-solid route. Thus, the results of this study can contribute toward not only the fabrication of aluminum alloy foam, but also the investigation of processes for developing new materials. The combination of metallurgy and physical approaches, such as percolation theory, are expected to help accelerate the future development of these material processing technologies.

Thus, the contributions of this study include defining the structure of stable foam and the preferred range of volume fraction of solid for fabrication and clarifying the stabilization mechanism of aluminum alloy foam through the semi-solid route based on percolation theory. These advances with help fabricate foams with high reliability via the semi-solid route.

Appendix A

Monte Carlo simulation to calculate percolation threshold of

each cell wall structure δ

Appendix A: **Monte Carlo simulation to calculate percolation threshold for each cell wall structure *δ***

This programming code is written in Python. Operation was checked under the following system environment: Python 3.11.1, Windows 11 Pro.

Advance preparation
1) Create a structure consisting only with one cell wall structure *δ* as shown in Figure A-1. Black circle is the connection of cell walls called node. Black rod is the cell wall itself called edge.
2) Record the connection of two nodes in each group. Create a CSV file named "edge.csv" as shown in Figure A-2.
3) Measure coordinates of nodes. Name each node. Create a CSV file named "node.csv" as shown in Figure A-3.
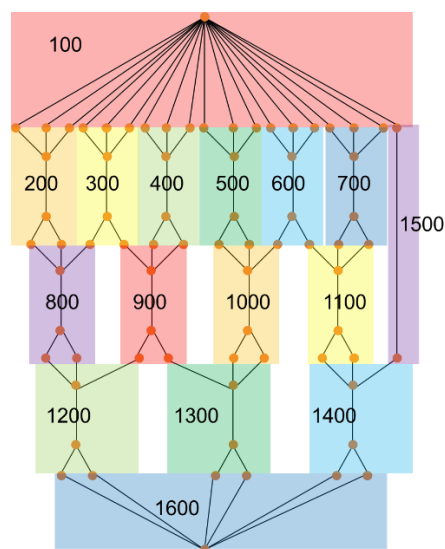4) Create a CSV file named "group.csv" as shown in Figure A-4.

Figure A-1 Example of a structure. Each cell wall structure *δ* is numbered as group.

Figure A-2 Example of the file "edge.csv."

node_id	node_name	group_id	X	Y
1001	一	100	366.5	1000
1002	二	100	11.5	792
2001	二	200	11.5	792
1003	三	100	69.5	792
2002	三	200	69.5	792
1004	四	100	112.5	792

Figure A-3 Example of the file "node.csv."

group_id	group_color
100	FF9500
200	F62E36
300	B5B5AC
400	009BBF
500	00BB85
600	C1A470

Figure A-4 Example of the file "group.csv."

The used source ccodes are written below.

```
1  import pandas as pd
2  import matplotlib.pyplot as plt
3  import japanize_matplotlib
4  import numpy as np
5  import networkx as nx
6  from graphillion import GraphSet, tutorial
7  import itertools
8  import random
9
10 """Monte Carlo Method for Percolation Threshold"""
11
12 #Calculate all paths Npath
13 print('----------------------------------------')
14 print('Calculate Npath')
15
16 #Read CSV into DataFrame
17 nodes = pd.read_csv("node.csv")
18 edge = pd.read_csv("edge.csv")
19 group = pd.read_csv("group.csv")
```

```
20
21  #Extract edges
22  nodes_edge = edge[["node_id1", "node_id2"]]
23
24  #Create a grapg
25  g = nx.Graph()
26  G = nx.DiGraph(g)
27
28  #Name the nodes as node_name
29  G.add_nodes_from(nodes["node_name"])
30
31  #Lint node_name and its coordinate(X, Y)
32  pos={}
33  for i, j, k in zip(nodes["node_name"], nodes["X"], nodes["Y"]):
34    pos[i] = (j, k)
35
36  #Add node_name and node_id to list e and link each other
37  e = []
38  for i, j in zip(nodes["node_name"], nodes["node_id"]):
39    e.append([i, j])
40
41  #Add information of edges to the graph
42  for i, j in zip(nodes_edge["node_id1"], nodes_edge["node_id2"]):
43      for k in e:
44        if k[1] == i:
45          for l in e:
46            if l[1] == j:
47              G.add_edge(k[0], l[0])
48
49  #Set output rules of the graph
50  plt.figure(figsize=(5,5),dpi=100)
51  plt.title('Initial structure', fontsize=10)
52  plt.xlabel("x")
53  plt.ylabel("y")
54  nx.draw_networkx(G, pos, node_color='b', alpha=0.8, node_size=10,
55  font_size=5, font_family='IPAexGothic')
56
57  Npath = 0
58  #Count Npath
59  for path in nx.all_simple_paths(G, source='一', target='七十四'):
60    """Word 一 and 七十四 are the node_name of virtual top site and
    virtual bottom site, respectively. Both are written in
    Japanese."""
61    Npath = Npath + 1
62
63  #Count how many node_name exists
```

143

```python
NN = nodes['node_name'].nunique()
print('Number of nodes is', NN)

percolate = []
probability = []
percolate.append(1)
probability.append(1)

print('Npath =', Npath)
print('-----------------------------------------')
plt.savefig('initial condition - Npath=' + str(Npath) + '.png')


nodes = []
edge = []
group = []
rn = 0
rlist = []
l = []
no = 0

npath = Npath

nodes = pd.read_csv("node.csv")
edge = pd.read_csv("edge.csv")
group = pd.read_csv("group.csv")

print('Calculate npath')

while npath > 0:
  no = no + 1
  #Determine which group will be deleted
  rn = random.randrange(200, 1600, 100) #Create random number in
  the range of 200 – 1600, every 1100
  while rn in rlist:
    #If created number was already used in steps so far, create
  number again
    rn = random.randrange(200, 1600, 100)
  else:
    rlist.append(rn)
    print('--------------------')


  #Take indexes that include rn in group_id
  drop_index_nodes = nodes.index[nodes['group_id'] == rn]
  drop_index_edge = edge.index[edge['group_id'] == rn]
```

```
108    drop_index_group = group.index[group['group_id'] == rn]
109
110    #Delete the indexes
111    nodes = nodes.drop(drop_index_nodes)
112    edge = edge.drop(drop_index_edge)
113    group = group.drop(drop_index_group)
114
115    #Count how many node_name exists
116    nn = nodes['node_name'].nunique()
117    print('Number of nodes is', nn)
118
119    print('Deleted the row whom group_id is',rn)
120    print('----------')
121    print(nodes)
122    print('----------')
123
124
125    #Count npath
126
127    nodes_edge = edge[["node_id1", "node_id2"]]
128
129
130    G2 = nx.Graph()
131    G = nx.DiGraph(G2)
132
133    G.add_nodes_from(nodes["node_name"])
134
135
136    pos={}
137    for i, j, k in zip(nodes["node_name"], nodes["X"], nodes["Y"]):
138      pos[i] = (j, k)
139
140      e = []
141      for i, j in zip(nodes["node_name"], nodes["node_id"]):
142        e.append([i, j])
143
144      for i, j in zip(nodes_edge["node_id1"],
145  nodes_edge["node_id2"]):
146          for k in e:
147            if k[1] == i:
148              for l in e:
149                if l[1] == j:
150                  G.add_edge(k[0], l[0])
151
152    plt.figure(figsize=(5,5),dpi=100)
153    plt.title('Structure', fontsize=10)
```

```
154    plt.xlabel('')
155    plt.ylabel('')
156    nx.draw_networkx(G, pos, node_color='b', alpha=0.8,
157  node_size=10, font_size=5, font_family='IPAexGothic')
158
159
160    npath = 0
161
162    for path in nx.all_simple_paths(G, source='一', target='七十四
     '):
163      npath = npath + 1
164
165    #Calculate percolate npath/Npath
166    n_N = npath / Npath
167    percolate.append(n_N)
168
169    #Calculate percolation probability pb = nn/NN
170    pb = nn / NN
171    probability.append(pb)
172
173    print('npath now =', npath)
174    print()
175    plt.savefig('No' + str(no) + 'cycle - npath=' + str(npath) +
176  '.png')
177
178
179  print(percolate)
180  print(probability)
181
182  plt.figure(figsize=(5,5),dpi=100)
183  plt.scatter(probability, percolate)
184  plt.title("Percolation")
185  plt.xlabel("Probability")
186  plt.ylabel("Percolate")
187  plt.savefig("percolation.png")
188  plt.show()
189
190  print('---------------------------------------')
```

Appendix B

Calculation of pair distribution function $g(r)$

Appendix B: Calculation of pair distribution function *g(r)*

This programming code is written in Python. Operation was checked under the following system environment: Python 3.11.1, Windows 11 Pro.

Advance preparation

1) Create a CSV file including coordinates of nodes for each cell wall structure δ. Name the file as "<δ>.csv" as shown in Figure B-1.

	coodinate /mm		
d	x	y	z
0	39	58	89
0	2	74	12
0	55	54	43
0	58	36	75
0	54	31	57
0	44	79	20

Figure B-1 Example of the csv file..

The used source code is written below.

```python
1  from csv import reader
2  import csv
3  from openpyxl import Workbook
4  from re import L
5  import matplotlib.pyplot as plt
6  import matplotlib
7  import os
8  import math as m
9
10 """Pair Distribution Function"""
11
12 print('----------------------------------------')
13 print('Now you are at')
14 print(os.getcwd() + '\n')
15 dir = str(input('Select the work directory'))
16 os.chdir(f'{dir}')
17 print('Now you are at' + os.getcwd() + '\n')
18
19
```

```python
20  for td in range(-2, 3): #td stands for target delta
21
22      plt.figure(figsize=(5,5),dpi=100)
23
24      for dd in range(-2, 3): #dd stands for distributed delta
25          #Open CSV file of target cell wall structure
26          data = open(f'{td}.csv', 'r', encoding='UTF-8')
27          #Write to list target
28          csv_reader = reader(data)
29          target = list(csv_reader)
30          #Delete two headers
31          del target[0]
32          del target[0]
33          data.close()
34
35          #Open CSV file of distributed cell wall structure
36          data = open(f'{dd}.csv', 'r', encoding='UTF-8')
37          csv_reader = reader(data)
38          distr = []
39          distr = list(csv_reader)
40          del distr[0]
41          del distr[0]
42          data.close()
43          print('----------------------------------------')
44
45          print(f'Calculate the distance between d={td} and d={dd}.
    ')
46
47          dist = 0
48          tl = len(target)  #Number of target cell walls
49          dl = len(distr)   #Number of distributed cell walls
50          print(f'Number of cell wall is target:{tl}, distributed:{d
    l}.')
51
52          dist_list = []
53          data = [[0,0,0,0]]
54
55          #Calculate the distance between two cell wall structure
56          for j in range(tl):
57              for k in range(dl):
58                  #According to the Pythagorean theorem
59                  dist = m.sqrt( (int(target[j][1])-int(distr[k]
    [1]))**2 + (int(target[j][2])-int(distr[k][2]))**2 + (int(target
    [j][3])-int(distr[k][3]))**2 ) #dist stands for distance
60                  #Add dist to list dist_list
61                  dist_list.append(dist)
```

```
62
63              data.append([j, k, dist])
64
65          del data[0]
66          #Set the header
67          header = [['target','distributed','length']]
68          with open(f'd={td}-d={dd}.csv','w') as file:
69              writer = csv.writer(file, lineterminator='\n')
70              writer.writerows(header)
71              writer.writerows(data)
72
73
74          #Calculate pair distribution function
75          r = 0 #Radius of spherical shell
76          dr = 5 #Thickness of spherical shell
77          V = 37000 #Volume of foam
78          rho = dl/V #Number density
79          gr_list = []
80
81          while r < 100:
82
83              r_dr = r + dr
84
85              #Count the cell walls within the spherical shell
86              nr = sum([r < i < r_dr for i in dist_list])
87
88              #Calculate the pair distribution function
89              try:
90                  gr = nr/(4*m.pi*r*r*dr*rho)
91                  gr_list.append(gr)
92              except ZeroDivisionError:
93                  gr = 0
94                  gr_list.append(gr)
95
96              r = r + 1
97
98          if dd == -2:
99              plt.plot(gr_list, color='purple')
100         elif dd == -1:
101             plt.plot(gr_list, color='dodgerblue')
102         elif dd == 0:
103             plt.plot(gr_list, color='forestgreen')
104         elif dd == 1:
105             plt.plot(gr_list, color='orange')
106         else:
107             plt.plot(gr_list, color='red')
```

```
108          plt.title('g(r) target:' + str(td), fontsize=10)
109          plt.xlabel('Distance r / mm')
110          plt.ylabel('Pair distribution function g(r)')
111          plt.savefig(f"g(r) target_{td} distributed_{dd}.png")
112      plt.show()
113
114 print('----------------------------------------')
115 print('Finish the calculation.')
116 print('Graphs were saved.')
117
118
```

Acknowledgements

—謝辞—

Acknowledgements

—謝辞—

<div align="right">髙松　聖美</div>

List of research achievements for application of Doctor of Engineering, Waseda University

Full Name： 髙松　聖美　　　　　　　　　　　　　　seal or signature

Date Submitted(yyyy/mm/dd)：　　2024/2/6

種類別 (By Type)	題名、 発表・発行掲載誌名、 発表・発行年月、 連名者（申請者含む） (theme, journal name, date & year of publication, name of authors inc. yourself)
Journal (Corresponding)	○[1] Characteristics of Pore Morphology in Aluminum Alloy Foams Fabricated by Semi-Solid Route among Multiple Experimental Runs, Metals, September 2023, vol. 13, pp. 847-859, **S. Takamatsu**, T. Arai, A. Sayama and S. Suzuki ○[2] Percolation of Primary Crystals in Cell Walls of Aluminum Alloy Foam via Semi-Solid Route, Metals, June 2020, vol. 10, pp. 1654-1669, **S. Takamatsu**, T. Kuwahara, R. Kochi and S. Suzuki
Jounal (Coauthor)	[3] Stabilization mechanism of semi-solid film simulating the cell wall during fabrication of aluminum foam, Metals, March 2020, vol. 10, pp. 333-345, T. Kuwahara, A. Kaya, T. Osaka, **S. Takamatsu** and S. Suzuki.
Oral presentation	[4] Aluminum alloy foams fabricated by semi-solid route in various atmosphere changing oxygen concentration, 145th JILM Annual Meeting, November 2023, **S. Takamatsu**, N. Tsuchida, M. Tsutsumi and S. Suzuki. [5] Relationship between Fabrication Conditions of Semi-solid Route and Morphology of Aluminum Alloy Foam, MetFoam2023 12th International Conference on Porous Metals and Metallic Foams, July 2023, **S. Takamatsu**, T. Arai, A. Sayama and S. Suzuki. [6] Effect of fabrication conditions of semi-solid route on stability of aluminum alloy foam, 143rd JILM Annual Meeting, November 2022, **S. Takamatsu**, T. Arai and S. Suzuki. [7] Stabilization Mechanism of Aluminum Alloy Foam affected by Primary Crystals and Cell Wall Structure, CellMAT2022 7th International Conference on Cellular Materials, October 2022, **S. Takamatsu**, T. Arai and S. Suzuki. [8] Effect of cell wall structure on stability of aluminum alloy foam, 142nd JILM Annual Meeting, May 2022, **S. Takamatsu**, T. Arai and S. Suzuki. [9] Stabilization mechanism and cell wall structure of alminum alloy foam in semi-solid route, 141st JILM Annual Meeting, November 2021, **S. Takamatsu**, T. Arai and S. Suzuki. [10] The Stabilization Mechanism of Semi-solid Foaming Method by Primary Crystals, MetFoam2019 11th International Conference on Porous Metals and Metallic Foams, August 2019, **S. Takamatsu**, T. Kuwahara, R. Kochi and S. Suzuki.
Poster presentation	[11] Pore morphology of aluminum alloy foam changing with fabrication conditions of semi-solid route, 144th JILM Annual Meeting, May 2023, **S. Takamatsu**, A. SAYAMA, T. ARAI and S. Suzuki. [12] Clogging effect with primary crystals in aluminum alloy foam based on percolation theory, 139th JILM Annual Meeting, November 2020, **S. Takamatsu**, T. Kuwahara, R. Kochi and S. Suzuki. [13] Stabilization mechanism of cell wall in aluminum alloy foamed in semi-solid state, 9th Porous Materials Research Symposium, March 2019, **S. Takamatsu**, T. Kuwahara, R. Kochi and S. Suzuki. [14] Stability of Cell Wall in Aluminum Alloy foamed in Semi-Solid State, 6th Poster Conference for Young Researcher JILM Kanto BRanch, August 2018, **S. Takamatsu**, T. Kuwahara, R. Kochi and S. Suzuki.
Lectures	[15] Application of semi-solid forming to fabrication of aluminum foam, Seminar at Technische Universitat Dortmund, July 2023, **S. Takamatsu**

List of research achievements for application of Doctor of Engineering, Waseda University

Full Name： 髙松　聖美　　　　　　　　　　　　　seal or signature

Date Submitted(yyyy/mm/dd): 2024/2/6

種類別 (By Type)	題名、　発表・発行掲載誌名、　　発表・発行年月、　　連名者（申請者含む） (theme, journal name, date & year of publication, name of authors inc. yourself)
Award	[16] Allowance range of fabrication temperature for pore stabilization mechanism to work in semi-solid route, Seminar at Deutsches Zentrum fur Luft- und Raumfahrt (German Aerospace Center), July 2023, **S. Takamatsu**. [17] Recent Progress of Porous Metals in Japan, Seminar at Technische Universitat Berlin, October 2022, **S. Takamatsu**. [18] Recent progress in porous metals for aerospace and other applications, Seminar at Deutsches Zentrum fur Luft- und Raumfahrt (German Aerospace Center), October 2022, **S. Takamatsu**. [19] Excellent English Poster Award, 144th JILM Annual Meeting, May 2023, **S. Takamatsu**. [20] Excellent Materials Science Acdemic Award, Graduate School of Fundamental Science and Engineering Waseda University, March 2021, **S. Takamatsu**. [21] Excellent Student Award, 6th Poster Presentation of Young Scientists JILM Kanto Branch, August 2018, **S. Takamatsu**. [22] Excellent Woman Award, 6th Poster Presentation of Young Scientists JILM Kanto Branch, August 2018, **S. Takamatsu**. [23] JILM Kanto Branch Special Award, 6th Poster Presentation of Young Scientists JILM Kanto Branch, August 2018, **S. Takamatsu**. [24] JILM Kanto Branch Award, 6th Poster Presentation of Young Scientists JILM Kanto Branch, August 2018, **S. Takamatsu**. Blank below